MAGNETO OPTICAL TRAP RECOIL ION MOMENTUM SPECTROSCOPY

by

HAI TRUONG NGUYEN

B.S., Saint Norbert College, 1999

A DISSERTATION

submitted in partial fulfillment of the

requirements for the degree

DOCTOR OF PHILOSOPHY

Department of Physics

College of Arts and Sciences

KANSAS STATE UNIVERSITY

Manhattan, Kansas

2003

Approved by:

Major Professor

B. D. DePaola

ABSTRACT

The Magneto Optical Trap Recoil Ion Momentum Spectroscopy (MOTRIMS) technique has been developed for ion-atom collisions experiments. This new approach expands the number of target species available as a target for ion-atom collision. The extreme low temperature of atoms in a magneto optical trap yields increased recoil ion momentum resolution as compared to the traditional COLTRIMS (Cold Target Recoil Ion Momentum Spectroscopy). Furthermore, the traditional method for cooling the target, namely supersonic gas jet expansion, is not suitable for targets with optically active electrons since these species generally form clusters or dimers upon expansion. Because cooling and trapping leaves some atoms with an electron in an excited state, MOTRIMS naturally allows the study of collisions with excited targets. The collision systems presented within this dissertation are for low energy charge transfer between singly charged alkali ions and trapped rubidium atoms. Detailed results from simultaneous measurements of target excited state fraction and kinematically complete relative cross sections for several systems having energetically degenerate channels will be addressed. Furthermore, development of the MOTRIMS technique has enabled it to become an unique probe of population dynamics. This latest development and its implications will be introduced.

TABLE OF CONTENTS

Table of Contents i

List of Figures iii

List of Tables viii

Acknowledgements x

Dedication xi

1 Introduction 1
- 1.1 Ion-Atom Collisions . . . 1
- 1.2 Perspectives . . . 3
- 1.3 Overview of Dissertation . . . 11

2 Theoretical Approaches 13
- 2.1 Multi-channel Landau-Zener Model . . . 13
- 2.2 Modified Demkov Model . . . 16
- 2.3 Semiclassical Close-Coupling . . . 17

3 Experimental Setup 21
- 3.1 Description of Apparatus . . . 21
- 3.2 Kinematics . . . 23
- 3.3 Beam-line and Ion-optics . . . 26
- 3.4 Ion Gun . . . 28
- 3.5 Target Preparation . . . 30
  - 3.5.1 Laser Cooling . . . 30
  - 3.5.2 Trapping Magnetic Field . . . 39
  - 3.5.3 Rubidium Source . . . 41
  - 3.5.4 Magneto Optical Trap Characteristics . . . 41
- 3.6 Momentum Spectrometer . . . 45
- 3.7 Detectors . . . 47
- 3.8 Coincidence Detection . . . 49
  - 3.8.1 Recoil Ion Geometry and Reconstruction . . . 54
- 3.9 Data Acquisition . . . 55

4 Experimental Results **57**
4.1 Relative Cross Section Measurements 57
4.1.1 $Na^+ + Rb$ 59
4.1.2 $Cs^+ + Rb$ 76
4.1.3 $Rb^+ + Rb$ 84
4.1.4 The Dual Beam Method 92
4.2 Magneto Optical Trap Population 102

5 Conclusion and Outlook **111**
5.1 Conclusion 111
5.2 Outlook 113

Bibliography **115**

A Acquisition Program **123**
A.1 Acquisition Program 124
A.2 MOTRIM6.com file 140
A.3 Time of Flight Drifts 141

B Simulations **143**

C Detectors **151**
C.1 Recoil Ion Detector 151
C.1.1 Principle of Operation 151
C.1.2 Efficiency 152
C.1.3 Resolution Calibration 153
C.2 Projectile Detector 154
C.2.1 Principles of Operations 155

D Rubidium Magneto Optical Trap **157**
D.1 Rubidium Atom 157
D.1.1 Doppler-free Saturated Absorption Spectroscopy 158
D.1.2 Laser Locking 161
D.2 Rubidium MOT Characteristics 164
D.2.1 Measuring MOT Temperature 164
D.2.2 Measuring MOT Density 168
D.2.3 The MOT in Operation 169

LIST OF FIGURES

1.1 (a),(b) Longitudinal momentum distribution for the recoil ions from the reaction 0.25 and 1 MeV He^{2+} + He → He^{+} + He^{+}. The momentum resolution is 0.26 a.u. The experimental results are from Ref. [29]. . . 6

1.2 Ion yields for 3 keV/u $O^{6+} + Na$. The experimental results are from Ref. [30]. 7

1.3 Experimental 2D momentum plots of (a) Na^{4+}, (b) Na^{3+}, (c) Na^{2+} and (d) Na^{+} recoils created by 3 keV/u O^{6+} impact. The experimental results are from Ref. [30]. 8

1.4 Q value spectrum for Li^{+} + Na($3l$), where l = s and p, shown as s function of longitudinal momentum transfer. The experimental results are from Ref. [32]. 9

1.5 Upper panel: Li angular scattering pattern for $\sigma(\theta, \phi)$ in 3s-2s electron transfer collisions extracted from the coordinate with highest resolution. Fraunhofer diffraction rings are clearly seen. Lower panel: The actual measured scattering pattern in momentum space for two selected velocities. The experimental results are from Ref. [32]. 10

3.1 MOTRIMS experimental setup. 22

3.2 Setup schematic. 27

3.3 Ion gun image. 29

3.4 Force on atoms. 31

3.5 External cavity diode laser in the Littrow configuration. 32

3.6 Power characteristics of the diode used in the master laser. 34

3.7 Power characteristics of the diode used in the repump laser. 35

3.8 Master-slave configuration. 36

3.9 Injection polarization. 37

3.10 Double-passing optics layout. 38

3.11 Single-passing optics layout. 38

3.12 Trapping optics. 39

3.13 Position-dependent force. 40

3.14 Magneto Optical Trap. 42

3.15 Magneto optical trap temperature determination. 43

3.16 Magneto Optical Trap theoretical excited state fraction as a function of both the trapping laser intensity and detuning. 45
3.17 Cut away view of the spectrometer. 46
3.18 Actual image of the spectrometer. 48
3.19 Calculated delay time for different projectile ions. 50
3.20 Coincidence detection electronic logics. 51
3.21 Electronic setup for coincidence detection. 52
3.22 TAC setup. 53

4.1 Partial energy level diagram for sodium and rubidium [76]. 60
4.2 TAC spectrum for 7 keV Na^+ + Rb($5l$), where l = s and p. 61
4.3 Q value spectra for 7 keV Na^+ + Rb($5l$), where l = s and p. Down projections of Fig. 4.2. The top panel is the total projection and the lower panel is the projection of the regions where the lasers are off. . 62
4.4 The adiabatic potential curves for the $NaRb^+$ molecule. This figure is from Ref. [43]. 68
4.5 (a) sinθ × DCS as functions of laboratory scattering angle θ for Rb(5s)→Na(3s) at impact energies from 7 to 2 keV. The ⊙ represent the MOTRIMS data and the solid line,—, denotes theoretical calculations folded with experimental angular resolution. The experiment results have been normalized to the theoretical data. (b) is the same as (a) except for the Rb(5s)→Na(3p) channel. Note the difference in the angular scale. 69
4.6 (a) Experimental measured DCS as functions of scaled laboratory scattering angle E × θ for Rb(5s)→Na(3p) at impact energies from 7 to 2 keV. Experimental data are normalized to the TCAOCC calculations. (b) is the same as (a) except that this is the results from TCAOCC calculations [43]. 71
4.7 (a) Same as Fig. 4.5 but for charge-transfer from Rb(5p) to Na(4s). Solid lines denote the TC-AOCC and circles represent the experiment data. (b) is the same as (a) except for the Rb(5p)→Na(3p) channel. 74
4.8 Same as Fig. 4.6 but for charge-transfer from Rb(5p) to Na(3p). . . 75
4.9 Partial energy level diagram for cesium and rubidium [76]. 77
4.10 Double Differential Cross Sections for 6 keV Cs^+ + Rb($5l$), where l = s and p. 78
4.11 Q-value spectrum for 6 keV Cs^+ + Rb($5l$), where l = s and p. The labels identify the final state in cesium; "*" on the labels indicate charge exchange from Rb(5p). The solid points are data; the inset shows the theoretical predictions of individual channel cross sections (dashed lines) and the sum of all the channels (solid line). 79

4.12 Counts *versus* scattering angle for the two dominant channels shown in Fig. 4.11. The resolution is approximately 30 microradians (4 points) and the error bars are statistical. 80
4.13 Perel's measured cross sections for Cs^+ + Rb(5s) [74]. 81
4.14 Experimental energy-dependent relative cross sections compared to modified Demkov model. Solid line is the theoretical calculation while the dash line is the solid line × 1.65. 84
4.15 Double Differential Cross Sections for 7 keV Rb^+ + Rb($5l$) where l = s and p. 86
4.16 Counts *versus* Q-value for 7 keV Rb^+ + Rb($5l$) where l = s and p. In (a) the trapping lasers are blocked, while in (b) they are unblocked. . 87
4.17 Resonant charge transfer differential cross sections for 7 keV Rb(5s)-Rb(5s) and Rb(5p)-Rb(5p). 89
4.18 Differential charge transfer cross sections for 7 keV Rb(5p)-Rb(4d) and Rb(5s)-Rb(5p). 90
4.19 Rubidium molecular potential curves. 91
4.20 Energy levels of alkali atoms [76]. 92
4.21 Total time of flight for coincidences from both Na^+ + Rb($5l$) and K^+ + Rb($5l$), where l = s and p, in the dual beams method. 93
4.22 The 7 keV Na^+ + Rb($5l$),where l = s and p, collision system used to probe target excited state fraction. 94
4.23 Q-value spectrum for 7 keV K^+ + Rb($5l$), where l = s and p, collision system. 95
4.24 Differential cross sections for 7 keV K^+ + Rb($5l$), where l = s and p, collision system. 97
4.25 Total time of flight for both coincidences from Na^+ + Rb($5l$) and Li^+ + Rb($5l$), where l = s and p, observed for dual beam method. 98
4.26 Na^+ + Rb($5l$),where l = s and p, collision system used to probe target excited state fraction. 99
4.27 Q-value spectrum for 7 keV Li^+ + Rb($5l$), where l = s and p, collision system. 100
4.28 Differential cross sections for 7 keV Li^+ + Rb($5l$), where l = s and p, collision system. 102

4.29 Q-value plot for the 7 keV Na^+ + Rb(5l), where l = s and p, collision system. Both lasers driving the Rb(5s)-Rb(5p) transition are on. Peak labels containing a star indicate channels where capture is from the Rb(5p) state. Other peaks represent capture from the ground state Rb(5s). The solid line is the sum of Gaussian fits to the individual peaks. 104
4.30 TAC signal *versus* Q-value. The vertical lines can be compared with the peaks of Fig. 4.29. Broken lines correspond to capture from excited states. 106
4.31 Ratio of capture cross sections *versus* measured excited state fraction. Error bars are absolute. 107
4.32 Time dependence of relative Rb(5s) and Rb(5p) populations. At t = 0, the light from the "repump" laser was blocked. The vertical line near 1.2 ms indicates at which point the beam was turned back on. Representative error bars are absolute; relative error is smaller than the size of the points. 109

B.1 Simulation for focal plane position. 144
B.2 Simulation for TOF vs. $P_{R_\parallel}$. 145
B.3 Simulation for $P_{R_\perp}$ vs. X position. 146
B.4 Simulation for $P_{R_\perp}$ vs. Y position. 146
B.5 Raw recoil ion image. 148
B.6 Simion magnetic field distortion effect. 149
B.7 Corrected recoil ion image. 150

C.1 Photo of recoil ion detector. 152
C.2 Recoil ion detector assembly. 153
C.3 Detector mounting scheme. 154
C.4 Resistive anode. 155
C.5 Image of the mask used to calibrate the detector. 156

D.1 Doppler broadened spectrum. 159
D.2 ^{87}Rb trapping levels 159
D.3 Optics setup for saturated absorption spectroscopy. 160
D.4 The probe beam absorption spectrum. 160
D.5 Circuit electronics to take the difference of two signals. 162
D.6 Doppler free saturated absorption. 163
D.7 Dichroic atomic vapor laser lock setup. 164
D.8 Dichroic atomic vapor laser lock signals. 165

D.9 PZT Electronics 166
D.10 Flouresence from TOF measurement. 167
D.11 MOT temperature measurements. 168
D.12 Magnetic field dependence of the MOT. 170
D.13 Rubidium source current dependence of the MOT. 171

LIST OF TABLES

3.1 Actual knob values for delay gate. 53
3.2 Actual knob values for TAC delay. 54

4.1 State selective energy dependent relative cross section experimental results for the Na^+ + Rb(5s) collision system. Here the relative cross sections for each channel are normalized to the ground state 5s total cross section. 63
4.2 Same as in table 4.1. However, the initial state is Rb(5p) and the relative cross sections are normalized to the Rb(5p) total cross section. 64
4.3 Energy dependent relative total cross sections ($\frac{\sigma_p}{\sigma_s}$) for the Na^+ + Rb($5l$), where l = s and p, collision system. 64
4.4 This table is from Ref. [43]. Bound state energies of Na obtained from the model potential and the comparison with experimental data [76]. Even-tempered basis functions are used to diagonalize the atomic Hamiltonian. Energies are in atomic units. 65
4.5 This table is from Ref. [43]. Bound state energies of Rb obtained from the model potential and the comparison with experimental data [76]. Even-tempered basis functions are used to diagonalize the atomic Hamiltonian. Energies are in atomic units. 66
4.6 Theoretical integral cross sections (10^{-16} cm^2) for charge transfer from ground state Rb(5s) to final states [43]. The third and fourth lines show the comparison between theory and experiment for the capture cross section ratio: Na(3s)/Na(3p). 67
4.7 Theoretical integral cross sections (10^{-16} cm^2) for charge transfer from Rb(5p) to the indicated final states [43]. The third and fourth lines show the comparisons between theory and experiment for the capture cross section ratio: Na(4s)/Na(3p). 72
4.8 Experimental state selective energy dependent relative cross sections for the Cs^+ + Rb(5s) collision system. Here the relative cross sections for each channel are normalized to the ground state Rb(5s) total cross section. 82

4.9 Experimental state selective energy dependent relative cross sections for the Cs^+ + Rb(5p) collision system. Here the relative cross sections for each channel are normalized to the excited state Rb(5p) total cross section. 83
4.10 Energy dependent relative total cross section for Cs^+ + Rb(5l) where l = s and p. * indicates excited state fraction was obtained by observing target fluorescence. 83
4.11 Experimental relative charge transfer cross sections for 7 keV Rb^+ + Rb(5l), where l = s and p. 88
4.12 Experimental relative charge transfer cross sections for 7 keV K^+ + Rb(5l), where l = s and p. 96
4.13 Experimental relative charge transfer cross sections for 7 keV Li^+ + Rb(5l), where l = s and p. 101

D.1 Rubidium isotope natural abundances, nuclear spins, and masses. . . 157

ACKNOWLEDGEMENTS

There are many people that provided me assistance I need through out my educational pursuit. This work would not have been possible without the people I mention here. I would like to thank my advisor, Prof. Brett D. DePaola, for being an advisor with many ideas, insightful thoughts, encouragements, and patience. I also would like to extend my gratitude to Sue, Brett's wife. Beside being a good cook, Sue is also a very responsible landlord.

I would like to thank Dr. John and Margaret Spangler for believing in me to succeed in graduate school and allowing me to live with them for a couple of weeks before I begin my doctoral program. Also, I would like to thank Dr. Xavier and Karine Fléchard for their friendships and laboratory guidance as I embark upon MOTRIMS. Dr. Richard Brédy and Dr. Takaaki Awata helped me in many ways as I take and analyze data. I would like to thank the committee for careful review of this manuscript. Professors Lew Cocke and Chii-Dong Lin have provided many physical insights into experimental results observed using MOTRIMS.

This experimental work would not have turned out without the assistance from J. R. Macdonald laboratory support staff. Kevin Carnes, Vince Needham, Bob Gerring, Bob Krause, Mike Wells, Al Rankin, Scott Chainey, and Charles Fehrenbach would drop everything and concentrate on what I needed. I appreciate help and friendship from Teck Lee, Chris Verzani, Alina Gearba, and How Camp.

My family is the source of my inspirations. Everything that I have accomplished is due to their hardwork and love. My father (Ba) has provided me with all the opportunities he possibly could to achieve before he succumbed to cancer. My mother (Má) is continuing what she does best, loving.

Con cám σn ông bà nội, ông bà ngoại, ba (Nguỹên Văn Lợi) và má (Lâm Ngọc Anh) dã cho con một cuột sôńg có nhiêù ý ngĩa. Em cám σn các anh (Sσn và Lành), và các chị (Hà, Hiêú và Hiêǹ) giúp em tìm nêǹ tinh trông mình.

DEDICATION

To my family

Lòng mẹ bao la nhu biển Thái Bình

Chapter 1

Introduction

Ionization is a process in which an atom loses one or more of its electron to the continuum or to other atoms. A subset of ionization, charge transfer between a neutral atom and an ion, is treated in this dissertation. Natural ionization processes occur everywhere as the result of the interaction of photons, electrons, atoms, or ions with matter. The study of inelastic processes in ion-atom collisions is crucial not only for understanding the basic mechanism of the underlying reactions, but also for understanding the dynamic behavior and the physical properties of both astrophysical and controlled-thermonuclear-fusion Tokamak plasmas. Understanding ionization processes, more particularly charge transfer processes, is important to a broad range of pure and applied research. Experimental and theoretical data from collision experiments and calculation are used to elucidate atomic processes in laboratory plasmas, surface and material study and modification, earth's atmosphere, and even the creation of molecules in interstellar space [1, 2, 3, 4, 5].

1.1 Ion-Atom Collisions

When an ion collides with an atom, processes like excitation, charge exchange and ionization can occur [6]. The collision energies are classified according to the relative

velocity of the projectile and transferred electron. For low energy, $\frac{v_{projectile}}{v_{electron}} < 1$, electron transfer into resonant projectile states dominates over all other channels, and this channel's dominance increases as the collision energy decreases. This process depletes the initial state even at large impact parameters. This phenomenon can be qualitatively understood, since in resonant electron transfer, no energy need be transferred from the relative nuclear motion to the electronic motion. The collision system can be considered as being a diatomic molecule with time-varying internuclear separation. The electron motion is considered to be perturbed by the nuclear motion. Total cross section calculations using a nonperturbative description, where initial and final electronic motions are accounted for, are expected to be accurate. For intermediate energy collisions, $\frac{v_{projectile}}{v_{electron}} \sim 1$, electron transfer to non resonant states becomes appreciable. Furthermore, excitation and ionization process begin to compete with the charge transfer process. The quasi-molecular picture is less accurate; therefore, nonperturbative methods become less reliable. A Classical Trajectory Monte Carlo(CTMC) approach has been employed to calculate electron capture cross section in this energy regime [7]. However, CTMC fails at small angle, large impact parameter collisions because the nuclei are treated classically. To partially correct for the non-physical consequences of this, the electron is artificially forbidden to penetrate inside ($r < 2a_o$). At higher energy, $\frac{v_{projectile}}{v_{electron}} > 1$, all electron transfer cross sections decrease as energy increases. Excitation and ionization processes become more dominant. The projectile is considered as a perturbation to the target wave function. In this dissertation, only collisions in the low energy regime will be considered.

1.2 Perspectives

From a theoretical perspective, an enriched experimental database would allow rigorous comparison with theoretical model calculations. Of particular interest with respect to the focus of this thesis, calculation of charge transfer from ground and excited states of alkali metal atoms to protons have been done *via* a molecular treatment [8]. Charge transfer cross sections have been calculated for low energy protons (10 eV to 10 keV) incident on Na, K, Rb, and Cs. An impact parameter perturbed stationary state theory which takes the electron translation factors into account, was used. Results for electron capture from the ground states were compared to the experimental results of Nagata [9] and showed good agreement.

From an experimental perspective, charge transfer cross section measurements have been made either by detecting the slow target ions produced in the collision or by measurement of the projectiles. However, it is also possible to measure the radiation that is produced in those processes in which the products are formed in excited levels. Measurement of the neutralized projectiles for low energy ion collisions with gas targets have been done since the 50's [10, 11, 12]. The cross sections were deduced from the variation in neutral projectile flux with collision chamber gas pressure. However, the majority of charge transfer measurements have been done *via* collection of the ions produced in the collisions. This method allows precise control of the path length taken by the collision products *via* an applied external electric or magnetic field. It is this recoil ion method that will be addressed in this dissertation.

In the study of the dynamics of ion-atom collisions, among the most important quantities that one can measure are the Q-value and the scattering angle. The Q-value, a measure of the change in the internal energy of a system, provides, for example, quantitative information of initial and final state (in charge transfer colli-

sions) electron emission energy (in ionization) and initial and final vibrational states (in collisions involving molecules). The better the resolution in Q-value, the better one can differentiate between energetically similar collision channels. Scattering angle measurements, by which is meant collision cross sections, differential in projectile scattering angle, provide rigorous tests of theoretical models, since in order for the model to give agreement with experiment, it must correctly predict magnitudes as well as relative phases among the various collision channels. The direct measurement of Q-values is, in general, difficult to achieve in high resolution since typically, $\Delta E/E$ is a very small quantity, where E is the projectile energy, and ΔE is the change in energy of the projectile. Similarly, $d\sigma/d\Omega$ is generally difficult to measure directly since scattering angles tend to be rather small. For example, in the charge transfer collisions discussed in this work, cross sections peak at scattering angles of approximately 200 μRadians.

In the seventies and eighties, the first attempts at measuring the scattering angles and momenta of slow recoil ions were reported [13, 14, 15]. As will be shown later in this dissertation, the projectile scattering angle is directly proportional to the transverse momentum component of the recoil momentum, while the Q-value is linearly related to the longitudinal component of the recoil momentum. In 1987, Ullrich and Schmidt-Böcking successfully measured the transverse recoil ion momenta in 340 MeV U^{32+} on Ne collisions [16, 17]. That study reported the use of a static, room temperature gas target, time-of-flight measurement of recoil ions in a field free drift tube, and magnetic projectile ion charge state selection. The momentum resolution of this simple spectrometer was later improved through the use of a cooled gas cell (tens of Kelvin) [18, 19]. The result of this advance in technology was the first measurement of multiple-Differential Cross Sections (DCS) by coincident detection of recoil ion and projectile transverse momenta [18, 19, 20, 21, 22, 23]. Con-

currently, researchers at Kansas State University were using warm effusive gas-jet targets and an electric projection field [24, 25]. This development yielded the first measurement of recoil ion longitudial momentum distributions, allowing one to deduce the Q-values of the collision. Since the early ninties, researchers around the world including University of Frankfurt (Germany), Kansas State University (USA), CIRIL/GANIL (Caen, France), and RIKEN (Japan) have developed and utilized recoil ion momentum spectrometers based on supersonic gas-jet targets. The intrinsic temperature of these gas-jet targets is typically at or below 1 K. Such use of cold targets has yielded a momentum resolution of 0.2 a.u., more than a factor of 10 better than effusive or static target devices. Further improvement of the spectrometer, particularly the capability of focusing is projected to yield an ion-momentum resolution of 0.05 a.u. [24, 25, 26, 27]. With the rapid developments of target Recoil Ion Momentum Spectroscopy (RIMS), through the use of supersonic gas jet targets in combination with electric field extraction of recoil-ions, Cold Target Recoil Ion Momentum Spectroscopy, (COLTRIMS) [28, 29] yields a resolution of Δ $E_R \approx \pm$ 30μeV for Helium recoil-ions and a 4π solid angle for the detection of momenta below 5 a.u. [29]. Experimental data presented in Fig. 1.1 show the longitudinal momentum distribution for recoil ions from the reactions 0.25 and 1 MeV He^{2+} + He $\rightarrow$ He^{+} + He^{+}.

Recent developments at Kansas State University and by other groups around the world [30, 31] make use of Magneto Optically Trapped atoms as a target in Recoil Ion Momentum Spectroscopy. Details of this methodology are presented in this dissertation. Of paramount importance in RIMS is that the thermal momentum distribution of the target be small compared to the momentum transferred to it in the collision. In the COLTRIMS method, this is typically accomplished by pre-cooling the target, and then allowing it to undergo supersonic expansion. In the MOTRIMS

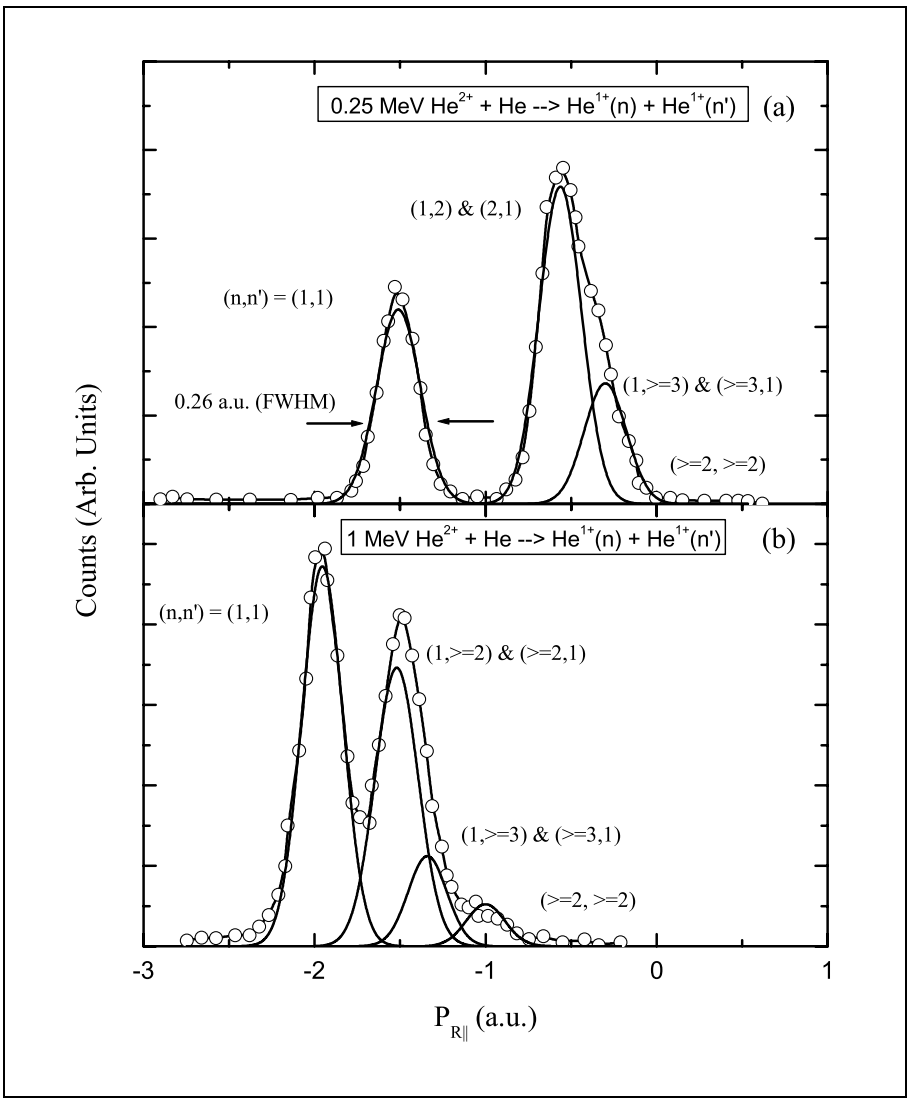

Figure 1.1: *(a),(b) Longitudinal momentum distribution for the recoil ions from the reaction 0.25 and 1 MeV* He^{2+} *+ He* $\rightarrow$ He^{+} *+* He^{+}*. The momentum resolution is 0.26 a.u. The experimental results are from Ref. [29].*

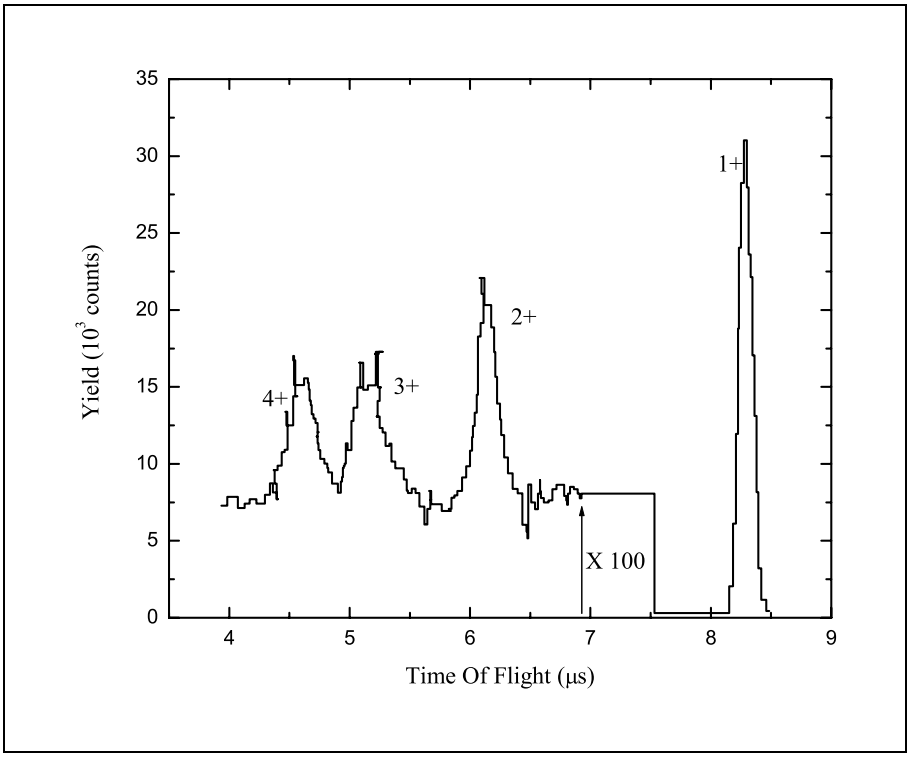

Figure 1.2: *Ion yields for 3 keV/u $O^{6+} + Na$. The experimental results are from Ref. [30].*

technique, the supersonically expanded gas target is replaced by a Magneto Optical Trap. The advantages are three-fold. First, the atoms can be laser cooled to a far lower temperature (typically, a few hundred μK) than through a supersonic expansion, thereby allowing improved momentum resolution, now limited only by detector time and position resolution. Second, target atoms which are unsuitable for supersonic expansion, such as the alkalis and alkali earth elements, are readily laser cooled and trapped. Third, these target species are of necessity readily excited by lasers, allowing for collisions studies on excited as well as ground state targets.

In the Netherlands, Morgenstern and collaborators used trapped sodium as a target for electron capture to highly charged projectiles in the tens of keV range of energy [30]. Shown in Fig. 1.2 is a sample of experimental results for 3 keV/u O^{6+} +

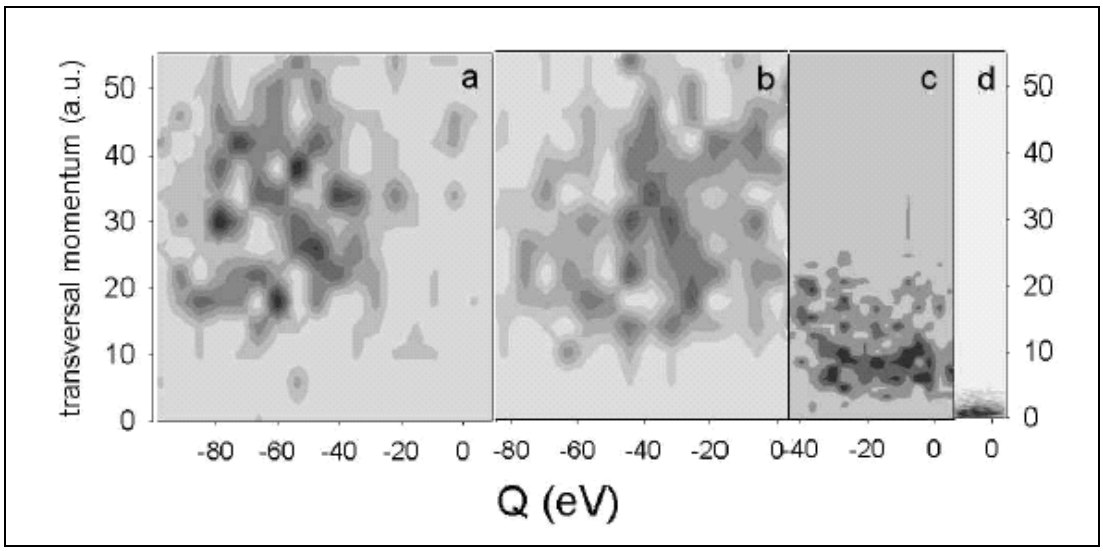

Figure 1.3: *Experimental 2D momentum plots of (a) Na^{4+}, (b) Na^{3+}, (c) Na^{2+} and (d) Na^{+} recoils created by 3 keV/u O^{6+} impact. The experimental results are from Ref. [30].*

Na. These measurements on highly charged ions in collisions with laser trapped atoms are the first of their kind. Clearly seen are the peaks due to multiple capture from the trapped sodium target. The experimental results show good agreement with the over-barrier model. Typical longitudinal momentum resolution, $\Delta P_{\parallel}$, is 0.2 atomic units. Shown in Fig. 1.3 are the intensity distributions of the Na^{q+}(q=1-4) recoil ions as functions of both the transverse momentum and Q-value. The measured transverse momentum distributions are also compare well with CTMC calculations.

Meanwhile, the group of Andersen *et al.* in Copenhagen also used a sodium trap as a target to investigate single electron capture to singly charged projectiles [31]. Figure 1.4 shows a typical longitudinal momentum spectrum for 6 keV Li^{+} + Na($3l$) where l = s and p. Longitudinal momentum resolution, $\Delta P_{\parallel}$, is 0.38 a.u. The studies showed a trend of increasing longitudinal momentum transfer from 0.37 a.u. at projectile velocity, v = 0.135 a.u., to 0.28 a.u. at v = 0.200 a.u. [32].

In Fig. 1.5, Fraunhofer diffraction can be seen in capture cross sections *via* high

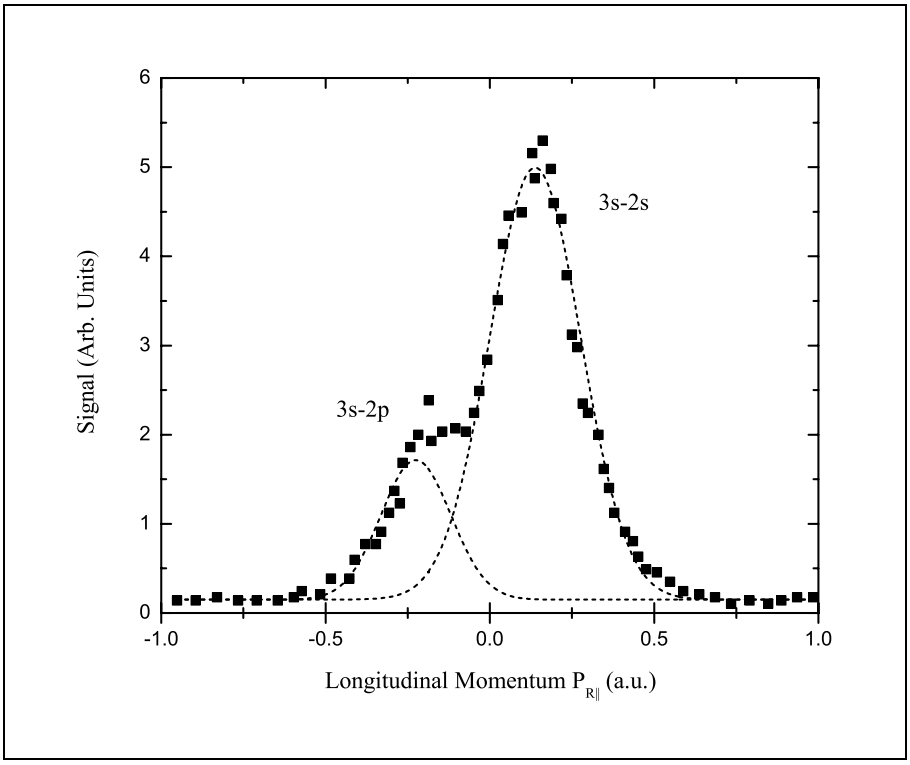

Figure 1.4: *Q value spectrum for Li^+ + Na(3l), where l = s and p, shown as s function of longitudinal momentum transfer. The experimental results are from Ref. [32].*

resolution measurements in recoil ion transverse momentum. A transverse momentum resolution of 0.12 a.u. was reported. Scattering images such as the ones shown in the lower panel of Fig. 1.5 display cylindrical symmetry due to the isotropic initial and final states. A slight asymmetry is seen in the lower panel, indicative of different experimental resolutions along the y- and z-axes. However, by transforming transverse momentum into scattering angle, the differential cross sections can be obtained with a resolution given by the better coordinate (here, the z-coordinate). The scattering patterns are reconstructed and shown in angle space in the upper panel of Fig. 1.5. Angular differential cross sections for Na($3l$)- Li($2l$), where l = s and p, electron transfer in the velocity range v = 0.135 to 0.40 a.u. were also investigated and showed significant improvement in angular resolution compared to earlier results for

this collision system. Atomic orbital as well as molecular orbital coupled channel calculations reproduced the experimental structure well over the range of collision velocities investigated [32].

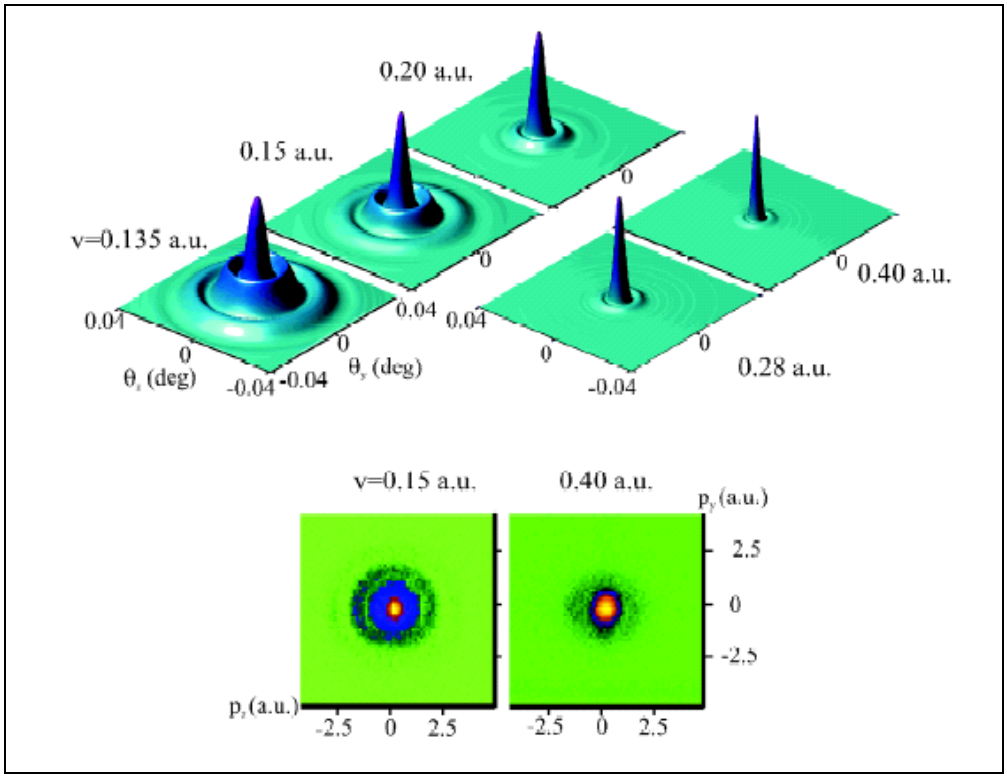

Figure 1.5: *Upper panel: Li angular scattering pattern for $\sigma(\theta, \phi)$ in 3s-2s electron transfer collisions extracted from the coordinate with highest resolution. Fraunhofer diffraction rings are clearly seen. Lower panel: The actual measured scattering pattern in momentum space for two selected velocities. The experimental results are from Ref. [32].*

Concurrently, the work presented in this dissertation was carried out at Kansas State University. A rubidium magneto optical trap is employed as a target for electron transfer studies.

1.3 Overview of Dissertation

In this chapter, some introduction to ion-atom collision has been introduced. The rest of dissertation will be divided into chapters and details relevant to each topic to be discussed: In Chapter 2, a few theoretical approaches are surveyed, including a couple of model calculational methods that will be discussed. These calculations provide an effective means of computing the relative cross sections being measured in the present work. Strong emphasis will be placed on Two Center Atomic Orbital Close Coupling calculation since it has been proven effective in correctly predicting many of the results investigated using MOTRIMS. Highlights of this calculational method will be introduced.

In Chapter 3, complete details of the MOTRIMS apparatus including the recoil ion spectrometer, the magneto optical trap, and the chamber and vacuum system will be given. Details involving all the technical aspect of the whole setup will be laid out to show the connection between the instruments and the measured quantities. The aim of this chapter is to lay down the framework and technical details of MOTRIMS for the benefit of future MOTRIMS users.

In Chapter 4, detailed results and discussion are contained. The primary purpose of the type of experiment done here is to measure relative charge transfer cross sections between singly charged alkali ions and a rubidium target. However, rather than reporting all the differential measurements for many different projectiles at various energies, the aim is to present the most interesting features of the many systems investigated. Also, a novel advantage of the technique, namely using the ion beam as a probe of target dynamics is also presented. Details of the these results will be fully addressed here.

Finally, Chapter 5 concludes this dissertation. A summary of results will be given.

Furthermore, MOTRIMS's potential and its future developments will be addressed. Suggestions for possible interesting experimental projects that could utilize the many capabilities of MOTRIMS technique will be given.

Chapter 2

Theoretical Approaches

As mentioned in Chapter 1, theoretical ion-atom collisions studies can be used to provide physical insights into many collision mechanisms. Many approximate analytical solutions for the study of electron transfer have been developed to provide rapid means of calculating transfer probabilities and to shed light onto the underlying physics phenomena. Here, a few theoretical approaches for calculation of charge transfer cross sections at low energy are presented. To begin, a couple of simpler methods of doing calculations for ion-atom collision will be presented. Along with the many advantages of being simple models, their disadvantages will also be addressed in order to assess the overall effectiveness of the methods. This will be followed by an introduction to a more sophisticated type of calculation normally referred to as a close-coupling calculation. The basic principle behind atomic orbital close-coupling calculations will be provided. It is this method that was used to compare with our experimental results, as will be shown in later chapters.

2.1 Multi-channel Landau-Zener Model

To fully understand the multi-channel Landau-Zener model, let us first discuss the two-state Landau-Zener model [33, 34], where the diabatic potentials are assumed to

be linear in internuclear separation R near the transition, and the coupling between the diabatic states is taken to be constant. Treating the multi-channel charge transfer process as a series of couplings between two states, approximate solutions to the coupled channel problem can be found. The two state coupled channel problem yields two coupled equations

$$\dot{c}_1 = c_2 H_{12} e^{-i \int_{-\infty}^{t} (E_1 - E_2) dt'}, \tag{2.1}$$

and

$$\dot{c}_2 = c_1 H_{12} e^{i \int_{-\infty}^{t} (E_1 - E_2) dt'}, \tag{2.2}$$

where E_1 and E_2 are the energy levels of the two states. H_{12} is the coupling matrix element at closest approach and assumed to be small compared to the relative kinetic energy of ion-atom system. A widely used formula for H_{12} developed by Olson and Salop [35] is

$$H_{12} = \frac{9.13}{\sqrt{q}} e^{\frac{-1.32R}{\sqrt{q}}}, \tag{2.3}$$

where q is the effective projectile charge.

The initial conditions of the system are $|c_1(-\infty)| = 1$ and $|c_2(-\infty)| = 0$. The probability for an adiabatic (non-crossing) transition is given by

$$P_{11} = |c_1(\infty)|^2, \tag{2.4}$$

and so by solving Eqs. 2.1 and 2.2 analytically, Eq. 2.4 becomes

$$P = P_{11} = e^{-2\pi \frac{H_{12}^2}{v_r \Delta F}}, \tag{2.5}$$

where v_r is the radial velocity and ΔF is the difference in the slope of the two potential curves. However, as the ion passes the atom the inter-nuclear separation increase can lead to electron capture on the way out. Therefore, there are two possible sets of paths for electron transfer. The adiabatic transition for the incoming path and the

diabatic transition for the exiting path or a diabatic transition on the way in followed by an adiabatic transition on the way out. Thus, the total probability of electron transfer at a given impact parameter is

$$P_{total} = 2P(1 - P). \tag{2.6}$$

Integrating over all impact parameters, b, the cross section for the two-level case is given by

$$\sigma = 2\pi \int_0^{R_c} bP_{total} db. \tag{2.7}$$

However, among its deficiencies, two-state Landau Zener model does not include rotational coupling; *i.e.* it does not allow molecular states with different Λ-symmetry to be correlated. To fix this problem, one might introduce a locking radius rotational coupling [36, 37, 38]. This R_L defines a region within which the molecular states with Λ-symmetry are allowed to mix. An additional problem in the Landau-Zener model is that translational effects for which the electron has a definite velocity, are not included.

This basic two-level charge exchange concept can be extended to multi-level systems. Assuming that each pseudo-crossing is separated from the others such that a two-state Landau-Zener probability can be applied for each. The net probability is the product of all the probabilities as the system passes through all possible sets of pseudo-crossings:

$$P_{f,i} = S_1 \ldots S_N S_N \ldots S_1 P_i, \tag{2.8}$$

where $P_{f,i}$ and P_i are the sets of final and initial population probabilities for the given set of channels. Details of this model can be found in [36, 39, 40].

2.2 Modified Demkov Model

The linear approximation discussed in the Landau-Zener model led us to an analytical solution of the two-state equations. However, it is not the only way. Here, we consider the Demkov model [39, 41] based on the assumption that the coupling varies exponentially over the transition region. Each transition is treated as a two-coupled-states problem, neglecting the effect of the other final states involved. The coupled equations are

$$i\dot{c}_1 = \alpha c_1 + \beta e^{\gamma t} c_2, \tag{2.9}$$

and

$$i\dot{c}_2 = -\alpha c_2 + \beta e^{\gamma t} c_1. \tag{2.10}$$

For the initial conditions $|c_1(-\infty)| = 1$ and $|c_2(-\infty)| = 0$, the above equations yield,

$$c_1 = \sqrt{\left(\frac{\pi\beta}{2\gamma} Sech(\frac{\pi\beta}{\gamma})\right)} e^{(\frac{\gamma t}{2})} J_{-\frac{1}{2}-i\frac{\alpha}{\gamma}}\left(\frac{\beta}{\gamma} e^{\gamma t}\right) \tag{2.11}$$

and

$$c_2 = -i\sqrt{\left(\frac{\pi\beta}{2\gamma} Sech(\frac{\pi\beta}{\gamma})\right)} e^{(\frac{\gamma t}{2})} J_{\frac{1}{2}-i\frac{\alpha}{\gamma}}\left(\frac{\beta}{\gamma} e^{\gamma t}\right), \tag{2.12}$$

where $J_\nu(\chi)$ is Bessel function of first kind. The coupling between the states is assumed to be

$$H_{12} \simeq \beta e^{\left(-\sqrt{2I}R(t)\right)}. \tag{2.13}$$

Thus by substituting $R(t) = \sqrt{(vt)^2 + b^2}$, where b is the impact parameter, the b-dependence is explicitly introduced, leading to the transition probability

$$P(b) = sech^2\left(\frac{\pi\Delta}{2\gamma}\right) \sin^2\left(\frac{2\beta K_0(2Ib^2)}{v\sqrt{2I}}\right), \tag{2.14}$$

where

$$\gamma = v\sqrt{2I}\sqrt{1 - \frac{2Ib^2}{\ln^2 \frac{\Delta}{\beta}}}, \tag{2.15}$$

and $\Delta = |I_1 - I_2|$. Here, I_1 and I_2 are the ionization potentials of the initial and final states, I is the minimum of I_1 and I_2, v is the collision velocity, $\beta \simeq I$ as suggested by Meyerhof [42], K_0 is a K-Bessel function, and all values are in atomic units. The cross sections of the reaction channels for which $H_{12} \gg \Delta$ are then evaluated by integration over b.

2.3 Semiclassical Close-Coupling

The semiclassical close-coupling theory of atomic collisions has been described by Fritsch and Lin [6] and in Bransden and McDowell [39]. In-depth analysis pertaining to the results obtained in this dissertation can be found in [43]. Atomic close-coupling calculations were employed for many reasons. First, they are easier to implement compared to molecular orbital (M-O) since potential curves, upon which M-O relies, are not well known for many one electron systems. Second, this method is generally reliable, as compared to the classical Over Barrier Model (OBM) where the cross section is reliable only to within an order of magnitude. Third, it compares well with other calculations. In the close-coupling description of atomic collisions, it is assumed that the quantum mechanical states of the electron may vary within the limits of a given space configuration. This method is mainly good for describing dominant processes. Then the question of which states to populate takes on the form of which configurations may significantly be fed from an initial state in course of the collision to a specific final state. For the scattering calculations, the theory as in Kuang and Lin [44] was adopted. The time-dependent wave function is expanded in terms of bound atomic orbitals, plus continuum states on each center, each with appropriate plane wave translational factors. The atomic orbitals are expressed in

terms of even-tempered basis functions

$$\phi_{nlm} = \sum_k C_{nk} N_l(\xi_k) e^{-\xi_k r} \tilde{Y}_{lm}(r), \tag{2.16}$$

where $\tilde{Y}_{lm}(r)$ consist of a spherical harmonics multiplied by r^l, $N_l(\xi_k)$ is a normalization constant, and the orbital exponents ξ_k are taken to form a geometric sequence

$$\xi_k = \alpha\beta^k, \qquad (k = 1, 2, \cdots, N). \tag{2.17}$$

The two parameters, α and β, can be determined by energy minimization. For low energy alkali ion-atom collisions, only the outer electron is active in the charge transfer process. The collision participants are each treated as a one-electron system with the core "frozen". The active electron in each atom is governed by a model potential. The parameters in these model potentials are chosen such that the experimental binding energies of the first few states of interest are well reproduced. In fitting the potential parameters, the wave functions are calculated numerically. Once the potential is chosen, a check is made so as to be sure that the atomic orbitals are adequately represented by combinations of even-tempered functions with properly adjusted α and β parameters. The eikonal approximation is then employed to obtain the differential cross sections [39]. The angle-differential cross section (DCS) for an inelastic transition from an initial state i to a final state f can be written as the absolute square of a scattering amplitude A_{fi} at a given angle θ,

$$\frac{d\sigma_{fi}}{d\theta} = 2\pi sin\theta |A_{fi}|^2, \tag{2.18}$$

where the scattering amplitudes A_{fi} are determined, in turn, from the impact parameter-dependent transition amplitudes, and are given by

$$A_{fi}(\theta) \;=\; \gamma \int_0^{+\infty} bF(b)dbJ_{|m_f - m_i|}(2b\mu\nu sin\frac{\theta}{2}). \tag{2.19}$$

Here

$$F(b) = C_{fi}(b, +\infty)e^{2\frac{i}{\nu}Z_T Z_P \ln b}, \tag{2.20}$$

with $\gamma = \mu\nu(-i)^{|m_f - m_i|+1}$, μ the reduced mass, ν the relative collision velocity and m_f (m_i) the magnetic quantum number of the final (initial) state. The function J is a Bessel function of the first kind, and C_{fi} is the semiclassical transition amplitude, evaluated for a given impact parameter b. The additional phase, $e^{2\frac{i}{\nu}Z_T Z_P \ln b}$, is the eikonal phase due to the Coulomb repulsion between the two nuclei. Z_T (Z_P) is the effective charge of the target (projectile) that defines the Coulomb trajectory of the two colliding nuclei. Since, for system under consideration here, charge transfer occurs far outside the core of both atomic ions, an effective charge of one was used for each.

The total cross section is checked by integration of the DCS over scattering angles. The total charge transfer cross section for each state was obtained from

$$\sigma_{nl} = 2\pi \sum_m \int_0^{+\infty} bdb|C_{fi}(b, +\infty)|^2. \tag{2.21}$$

Detailed results in terms of relative cross section as well as their comparison to experimental results will be presented in Chapter 4.

Chapter 3

Experimental Setup

In this chapter, details of experimental setup will be presented. The aim is to have a comprehensive documentation of all technical aspects of what is involved in doing Magneto Optical Trap Recoil Ion Momentum Spectroscopy. Through knowledge of this description, an understanding of the experimental results should be transparent. To begin, a simple description of the apparatus will be presented and then followed by an explanation of the kinematics in order to show the connection between the experimental setup and the measurements. Highlights of the many advantages of this setup, as compared to the more traditional ways of studying ion-atom collisions, namely COLTRIMS, will be discussed. Details of the beam line, the target, the spectrometer, and the data acquisition systems will be completely laid out to show the "nuts and bolts" of all that is involved.

3.1 Description of Apparatus

The experimental setup is depicted in Fig. 3.1. In the target region, ^{87}Rb atoms are trapped and cooled in a magneto optical trap (MOT) using a diode laser, split into three pairs of counter-propagating beams which operate on the $5^2S_{1/2}$, F=2 - $5^2P_{3/2}$, F=3 transition. A second diode laser is used to "re-pump" on the $5^2S_{1/2}$, F=1 -

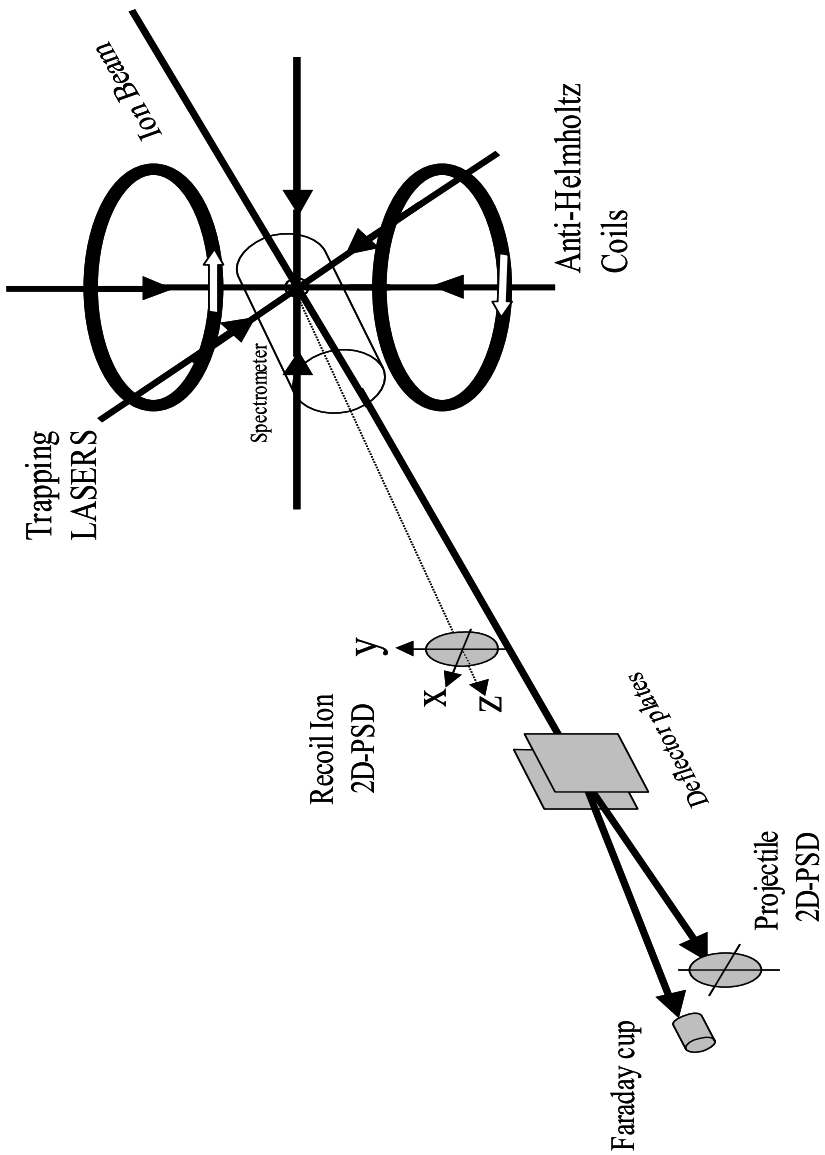

Figure 3.1: MOTRIMS experimental setup.

$5^2P_{3/2}$, F=2 transition. Complete details of laser preparation and implementation are presented in the target preparation section of this chapter. As discussed later, the rubidium target density was measured to be $\sim 4 \times 10^{10}\text{cm}^{-3}$; its diameter was 1.0±0.3 mm; and its temperature was 130±100μK. The trapping magnetic field had a gradient of approximately 5 Gauss/cm. The details of rubidium transitions, trapping magnetic field, and target density are explained in Appendix D. The rubidium was cooled and trapped inside a recoil ion momentum spectrometer whose extraction axis was oriented 3.5^o with respect to the projectile axis. Singly charged projectile alkaline ions are sent in to collide with the trapped target. Charge transfer from the trapped target to the projectile ion is studied. The products of the collision are detected in coincidence in order to reconstruct the collision process. The three momentum components of the recoils are determined, ion by ion, through their flight times, and their positions on a 2-dimensional position-sensitive detector (2-D PSD). The projectiles continue past the recoil detector, and are charge-state analyzed, with the neutral projectiles striking a second 2-D PSD, and the primary beam being collected in a Faraday cup. Details of the detectors are given in Appendix C

3.2 Kinematics

Magneto optical trap recoil ion momentum spectroscopy (MOTRIMS) is the principal tool used in these measurements. This new technique[45, 46, 47], an outgrowth of the more general COLTRIMS (COLd Target Recoil Ion Momentum Spectroscopy)[48, 49, 50, 51] method, enables high resolution Q-value and scattering angle measurements in ionizing ion-atom collisions. Measuring the target 3-dimensional momentum vector by time-of-flight (TOF) and 2-dimensional position-sensitive detection (2D-PSD) techniques, Q-values and scattering angles are determined. For a more complete

treatment of kinematics, including a relativistic treatment, one may find Mergel's dissertation to be helpful [28]. For most ion-atom collisions only a small fraction of the projectile's initial momentum (P_P) , energy (E_P) and mass (M_P) is transferred to the recoil. Also, the momentum of any emitted photons is small. These assumptions are valid for the system presented here. From non-relativistic energy and momentum conservation, one can deduce the kinematics of a collision given the longitudinal and transverse momentum components of the recoil.

Conservation of energy gives rise to

$$E_{initial}^{binding} + \frac{P_{P_{initial}}^2}{2m_P} = \frac{P_{P_{final}}^2}{2m_P} + \frac{P_{R_{final}}^2}{2m_R} + \frac{P_{e_{final}}^2}{2m_e} + E_{final}^{binding} \ , \tag{3.1}$$

where the subscripts P, R and e refer to projectile, recoil, and electron, respectively. The Q value, or energy defect, is defined by

$$Q = \left(E_{initial}^{binding} - E_{final}^{binding}\right) \ . \tag{3.2}$$

Using Eq. 3.1, Eq. 3.2 can be rewritten for the case of single charge transfer as

$$Q = \frac{P_{P_\parallel}^2}{2m_P}\left(1 + \frac{m_e}{m_P}\right) + \frac{P_{P_\perp}^2}{2m_P}\left(1 + \frac{m_e}{m_P}\right) + \frac{1}{2m_R}\left(P_{R_\parallel}^2 + P_{R_\perp}^2\right) - \frac{P_{P_{initial}}^2}{2m_P} \ . \tag{3.3}$$

The symbols $\perp$ and $\parallel$ refer to components perpendicular and parallel to the initial direction of the projectile.

Conservation of momentum gives rise to the following equations:

$$P_{P_{initial}} = P_{P_\parallel} + P_{R_\parallel} + P_{e_\parallel} \ , \tag{3.4}$$

and

$$0 = P_{P_\perp} + P_{R_\perp} + P_{e_\perp} \ . \tag{3.5}$$

From Eqs. 3.4 and 3.5, we can establish the following equations:

$$P_{P_\parallel}^2 = \left(\frac{m_P}{m_P + m_e}\right)^2 \left(P_{P_{initial}} - P_{R_\parallel}\right)^2 \ , \tag{3.6}$$

and

$$P_{P_\perp}^2 = \left(\frac{m_P}{m_P + m_e}\right) P_{R_\perp}^2 \ . \tag{3.7}$$

Incorporating Eqs. 3.6 and 3.7 into Eq. 3.3, one finds

$$Q = \frac{P_{P_{initial}}^2 - 2P_{P_{initial}}P_{R_\parallel} + P_{R_\parallel}^2}{2\left(m_P + m_e\right)} + \frac{P_{R_\perp}^2}{2\left(m_P + m_e\right)} + \frac{P_{R_\parallel}^2}{2m_R} + \frac{P_{R_\perp}^2}{2m_R} - \frac{P_{P_{initial}}^2}{2m_P} \ . \tag{3.8}$$

This equation seems messy; however, we can clean it up with the following approximation.

$$\frac{1}{m_P + m_e} \approx \frac{1}{m_P}\left(1 - \frac{m_e}{m_P}\right) = \frac{1}{m_P} - \frac{m_e}{m_P^2} \ , \tag{3.9}$$

and so, Eq. 3.8 becomes

$$Q = \frac{P_R^2}{2\mu} - \frac{m_e v_{P_{initial}}^2}{2} - v_{P_{initial}}P_{R_\parallel} - \frac{P_{R_\parallel}^2 m_e}{2m_P^2} \ , \tag{3.10}$$

where

$$\frac{1}{\mu} = \frac{1}{m_P} + \frac{1}{m_R} \ . \tag{3.11}$$

Furthermore, we use the approximation that $m_e \ll m_P$. For the collision energies treated in this dissertation, only a small fraction of projectile's initial momentum is transferred to the recoil. Thus, the first term is relatively small compared to the other terms in Eq. 3.10. Neglecting the first and last terms, Eq. 3.10 becomes

$$Q = -\frac{m_e v_{P_{initial}}^2}{2} - v_{P_{initial}}P_{R_\parallel} \ . \tag{3.12}$$

Thus, as Eq. 3.12 shows, one can express the collision Q-value in terms of the recoil ion longitudinal momentum.

The projectile scattering angle is characterized as

$$\tan\theta_P = \frac{P_{P_\perp} + P_{e_\perp}}{P_{P_{initial}} - P_{R_\parallel}} \ , \tag{3.13}$$

where θ_P is the polar projectile scattering angle. Using Eq. 3.5, this becomes

$$\tan\theta_P = \frac{-P_{R_\perp}}{P_{P_{initial}} - P_{R_\parallel}} \approx \frac{-P_{R_\perp}}{P_{P_{initial}}}. \tag{3.14}$$

This last approximation is valid since $P_{R_\parallel} \ll P_{P_{initial}}$. In the small angle approximation, this becomes

$$\theta_P = \frac{-P_{R_\perp}}{P_{P_{initial}}} \ . \tag{3.15}$$

Notice that Eq. 3.15 shows that the projectile scattering angle can be characterized by the transverse component of the recoil ion momentum. The component of recoil momentum parallel to the projectile axis, $\mathrm{P}_{R_\parallel}$, is thus directly related to the Q-value by Eq. 3.12, while the component of the momentum perpendicular to the projectile axis, $\mathrm{P}_{R_\perp}$, is directly related to the scattering angle by Eq. 3.15. Although transverse extraction is more common, our spectrometer was designed for longitudinal extraction so as to optimize the resolution of $\mathrm{P}_{R_\parallel}$, and thus the Q-value. (As is the case for most RIMS systems, the resolution in timing tends to be better than the resolution in position on a 2-D PSD).

3.3 Beam-line and Ion-optics

A schematic of our beam line is shown in Fig. 3.2. The total length is 3.25 meters, occupying a little less than half of the "MOT room" in J. R. Macdonald laboratory. The ion gun, chamber, aperture hole, and projectile detector center are mounted on a straight line in order to allow the proper tuning of an ion beam into the collision chamber, and from there on to the projectile detector.

The ions pass through various ion optics which include, the built-in optics of the ion gun, an einsel lens, a a set of four jaw slits. The focal point of the ion beam is at the aperture on the pusher plate of the spectrometer (to be described later). Ions

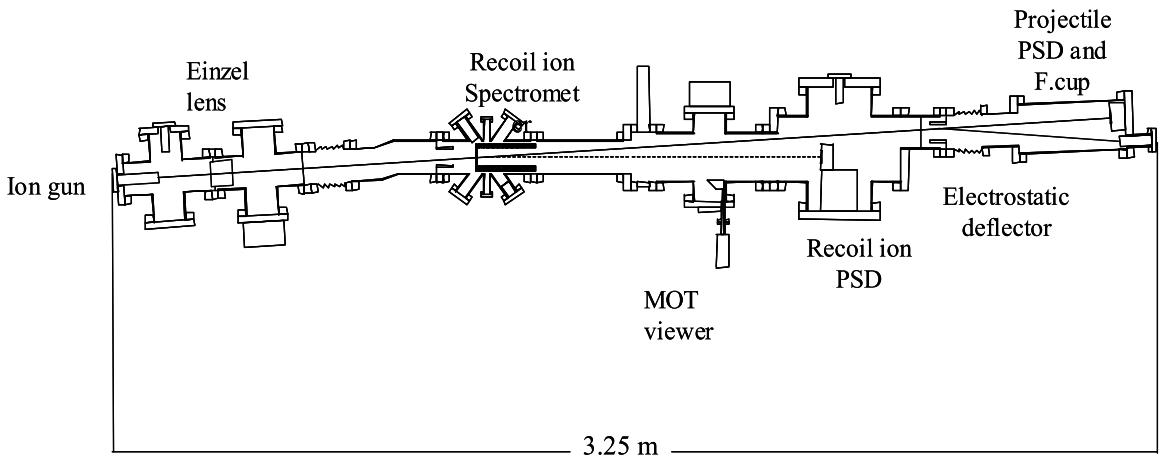

Figure 3.2: Setup schematic.

enter the chamber and intersect the target in the trapping region. The chamber itself is a modified 6-way cross of 4.00 inch tubes (0.083 inches wall) with terminations at three rotatable and three non-rotatable 6 inches con-flat flanges. Additional ports allow access for counter-propagating laser beams to enter the chamber. The delivery system for feeding rubidium into the chamber is mounted on yet another port. A gate valve just after the chamber, is used to separate the upstream and downstream parts of the beam line. A periscope, labelled in Fig. 3.2 as "MOT viewer", is used to give optical access from downstream of the chamber. This helps in the aligning and trapping procedure, especially in the alignment of the horizontal crossing laser beams. Deflector plates are mounted just in front of a downstream bellow to separate the primary beam from the projectiles which have undergone charge transfer.

3.4 Ion Gun

Manufactured by Phrasor Scientific Corporation, the ion source is a complete unit, easy to operate, and easy to maintain [52]. The reader should refer to the manufacturer for answers to technical questions. Some fundamental and operational aspects of ion gun are documented here. A picture of our ion gun unit is shown in Fig. 3.3.

Heating aluminosilicates containing alkali salts to 800-1200 C^o results in the emission of alkali ions. The Phrasor ion source takes advantage of this property by using molybdenum clad pellets of aluminosilicate material to serve as emitters of singly charged ions. The emitter consists of a heated, porous tungsten plug impregnated with an aluminosilicate compound. The heater itself consists of a Re/W alloy mounted inside the molybdenum body and isolated from the body using an Al_2O_3 potting mix. The kinetic energy spread of the emitted ions is less than 1 eV out of 7 keV.

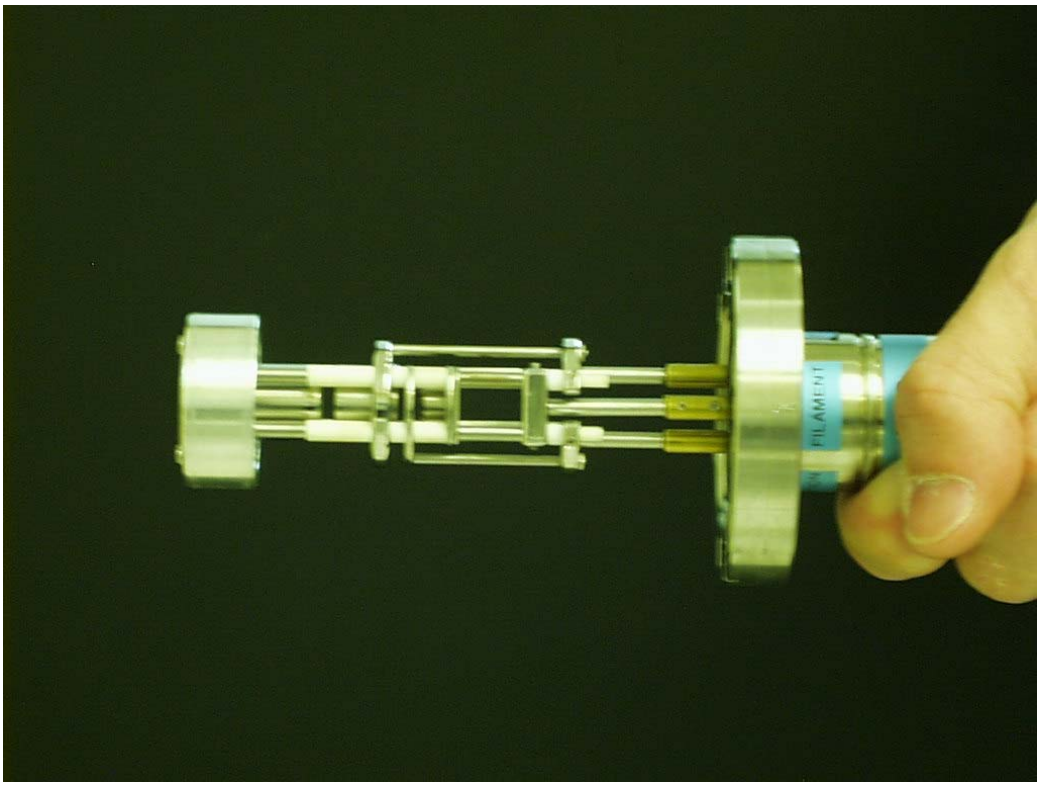

Figure 3.3: *Ion gun image.*

The ion optics of the Phrasor ion source are based on the behavior of so-called triodes used for electron guns. These guns consist of an emitter, counter electrode, and reference electrode. With triodes, the counter electrode serves to modify the potential distribution between emitter and reference, and is usually repulsive to the emitted ions or electrons. Such guns are designed for a single fixed focal point, such as the screen of a cathode ray tube. The Phrasor ion source has an additional lens element consisting of an array of emitter, extractor, focus, and reference electrodes. The potential on the extraction and focus electrodes can be varied making it possible to focus the positively charged ion beam at any distance from nearly zero to infinity. This focusing capability is useful since the distance separating the source from the

trapped target may vary depending on changes in the trapping region. Operationally, the ion gun unit provides a columnated ion beam, typically a few hundred nano-amps at the four jaw slits of our beam line.

3.5 Target Preparation

The usual COLTRIMS target has been replaced by a Magneto Optical Trap. In order to prepare the target, standard laser cooling and trapping methods were utilized. Laser cooling is one of the most important breakthroughs in atomic physics in recent years. Unprecedented control of atoms has resulted in a powerful technique to cool and trap virtually all alkalis, alkali earths, and meta-stable noble gases. Details of cooling and trapping need not be addressed here because the magneto optical trap (MOT) literature is so extensive [53, 54, 55, 56]. However, details of preparing a target for MOTRIMS experiments are outlined here.

3.5.1 Laser Cooling

Essentially, cooling is achieved by using the Doppler effect to make the photon scattering rate dependent on the atom velocity [57]. To do this, the laser is detuned to a frequency slightly to the red of the zero velocity resonance of the atom. As a result of the Doppler shift, atoms moving anti-parallel to the direction of the laser beam will be Doppler shifted into resonance and will scatter photons at a higher rate than those that are moving parallel to the direction of the laser beam. Thus, a larger net force is exerted on the counter-propagating atoms. With laser beams impinging on the atoms from all six directions, the net force is velocity dependent and opposes the motion of the atoms. This provides a strong damping force on atomic motion and cools the atomic vapor. The velocity-dependent forces from a pair of counter

propagating beams are given by

$$F_{\pm} = \pm R\hbar k = \pm \frac{\frac{I}{I_s}}{1 + \frac{4(\Delta \mp kv)^2}{\gamma^2}} \hbar k \gamma, \tag{3.16}$$

giving a net force of

$$F_{total} = F_{+} + F_{-} \ . \tag{3.17}$$

R is the rate of photon absorption, I is the light intensity and I_s is the saturation intensity,

$$I_s \equiv -\frac{\epsilon_0 mc\gamma^2 \hbar\omega}{e^2} \ . \tag{3.18}$$

Also, $k = \frac{2\pi}{\lambda}$ is the wave number, Δ is laser detuning, $\gamma = \frac{1}{\tau}$ is damping rate, τ is the mean lifetime of the excited state, and ω is laser frequency.

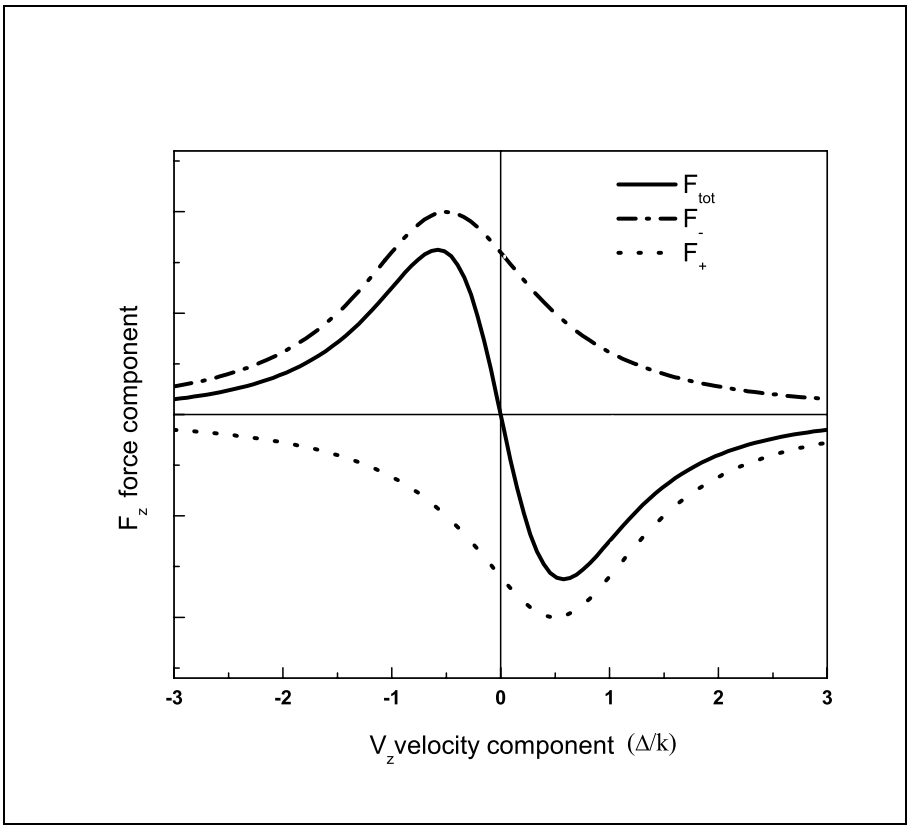

Figure 3.4: *Force on atoms.*

Figure 3.4 shows the radiative force as a function of atomic velocity. Note that the damping force is most effective over a range of velocities between approximately $+\frac{\Delta}{k}$ and $-\frac{\Delta}{k}$.

Diodes lasers at 780 nanometers provide the damping force needed to cool and trap ^{87}Rb. The ground state $5^2S_{1/2}$ is hyperfine split into F=1 and F=2. The upper state in the trapping cycle is the highest hyperfine (F=3) level of the $5^2P_{3/2}$ state. Occasionally, the $5^2P_{3/2}$, F=2 state is populated through off-resonant absorption. This has a non-trivial probability of decaying to the F=1 ground state. This "optical pumping" process would quickly places all the atoms into the F=1 ground state where they are no longer accessible to cooling and trapping laser. Thus, a second laser is employed to excite the F=1 ground state to the F=2 excited state in order to "repump" electrons back into the trapping cycle.

External Cavity Diode Laser

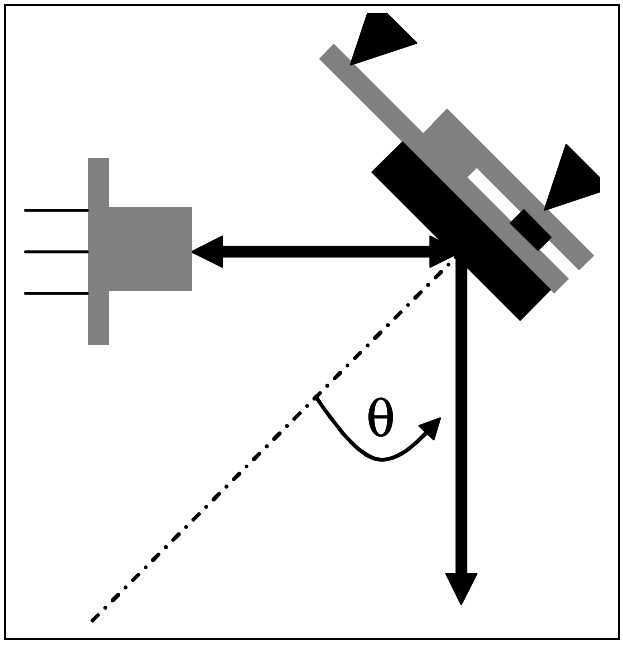

Figure 3.5: *External cavity diode laser in the Littrow configuration.*

The external cavity diode lasers used in this work, roughly follow the design of Ricci [58]. To obtain a spectrally narrow line width, an external cavity having optical feedback from a diffraction grating in the Littrow configuration is used. The zeroth order diffraction is the output beam, while the first order is directed back into the diode. This configuration is illustrated in Fig. 3.5. The diffraction grating equation is

$$d\left(\sin\theta_m - \sin\theta_i\right) = m\lambda, \tag{3.19}$$

where d is the line spacing, θ_m is the angle normal to the mth order of diffracted beam and θ_i is the angle normal to the incident beam. The diffraction grating used has 1800 lines per millimeter. The condition for which the first order is directed back to the diode is

$$2d\sin\theta = m\lambda, \tag{3.20}$$

where θ is the output angle for a wavelength λ. The 780 nm Phillips CQL7825 laser diode is used in the master laser box. For the re-pump laser box, a Phillips CQL7840 is used. The typical tuning range for the master is 5 nm. The master laser diode output power characteristics are shown in Fig. 3.6, while those for the repump laser are shown in Fig. 3.7. Commercial laser heads are readily available from many manufacturers. [59, 60].

Master-Slave Arrangement

The choice of this master-slave arrangement for the trapping laser allows flexibility in power and polarization [61]. The arrangement is shown in Fig. 3.8. Here, control of the master laser is essential since it is the master that injection-feeds and thereby determines the output frequency of the slave. The primary advantage here is that only a small amount of stable master power laser is needed to control the total output of the slave. By using the master-slave combination, we were able to create a laser

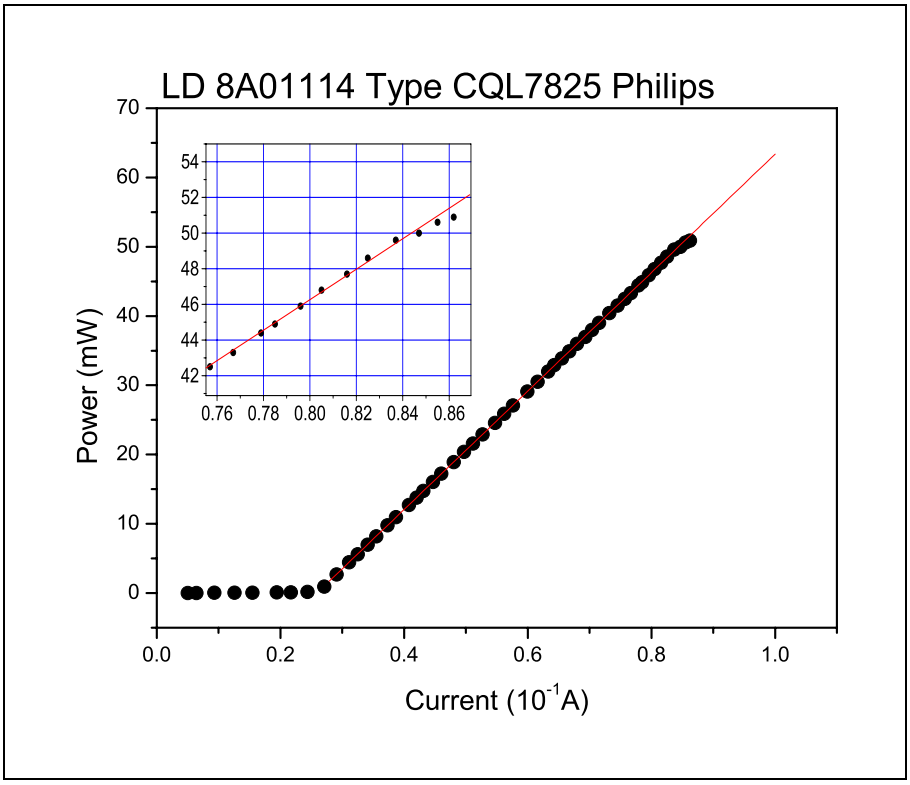

Figure 3.6: *Power characteristics of the diode used in the master laser.*

beam with both a narrow frequency range and high output power. The difficulties with the master-slave apparatus involve the injection of the master laser into the slave and the extraction of the resultant slave beam. For the slave to follow the master frequency, the master must be well aligned with the slave. Unfortunately, due to spurious reflections off optical surfaces, this can result in the formation of an unwanted external resonant cavities which can disrupt the frequency of the master laser. The solution to this problem is to use a series of lenses, beam splitters, and Faraday rotators to isolate the master laser from any reflected beams. Typical injection power into the slave is about 5 mW. Polarization of the injected beam is shown in Fig. 3.9.

Typical output from the slave laser is 70 mW. The higher the slave output the better since this beam has to pass through many optical elements before entering the trapping chamber. Typical required trapping beam power (before splitting) for a

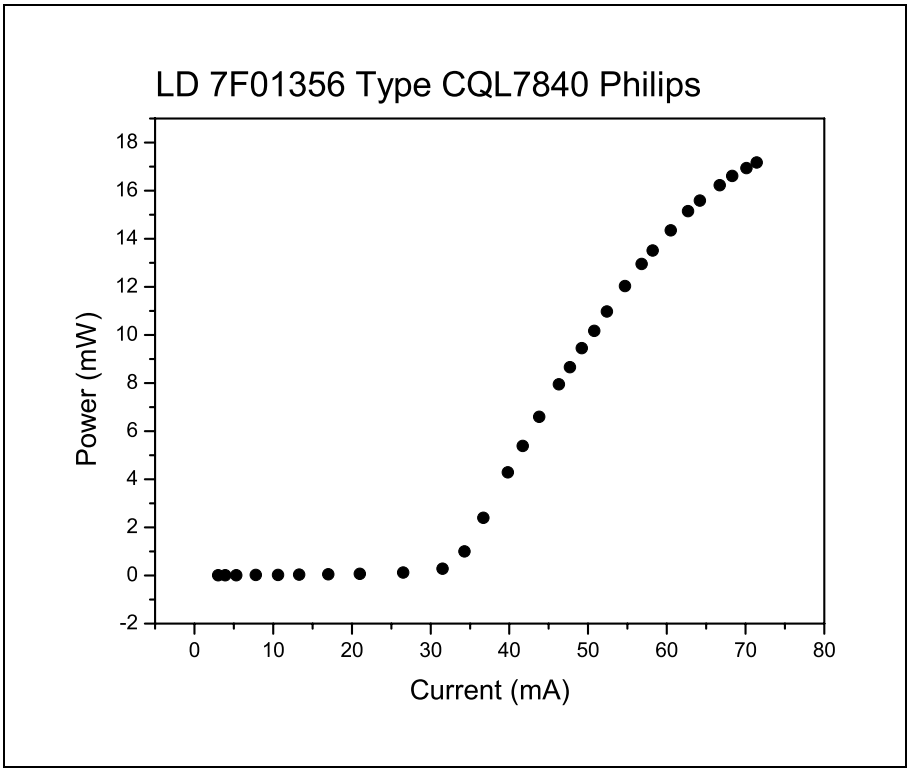

Figure 3.7: *Power characteristics of the diode used in the repump laser.*

reasonably dense target is 6 mW.

Acousto-Optical Modulator

Details and technical aspects of AOMs (acousto-optical modulator) are available through the manufacturers [62]. Here, only the operational aspects of the AOM are presented. The AOM used in this experiment creates sound waves in the lead molybdate crystal which can diffract an optical electromagnetic wave. The lasers are arranged such that the diffracted light is steered into the trapping region. Thus, in the absence of acoustical input, no light gets into the target region. The diffracted light is frequency-shifted by the acoustical frequency, here +80 MHz. A TTL signal is sent to both the AOM controller and the computer to chop and record the laser on and off time, respectively. From experimental experience, total number of trapped

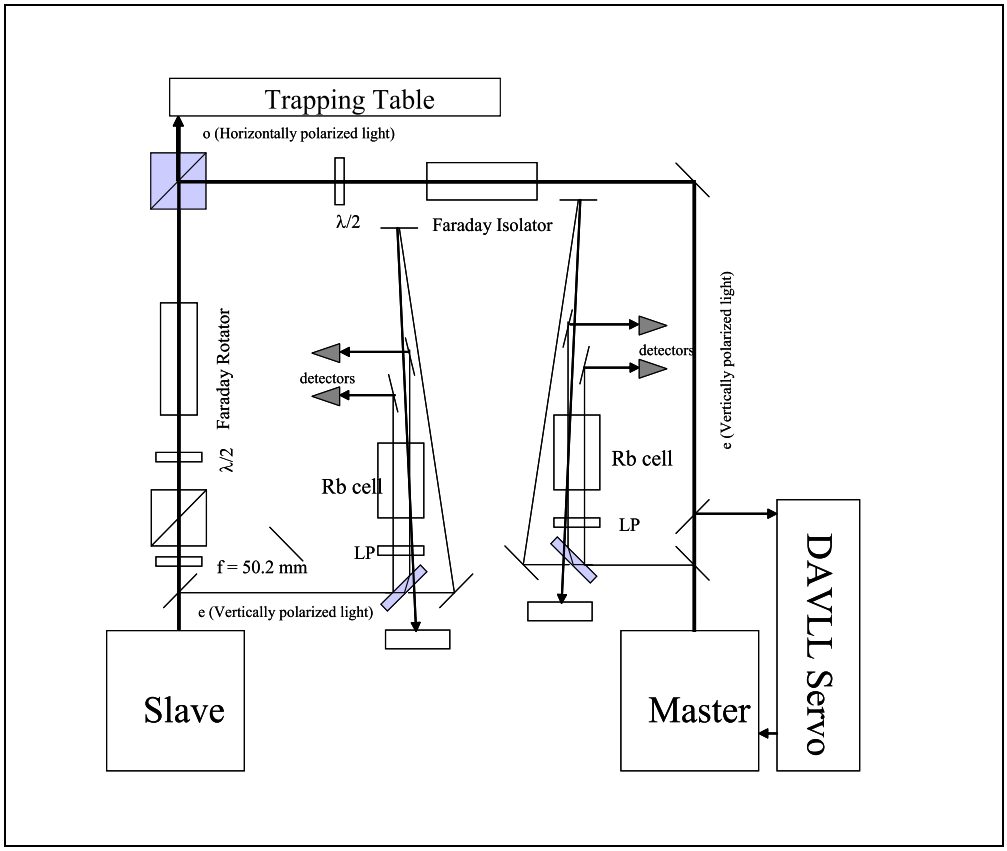

Figure 3.8: *Master-slave configuration.*

atoms in the MOT varies when the lasers are chopped on the millisecond time scale as will be shown in Chapter 4. Therefore, the laser beams were chopped on tens of μs timescale in order to keep the MOT population roughly constant. Acting as an optical shutter AOM works well in chopping the laser beams on this timescale. Rise and fall times for the optical beam are on the order of a few tens of nanoseconds. Two modes of operations with respect to the AMO were employed. Double-passing the AOM was installed as in Fig. 3.10 in order to to cool and trap as well as detune the lasers. In this configuration, the trapping laser is passed through the AOM twice. However, for each pass, laser power is lost and double passing becomes counter productive in making a thick target for collision studies. Therefore, single pass AOM optics were ultimately used as in Fig. 3.11. Here, the slave and the repump lasers are

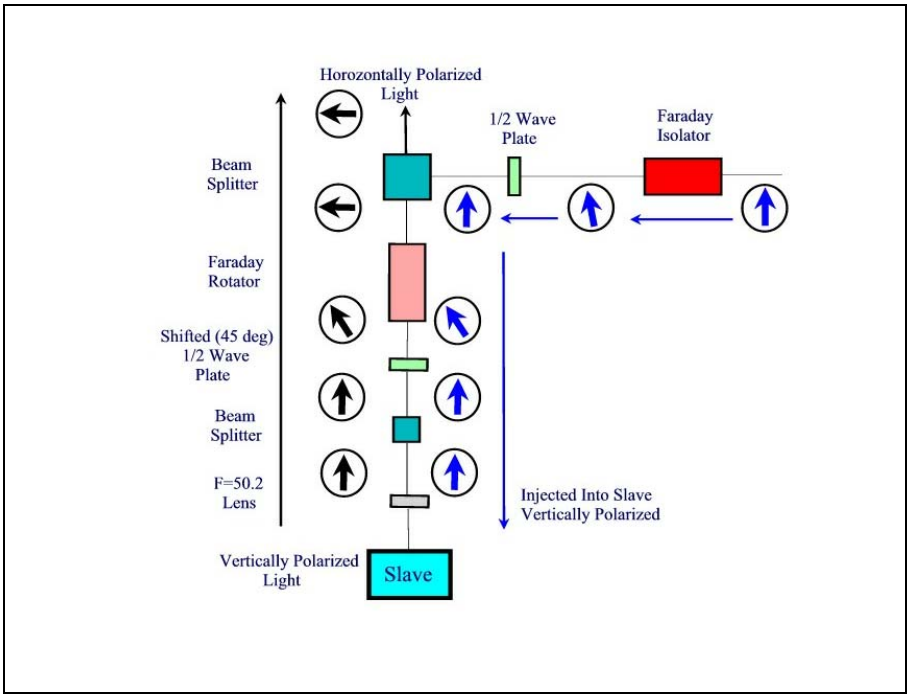

Figure 3.9: *Injection polarization.*

combined before entering the AOM module. Thus, both lasers are chopped.

Trapping Optics

After passing through the AOM, trapping laser beams must be prepared to ensure proper polarization before entering the trapping chamber. The power is equally separated into three beams *via* two sets of half-wave plate and polarizing beam splitter combinations as shown in Fig. 3.12. The quarter-wave plates are to convert the linearly polarized light into circularly polarized light before they interact with the rubidium in the chamber. This arrangement then provides the three dimensional velocity-dependent force needed for trapping. Proper alignment of these counter propagating laser beams is critical to the operation of the magneto optical trap. The intersection region of the three beams must be exactly at the position where the magnetic field is zero. For alignment, the MOT viewers, consisting of strategically placed

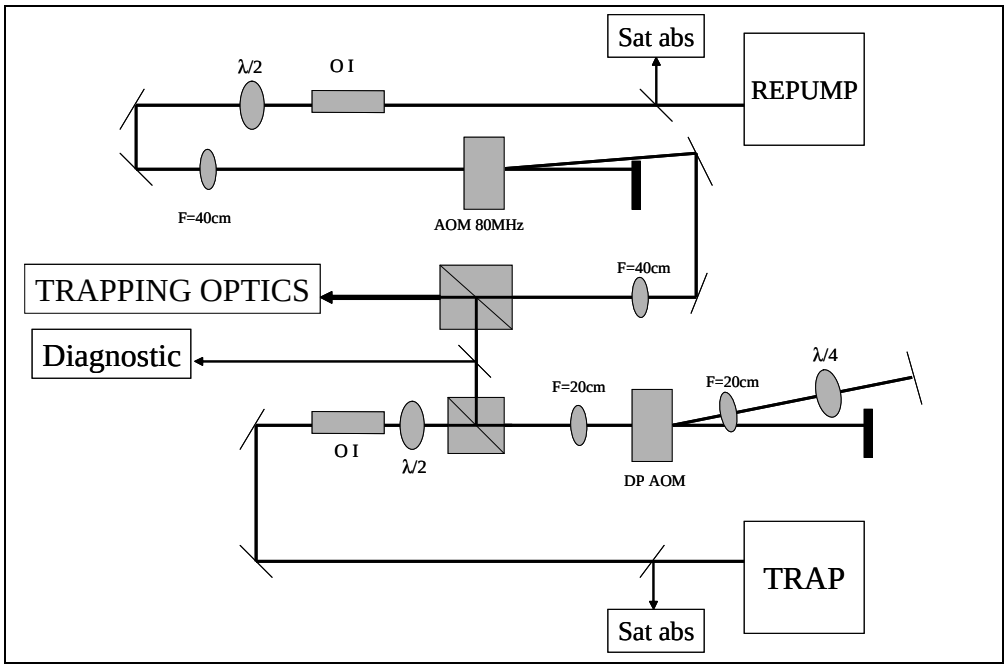

Figure 3.10: *Double-passing optics layout.*

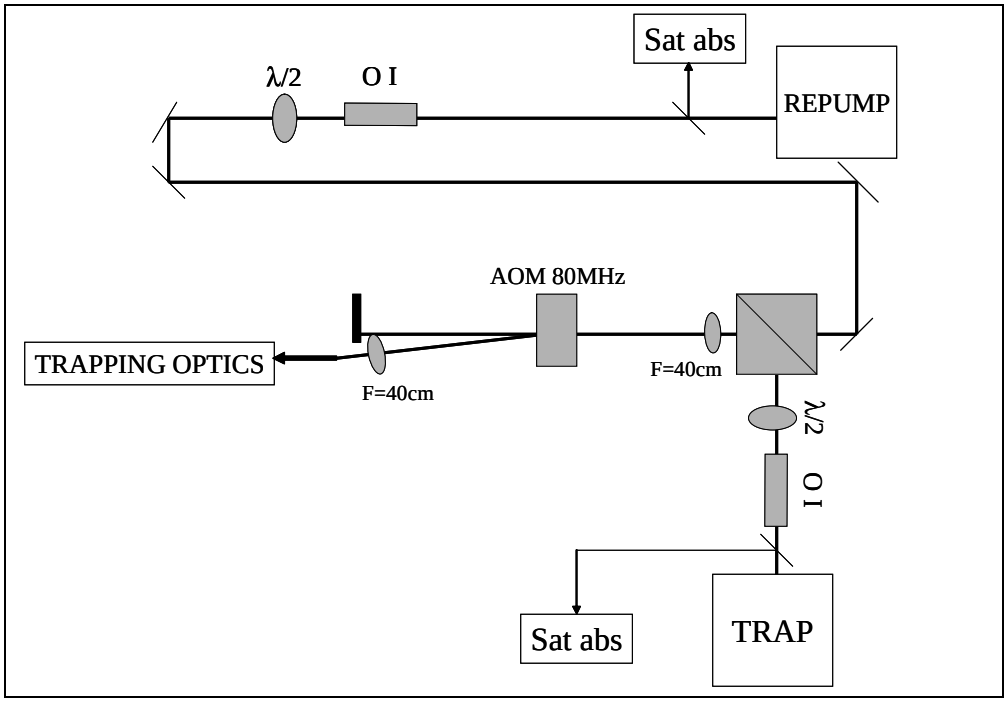

Figure 3.11: *Single-passing optics layout.*

CCD cameras, can be used to make sure two of the beams are horizontal with respect to the chamber, and the third beam is exactly perpendicular to the other two. A CCD camera placed on a side port of the chamber can also be use to make sure that the MOT position is actually at the 6th electrode. This is the location for which the recoil ion spectrometer was designed to optimally time and spatially focus the recoil ions.

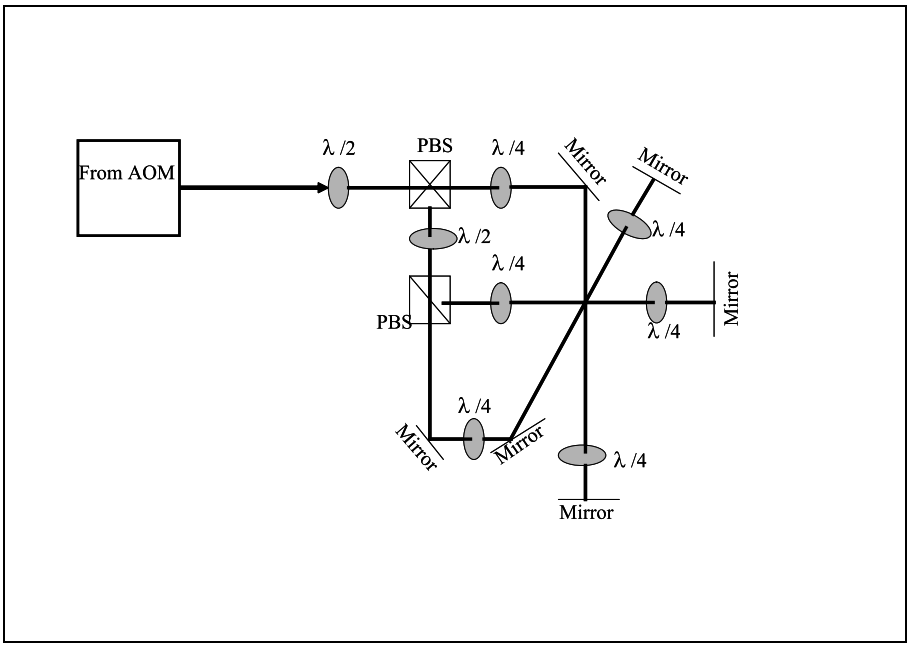

Figure 3.12: *Trapping optics.*

3.5.2 Trapping Magnetic Field

With only a velocity-dependent force, the cooled atoms can still drift away. Therefore, a position-dependent force is applied to maintain the atoms in the collision region. This position-dependent force is applied by the use of the appropriately polarized laser beams and an inhomogeneous magnetic field, which is created by a pair of anti-Helmholtz coil made from water cooled copper tubing. Positioned above and below the collision chamber, these coils can be moved to position the MOT as desired. The

trapping magnetic field gradient is approximately 5 Gauss/cm.

For simplicity, let us consider an atom with a $j = 0$ ground state and $j = 1$ excited state, illuminated by counter propagating right and left circularly polarized beams as illustrated in Fig. 3.13. Because of their angular momentum, right circularly polarized beam can only excite the $\Delta m = +1$ transition, while left circularly polarized light can only excite the $\Delta m = -1$ transition. The magnetic field is zero at the center, and increases and decreases linearly in the positive and negative z direction, respectively. This field Zeeman-shifts the energy levels so the $\Delta m = +1$ and $\Delta m = -1$ transitions are shifted in opposite direction. Let suppose that the atom is to the left of the origin, and laser frequency is below all the field-free atomic transition frequencies. Many photons are then scattered from the σ^+ beam because it is close to resonance. The σ^- is far from its resonance and therefore scatters fewer photons. The resultant force pushes the atom back to the zero field region. The same process shifts the atoms at the right of the origin back to the center.

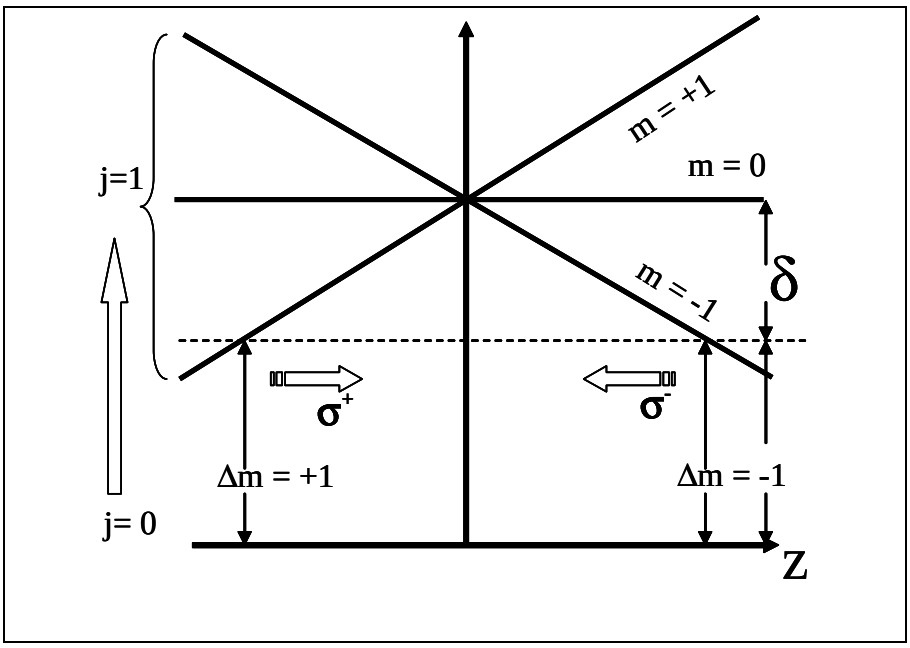

Figure 3.13: *Position-dependent force.*

The magnetic field along with the overlapping of the six laser beams control the position of the MOT. Therefore, operationally, the top coil can be moved in order to properly place the MOT position at the 6th electrode to ensure the over lapping of the target with the projectile beam.

3.5.3 Rubidium Source

Rubidium is introduced into the chamber *via* a reduction source from SAES Getters [63]. These sources contain a mix of alkali metal chromates (Rb_2CrO_4) with a reducing agent to provide sources of small amounts of alkali metals normally used for the preparation of alkali photocathodes. The reducing agent also prevents active gases, which are produced during the reduction reaction, from contaminating the alkali metal vapor. The reduction reaction and hence the rate of alkali production is controlled by applying a current to a heater wire which runs through the dispenser. There are many advantage in using this type of alkali metal dispenser since it consistently reproduces yields, with low gas emission, easily controlled evaporation, and absence of loose particles. The reduction source is mounted 15 cm away from, and directed toward, the collision region. Because the chamber is constructed of stainless steel, and thus continuously absorbs rubidium, the rubidium vapor pressure drops immediately upon stopping the heater wire current. Typically, the heater wire current is set between 4 and 5 Amps. Run continuously at this rate, a single source canister has an active lifetime of about 200 hours.

3.5.4 Magneto Optical Trap Characteristics

Technical details for achieving a magneto optical trap, as well as its characteristics are presented in Appendix D; However, highlights of MOT characteristics are appropriate here. An digitized image of the MOT fluorescence is shown in Fig. 3.14. The three

MOT characteristics that are relevant to the experiments conducted within the scope of this dissertation are temperature, density, and excited-state fraction.

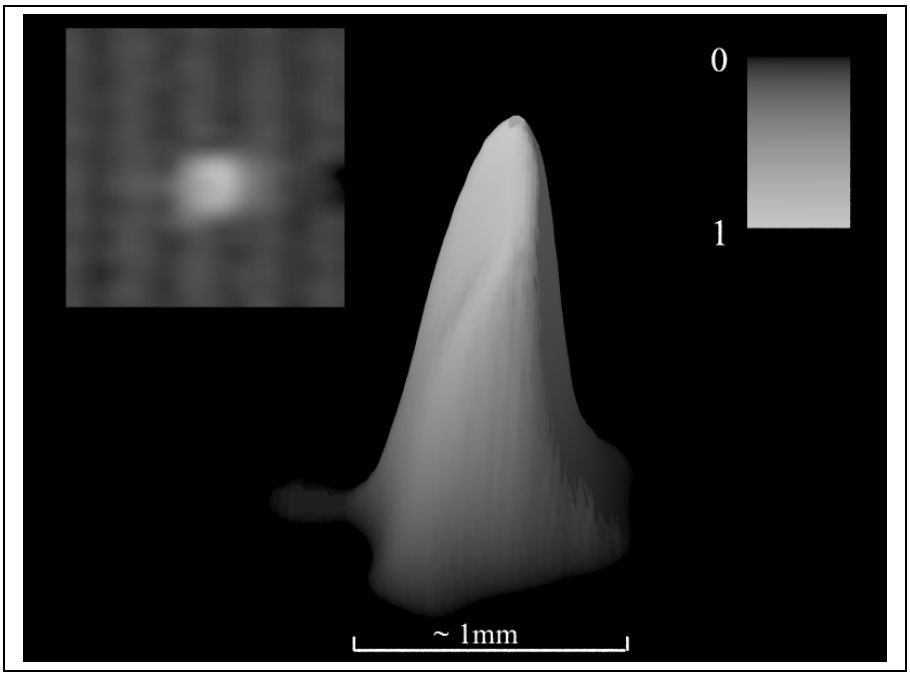

Figure 3.14: *Magneto Optical Trap.*

MOT Temperature

Precise measurement of target atom temperature is not necessary for the operation of this apparatus, since for any atoms cold enough to be held in the MOT, the system resolution is no longer limited by target momentum spread, but rather by timing and detector resolution. Nevertheless, it is interesting to know the approximate temperature. Several techniques can be used to measure the temperature of a MOT. We use the release and recapture method: The re-pump laser is turned on and off using a mechanical beam chopper or an AOM. Within 1.4 ms the atoms are optically pumped to F=1 of the ground state. No longer held in the trap, the atoms fall under the influence of gravity. At the same time, the cloud of atoms expands ballistically. At a later time, the re-pump beam is turned back on, some fraction of the atom

cloud is re-captured in the MOT, and its fluorescence is measured with a photodiode. The fraction of atoms recaptured is a function of delay time, laser beam size, initial cloud size, and final cloud size, the difference in cloud size being a function of the temperature of the atoms. The fluorescence is therefore measured as a function of delay time, and fit to this function. The fit, shown in Fig. 3.15, yields a temperature of 130μK $\pm$100μK.

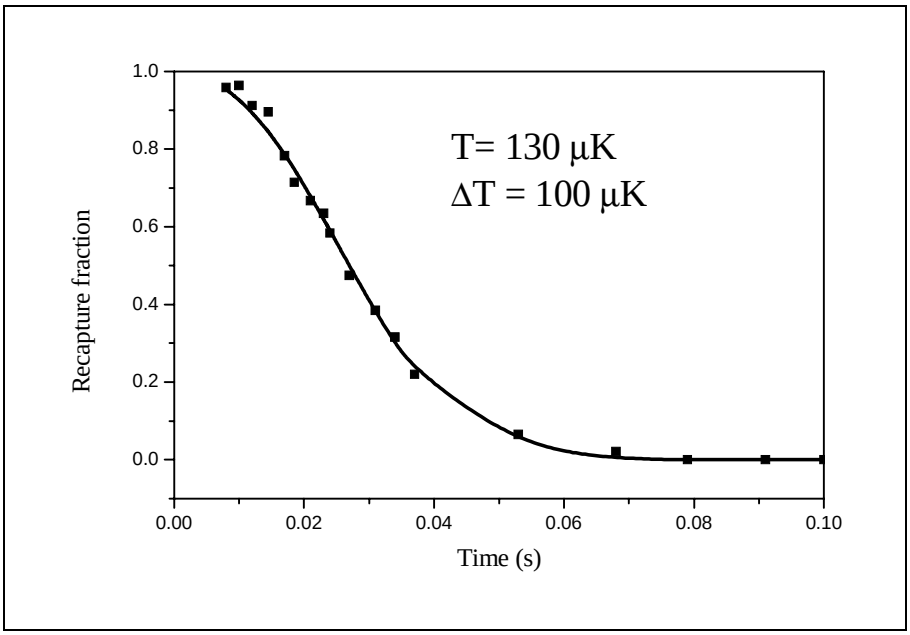

Figure 3.15: *Magneto optical trap temperature determination.*

MOT Density

Because the ion-atom collision rate is proportional to target thickness, an important characteristic of the target is its density. The density is defined as the total number of atoms divided by the target volume. The total number of atoms is roughly determined by measuring the target fluorescence using a calibrated photo-diode subtending a known solid angle, and dividing this result by the excited state fraction. The spatial dimensions of the target are measured with a calibrated CCD camera. Typical target

densities, thus determined, are of the order of $\sim 10^{10}$ atoms/cm^3. If absolute target number (or density) were a critical parameter, a second, more precise method [64], which makes use of a probe laser, could be used. In the apparatus described here, the overlap between ion beam and target is not well characterized. Thus, an approximate density determination is sufficient.

Excited State Fraction

For many experiments of interest, a precise measurement of the target's excited state fraction is required. The usual expression used in determining the fraction of excited atoms [65] is

$$f = \frac{\frac{I_t}{I_s}}{\frac{2I_t}{I_s} + 4(\frac{\Delta}{\Gamma})^2 + 1}, \tag{3.21}$$

where typically, $I_t = 20mW/cm^2$ is the total intensity of our trapping laser beams. I_s is the saturation intensity which, for equally populated m_F levels, is 7.6 mW/cm^2. Δ is the laser detuning from resonance and Γ is the transition linewidth, here, $2\pi \times$ 5.9 MHz. Within this two state model, Fig. 3.16 shows how the excited state fraction depends on both trapping laser intensity and detuning.

Unfortunately, the expression for the scattering rate is believed to be accurate only to within a factor of 2 since it is based on a single laser, single transition model. The uncertainty lies in the unknown m_F distribution, and therefore the actual values for I_s and Γ. Nevertheless, we have used this method to estimate that our typical excited state fraction is greater than 15%. The MOTRIMS system allows for a much more elegant and accurate determination of excited state fraction, which will be described later in this work.

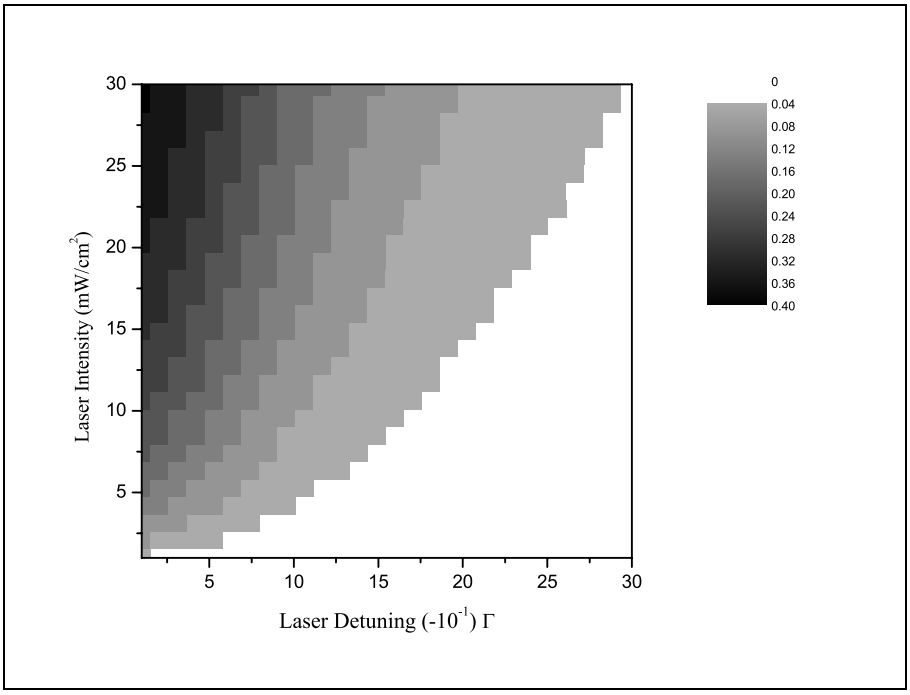

Figure 3.16: *Magneto Optical Trap theoretical excited state fraction as a function of both the trapping laser intensity and detuning.*

3.6 Momentum Spectrometer

The recoil ion momentum spectrometer, shown schematically in Fig. 3.17 is one of the key elements of the apparatus used here.

Simply stated, the spectrometer functions by extracting recoil ions from the collision region using an electric field, and collects them on a PSD (position sensitive detector). The ion's time-of-flight (TOF) is linked to $P_{R_\parallel}$, and its position on the PSD, is linked to $P_{R_\perp}$. In order to reduce the contribution of the collision region's finite size and thus to optimize the spectrometer resolution, the extraction field geometry and the PSD placement have been chosen to achieve three dimensional spatial focusing conditions. With these conditions, the TOF and the coordinates of the ions on the PSD no longer depend (to first order) on the position at which the ions were created. If the spectrometer were only for TOF measurements, one could use the

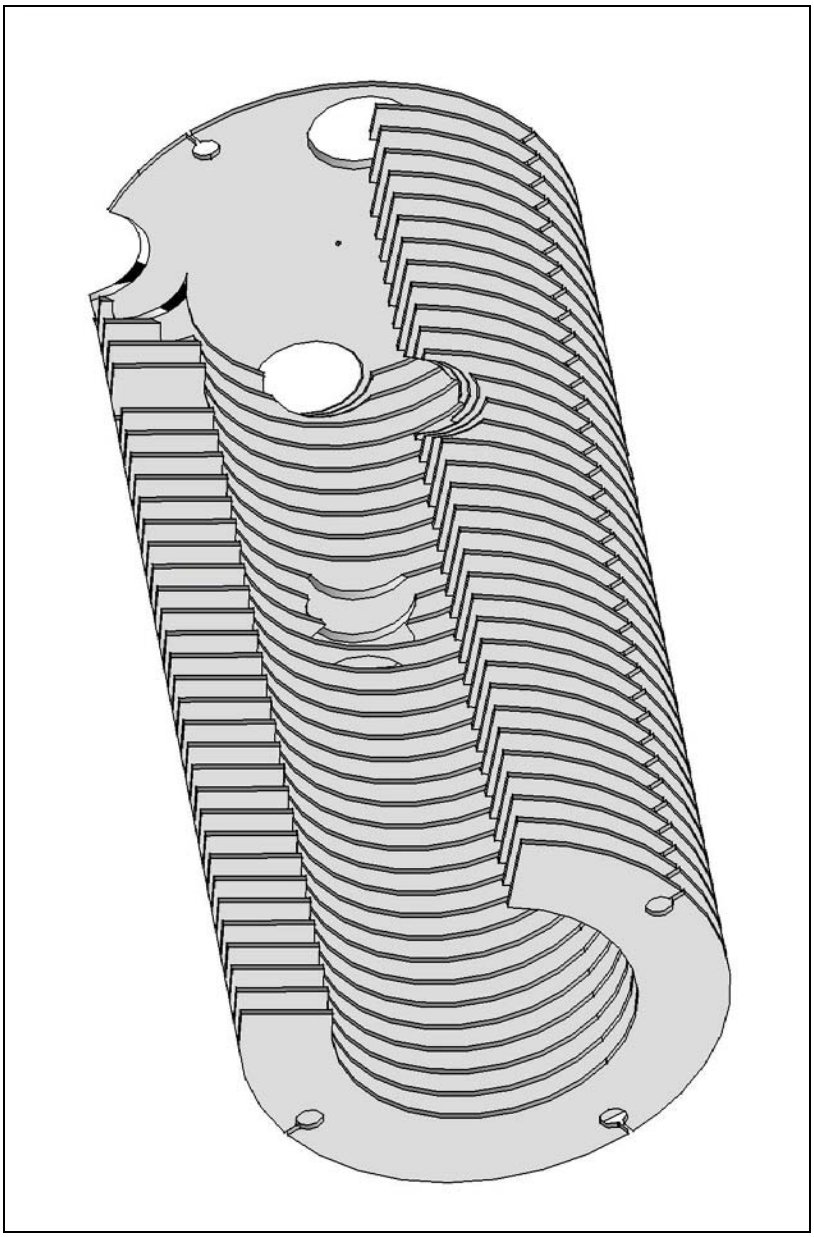

Figure 3.17: *Cut away view of the spectrometer.*

Wiley-McLaren configuration [66] which can be described with a simple closed-form expression; three dimensional focusing requires numerical simulation. Such a simulations was done using the software SIMION [67] in order to determine an optimal geometry and electric field values for the spectrometer. More details on this simulation are presented in Appendix B.

The spectrometer consists of one solid plate (the "pusher") and 34 parallel bored brass plates (effectively "rings") each 1 mm in thickness, having outer diameters of 85.0 mm, and inner diameters of 53.0 mm. A 4.2 mm gap exists between adjacent electrodes (5.2 mm center-to-center). Adjacent electrodes, numbered from 0 to 34, from the pusher to the final grounded element, are connected by 1 MΩ resisters. Electrodes 0 through 15 have had some sections of their diameters cut out to allow for a 15 mm diameter pathway for the trapping laser beams which intersect in the center of electrode 5, in a volume referred to as the collision region. A "pusher voltage", V_p, is applied to electrode 0, and an independent potential, referred to as the focus voltage, or V_f, is applied to electrode 16. The final electrode, number 34, is grounded, as is the front of the PSD, located 1024 mm downstream from the collision region. The entire electrode assembly is enclosed in a 102 mm i.d. grounded tube. Thus, three separate electric field regions exist in the spectrometer: the constant field extraction region, the constant field "focus region" and the field-free drift region. A cut away drawing of the assembled spectrometer is shown in Fig. 3.17, and a photograph is shown in Fig. 3.18.

3.7 Detectors

Detectors used in this work are based on micro channel plate technologies [68]. They have proven to be versatile, routinely used to detect x-ray, photons, electrons, ions,

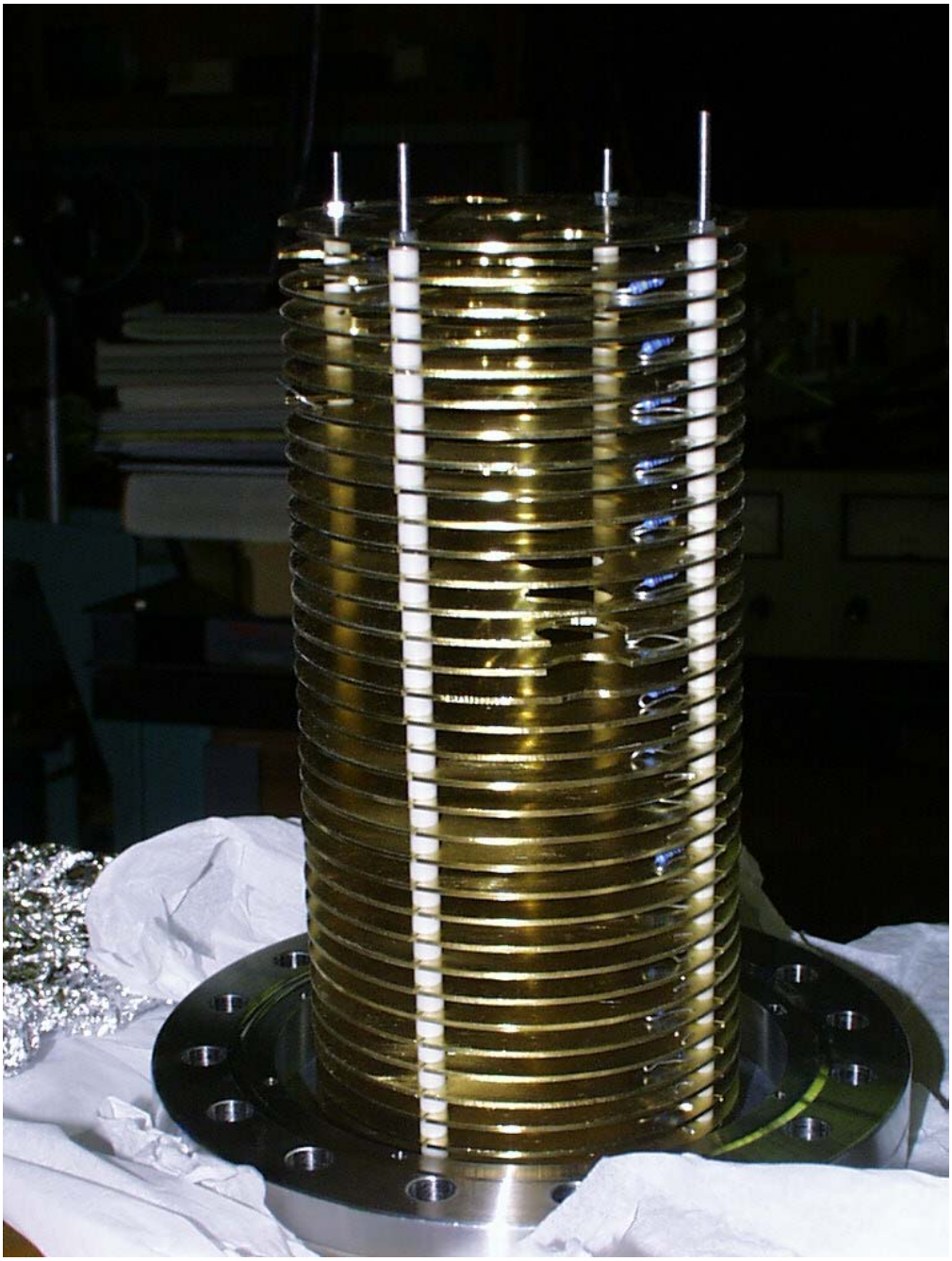

Figure 3.18: *Actual image of the spectrometer.*

and energetic neutral particles. The behavior and characteristic performances of these type of detector are well understood. A resistive anode two dimensional position sensitive detector is used here to detect the recoil ions [69]. A backgammon anode two dimensional position sensitive detector is used to detect neutralized projectiles [70]. Testing of these detectors for their efficiency and resolution involves using an alpha particle source and a mask with known dimensions. Details are in Appendix C. Mentioned here are the highlights for the detector characteristics. Because the recoil ions were of such low energy, and the projectiles were neutral (following charge transfer) three 40 mm diameter channel plates (MCPs) were used in the high gain Z-stack configuration for both position sensitive detectors. A copper mesh was placed in front of the MCPs to insure that the recoil drift region remained free of the electric fields generated by the detector bias voltages. The electro-formed mesh was specified [71] at 333 wires per 2.54 cm, and 70.0 % transmission. As these detectors are well-described in the literature, no further discussion will be given here, except to note that the spatial resolution achieved in this apparatus ($\sim$0.250 mm) for both detectors is not as good as the ($\sim$0.05 mm) claimed by other groups [72]. Thus, in principle, the MOTRIMS resolution in $P_{R_\perp}$ and hence scattering angle could be made even better.

3.8 Coincidence Detection

In order to determine the $P_{R_\parallel}$, the recoil flight time must be measured. To do this, the neutralized projectile hits the projectile PSD and starts a TDC (time-to-digital converter) after which the recoil ion hits its PSD and stops the TDC. In order to set appropriate "coincidence window," the appropriate flight times for both the recoils and projectiles must be known. Figure 3.19 shows the calculated delay time for the

recoil ion to arrive after the arrival of the projectile. Figure 3.20 is a schematic illustra-

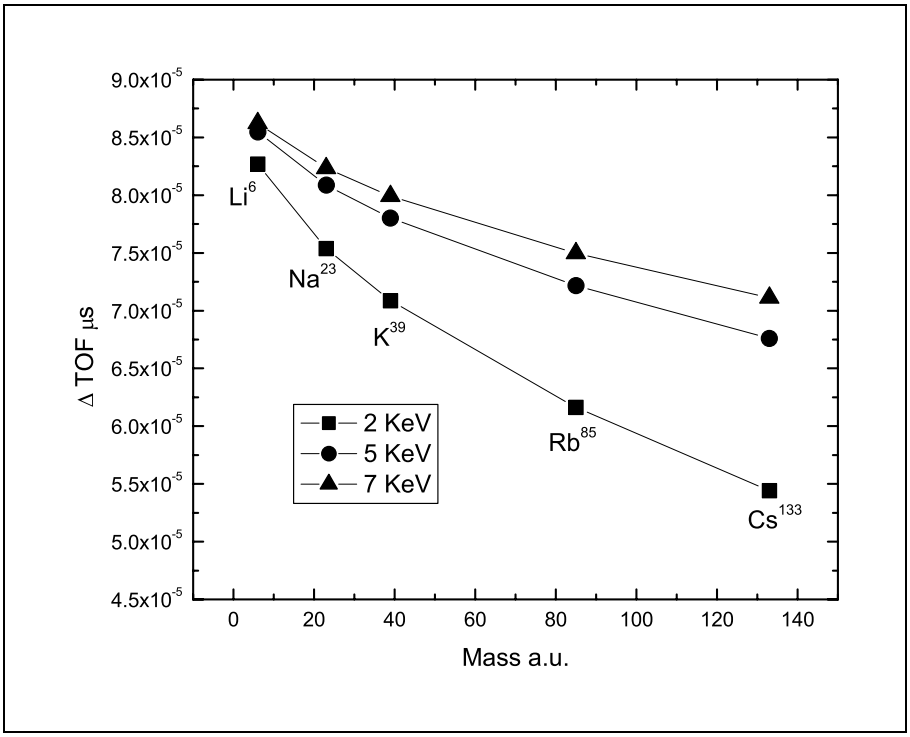

Figure 3.19: *Calculated delay time for different projectile ions.*

tion of the sequence of the signals generated when a projectile strikes its backgammon anode on the projectile detector. This pulse, besides starting the TDC, is delayed and stretched to produce (1) a strobe for the projectile PSD; (2) an "EOW" (End of Window) signal for the TDC; (3) a strobe for the recoil PSD; (4) and a TDC "veto". All of these delays and widths are individually set by separate gate and delay modules. The veto is actually a window inside of which coincidences are recognized. This window is typically set at 2 - 3 μs. When a recoil ion arrives at the detector within the properly set window, a coincidence is registered. The end of window pulse indicates to the computer the end of an event.

A schematic of the electronic setup is shown in Fig. 3.21. The backgammon anode projectile detector records time and position: the time signal is derived from the

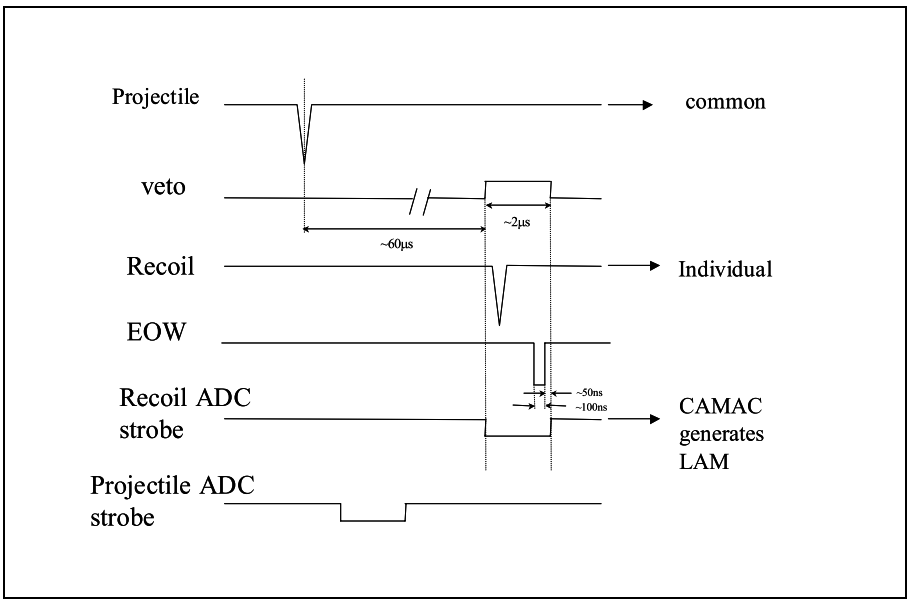

Figure 3.20: *Coincidence detection electronic logics.*

MCPs, while the X, Y, and R outputs give position information for the projectile. These outputs are sent to in-house Pre-Amplifiers, followed by Tennelec TC247 spectral amplifiers. The three components are sent into a CAMAC crate-mounted Ortec 811 ADC to be read by the computer. Meanwhile, the timimg signal is sent to a fast pre-amplifier whose output feeds a constant fraction discriminator, CFD. From the CFD, the projectile time signal is sent to a LeCroy 4208 TDC common input (the "start") the ADC strobe, and a gate and delay box whose output goes into a coincidence module. Similarly, the recoil ion signal is processed. However, the time signal from the recoil ions are sent to the TDC individual ("stop") and, after an appropriate delay, to the coincidence module. The position signals of the recoil ions are sent to the recoil ion ADC.

In order to record both the arrival time of the recoil ion for an event and to determine if that event is for laser on or off, a TAC setup as in Fig. 3.22 is required. A TTL signal generated, for example, by a function generator, is sent to the AOM controller to turn on and off the lasers. It is also sent to the start of a TAC. The stop

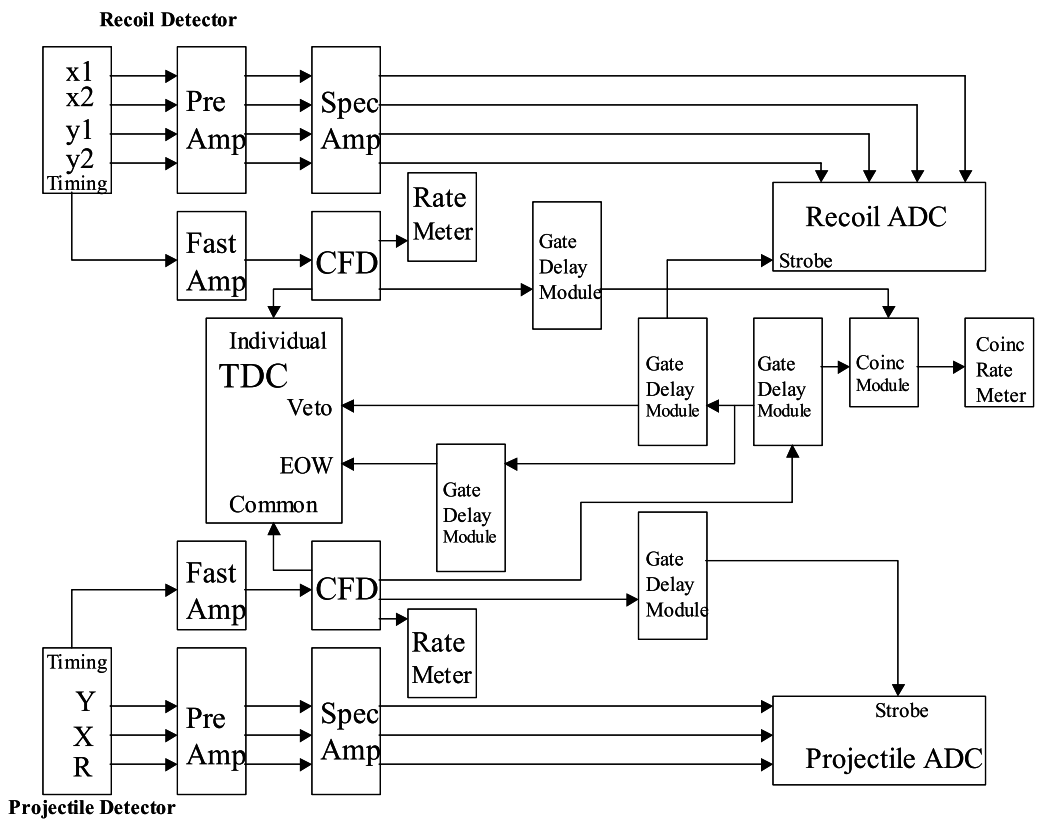

Figure 3.21: Electronic setup for coincidence detection.

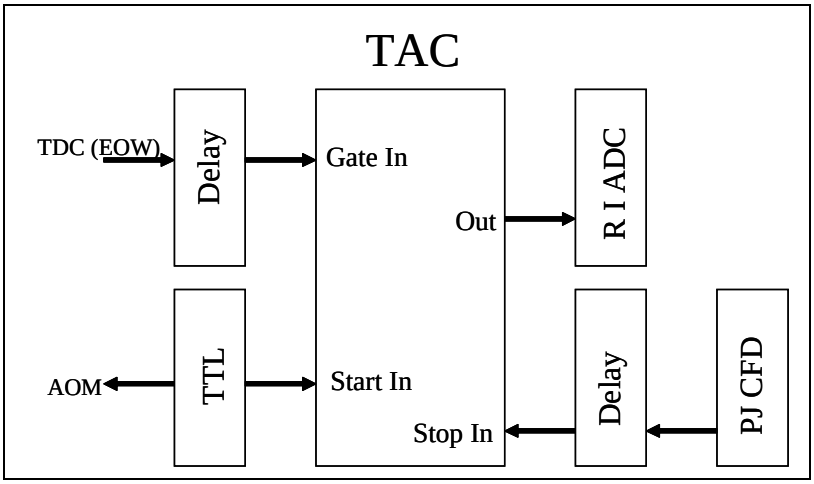

Figure 3.22: *TAC setup.*

Mass(a.u.)	**2 keV**	**5 keV**	**7 keV**
6	7.55E-05	7.80E-05	7.87E-05
23	6.88E-05	7.38E-05	7.52E-05
39	6.47E-05	7.12E-05	7.30E-05
85	5.63E-05	6.59E-05	6.84E-05
133	4.97E-05	6.17E-05	6.49E-05

Table 3.1: *Actual knob values for delay gate.*

is provided by an appropriately delayed projectile timing signal. The TDC EOW is delayed and used as a gate. The output of the TAC is sent to the recoil ion ADC to be recorded and processed by the computer. Operationally, within our electronic modules, the knob values do not exactly reflect the actual values one might wish to enter. However, these have been calibrated and recorded here in Tables 3.1 and 3.2.

Mass(a.u.)	**2 keV**	**5 keV**	**7 keV**
6	5.91E-05	6.11E-05	6.16E-05
23	5.38E-05	5.78E-05	5.88E-05
39	5.06E-05	5.57E-05	5.71E-05
85	4.40E-05	5.15E-05	5.36E-05
133	3.89E-05	4.83E-05	5.08E-05

Table 3.2: *Actual knob values for TAC delay.*

3.8.1 Recoil Ion Geometry and Reconstruction

Because the recoil ion extraction direction is not exactly parallel to the projectile axis, but at an angle of about 3.5°. However, the reconstruction of $P_{R_{\|}}$ is somewhat complicated. The additional complication is readily handled by the data acquisition program as shown in the program listing in Appendix A. The recoil ion momentum vector is determined using the following expressions:

$$P_{R_X} = b(X - X_o) \tag{3.22}$$

$$P_{R_Y} = b(Y - Y_o) \tag{3.23}$$

$$P_{R_Z} = a(T - T_o) \tag{3.24}$$

where a and b are constants, X_o and Y_o are defined as the recoil PSD center, and X and Y are the recorded recoil ion position on the PSD. T and T_o are the impact time and the "centroid" time, respectively.

Recoil Ion Vector Reconstruction

In order to reconstruct the recoil ion momentum vector and correct for the 3.5° extraction angle, the following equations are used within the acquisition program.

$$P_{R_{\parallel}} = 0.998 P_{R_Z} + 0.06 P_{R_X} \approx P_{R_Z} + 0.06 P_{R_X} \tag{3.25}$$

$$P^2_{R_{\perp}} = P^2_{R_Y} + (0.998 P_{R_X} - 0.06 P_{R_Z})^2 \approx P^2_{R_Y} + P^2_{R_X} \ , \tag{3.26}$$

where the numerical values are just the sin and cos of 3.5°.

3.9 Data Acquisition

The data acquisition and analysis were performed on the J. R. Macdonald Laboratory VAX network using the XSYS data acquisition and analysis software package [73]. Normally, the MOTRIMS experiments are done using the computer named "STARK." However, off-line sorting can be done using a different machine if desired. Details on how the data are acquired are included in Appendix A. Briefly, when a projectile triggers an event, the coincident detection scheme becomes operational. The processed signals are sent into the ADCs on the CAMAC crate and are readily read into the computer by the acquisition program which is programmed specifically to read information which is being sent to the CAMAC modules.

Chapter 4

Experimental Results

In this chapter, the experimental results and theoretical calculations for system of interest will be fully discussed. Essentially, two types of measurements were made that need to be discussed. First, we have performed relative cross section measurements of low energy alkali projectiles in collision with cooled and trapped Rb($5l$), where l = s and p. These measurements are then compared with well-established model calculations, allowing us to gain further physical insights of low energy electron transfer relative cross sections. As mentioned in section 3.5.4 , knowledge of the target excited state fraction plays a vital role in the determination of relative capture cross sections. We therefore needed a way to independently determine target excited state fractions. An elegant procedure of obtaining target excited state fraction was developed and will be presented along with the results of our cross section measurements .

4.1 Relative Cross Section Measurements

Here, relative cross section measurements for many systems of interest, differential in terms of initial states, final states, and projectile scattering angle, will be presented. Instead of presenting an atlas of all relative differential cross sections for all systems at all energies measured, the focus here is to emphasize the interesting aspects of

each system investigated. In a sense, this section gives many flavors of the limitless capabilities of MOTRIMS.

Experimental results for the case study of Na^+ + Rb($5l$) will be fully addressed. Energy dependent relative cross section measurements, differential in channel and scattering angle, along with comparison to the two center atomic orbital closed coupling calculation will be given. The 6 keV Cs^+ + Rb($5l$) collision system, with unprecedented longitudinal recoil ion momentum resolution, is used to overturn a long standing conjecture of the the origin of the oscillatory structure in total cross section measurements performed by Perel and coworkers [74]. Furthermore, energy-dependent relative cross sections for this system were measured and compared with Demkov model calculation.

Furthermore, MOTRIMS was used to investigate several collision systems having energetically degenerate charge exchange channels. Systems of interest include Rb^+, K^+, and Li^+ colliding with Rb($5l$). Kinematically complete relative cross sections were measured. Experimental results that demonstrate the capabilities of the technique to study these system will be presented. Resonant relative charge transfer cross section measurements for the case study of Rb^+ + Rb($5l$) at 7 keV were investigated. In charge transfer, the magnitude of the energy defect helps determine the electron capture probability. Typically, a small energy defect or Q value means a higher capture probability. This is well demonstrated by the enhanced capture cross sections for resonant and near resonant channels. However, present experimental evidence reveals a counterintuitive entropy-lowering example of an inelastic low energy ion atom collision. Peculiar counterintuitive relative cross sections having propensity for endoergic processes were observed. A logical explanation of the observed abnormality will be given. For the cases of K^+ and Li^+ colliding with Rb($5l$), because the target excited state fraction is not trivially obtained, a single source producing two different

types of projectiles, of which one is Na^+, is used. With the dual beam method, kinematically complete experiments for electron transfer in the collisions between K^+, and Li^+ with Rb($5l$) were possible. Details of experimental techniques and results will be presented.

4.1.1 Na^+ + Rb

Experimentally, the trapping and cooling process leaves some fraction of the rubidium in the $5p_{3/2}$ state; it is critical to determine what this fraction is. In general, studies of charge transfer from laser-excited targets are made difficult by the fact that transfer rates are proportional to the product of the cross section for transfer from some state and the population of that state. Thus, to obtain the cross section, one must have an independent measurement of the population, and *vice versa*. For example, if one wished to measure the cross section for charge transfer from a target that had been laser-excited into some state, one would first have to determine the fraction of the target in that state. The independent determination of a level's population is usually difficult and generally relies on some model-dependent measurement [75]. Thus, the uncertainties in cross section measurements tend to be rather large. In addition, if the excitation of the target is not steady-state, then the level populations are dynamic, making cross section determination problematic. Conversely, even if charge transfer cross sections are known, for example through calculation, the dynamics of the evolution of excited state fractions can be difficult to measure, since the principal means of study rely on the measurement of fluorescence, the time dependent of which is heavily affected by radiative lifetime. The Na^+ + Rb($5l$) collision system is of interest because after inspection of the energy level diagram as in Fig. 4.1, the energy defects for charge transfer from both the ground and first excited states of Rb to the various Na^+ projectile channels are well separated. This feature allows us to measure

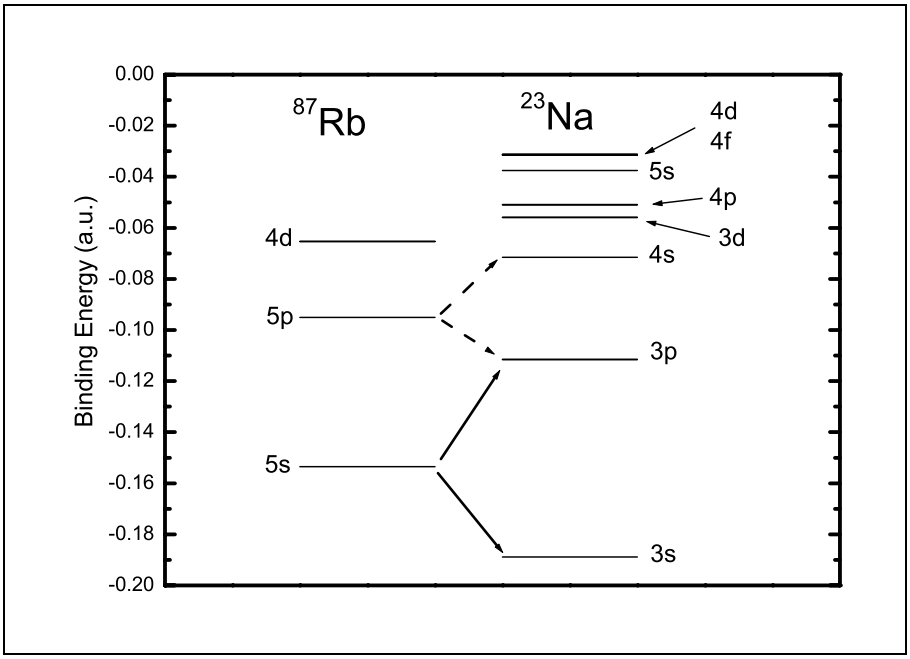

Figure 4.1: *Partial energy level diagram for sodium and rubidium [76].*

each individual peak accurately without the use of de-convolution techniques. This gives a tremendous advantage in determining target excited state fraction as will be describe here.

An Acousto-Optic Modulator (AOM) was used to chop both the trapping laser beams (trapping and repump) at 50 kHz, with an on-time duty cycle of 75%. A Time-to-Amplitude Converter (TAC) was keyed to the AOM, and the TAC output was sent to the ADC of the data acquisition system to provide a time signal, related to the laser status at the time of the collision. A plot of counts *versus* TAC output and Q-value is shown in Fig. 4.2. The figure shows capture events corresponding to the times of laser on and off. The plot in Fig. 4.3, "Laser-total" and "laser-off" Q-value spectra were made by integrating the appropriate portion of Fig. 4.2 along the vertical axis. Because the atoms do not move an appreciable distance during a single on-off period, the change in Rb(5s) population is exactly equal and opposite to the change in the Rb(5p) population. We will show that this enables one to determine both the ratio

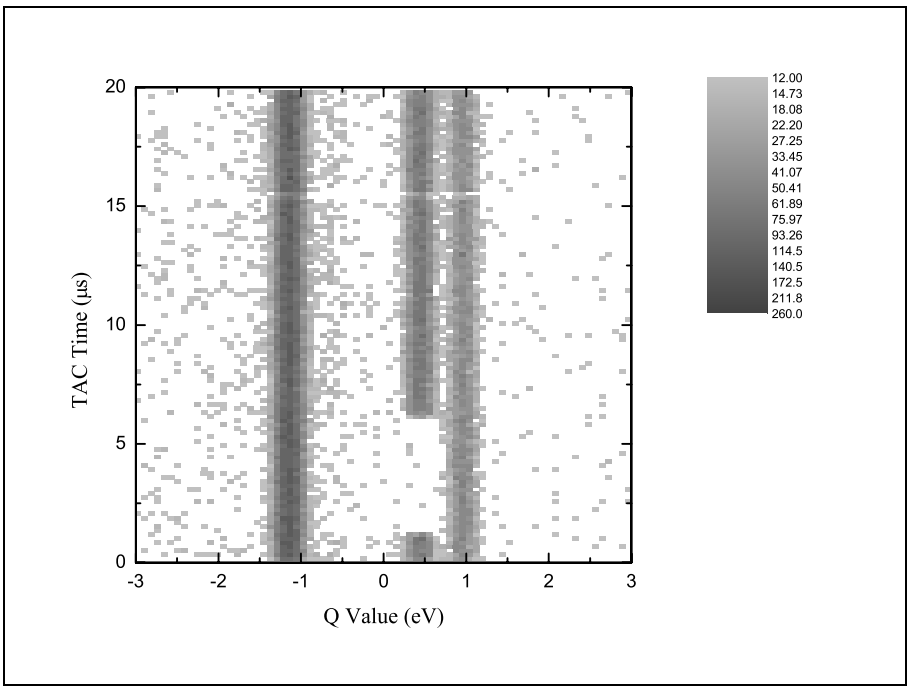

Figure 4.2: *TAC spectrum for 7 keV Na^+ + Rb(5l), where l = s and p.*

of the 5s and 5p populations and the ratio of capture cross sections from these states. Once the excited state fraction has been thus measured, an accurate measurement of the target fluorescence and spatial dimension is sufficient to determine the target density. Typically, excited state fractions of 22% were obtained. Because the day-to-day excited state fraction could vary, they were measured *in situ* for each cross section measurement presented here.

Experimental results for energy-dependent kinematically complete relative cross sections for Na^+ + Rb(5l) are presented in Tables 4.1 and 4.2. In Table 4.1, cross sections of capture from the ground state into various final states are normalized to the total capture from the ground state. As observed here, capture from the ground state Rb(5s) to the final state Na(3p) over our range of energies is the dominant channel. Little of the 5s goes into the Na(3d) final state. Table 4.2 shows the relative capture cross sections from an excited Rb(5p) target to various final projectile states.

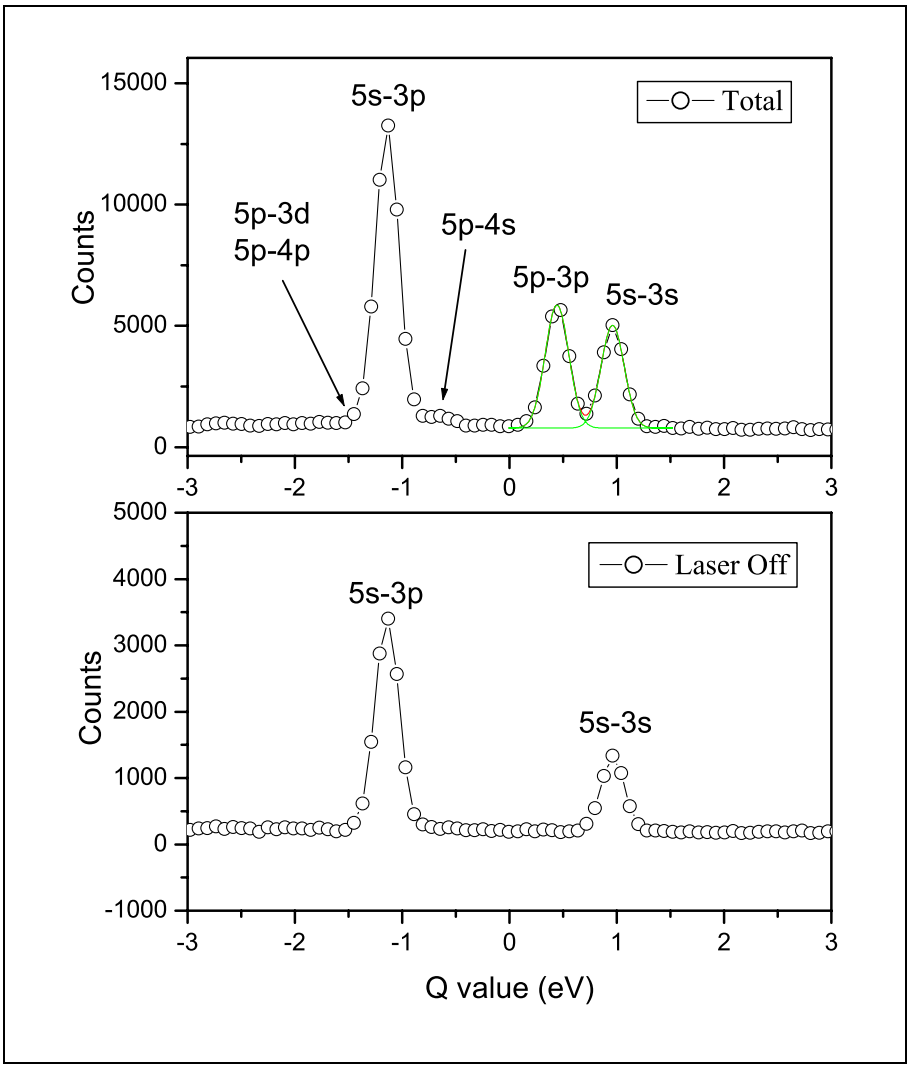

Figure 4.3: *Q value spectra for 7 keV Na^+ + Rb(5l), where l = s and p. Down projections of Fig. 4.2. The top panel is the total projection and the lower panel is the projection of the regions where the lasers are off.*

Final States	2 keV	5 keV	7 keV
3s	0.02 ± 0.01	0.19 ± 0.07	0.19 ± 0.01
3p	0.98 ± 0.05	0.79 ± 0.29	0.78 ± 0.01
3d	0.00 ± 0.02	0.02 ± 0.01	0.03 ± 0.01

Table 4.1: *State selective energy dependent relative cross section experimental results for the Na^+ + Rb(5s) collision system. Here the relative cross sections for each channel are normalized to the ground state 5s total cross section.*

The dominant channel here is the Rb(5p)-Na(3p) channel. The relative total cross sections of ground to first excited state are presented in Table 4.3.

The experimental results reported in Tables 4.1, 4.2 and 4.3 are used as tests of theoretical calculations [43]. Theoretically, the Rb and Na are each treated as one-electron systems with the core "frozen". The active electron in each atom is governed by model potentials:

$$V_{Na}(r) = -\frac{1}{r}(1 + (10 + 17.9635r)e^{-3.5927r}) \tag{4.1}$$

$$V_{Rb}(r) = -\frac{1}{r}(1 + (36 - 1.975r)e^{-2.34113r}) \ . \tag{4.2}$$

Tables 4.4 and 4.5 show the energies of the bound and pseudo-continuum states of Na and Rb, respectively, used in the close-coupling calculation [43]. For the bound states, the binding energies obtained from the model potentials were also compared to experimental values [76]. The pseudo-states were used in the basis set to help describe the distortion of the electronic orbitals at smaller internuclear separations. To obtain the differential cross sections, the eikonal approximation was employed [39].

Final States	**2 keV**	**5 keV**	**7 keV**
3p	0.60 ± 0.14	0.82 ± 0.05	0.78 ± 0.02
4s	0.08 ± 0.03	0.08 ± 0.01	0.07 ± 0.01
3d	0.15 ± 0.16	0.03 ± 0.02	0.11 ± 0.02
4p	0.14 ± 0.15	0.04 ± 0.02	0.03 ± 0.01
5s	0.01 ± 0.01	0.00 ± 0.01	0.00 ± 0.01
4d	0.02 ± 0.01	0.03 ± 0.01	0.01 ± 0.01

Table 4.2: *Same as in table 4.1. However, the initial state is Rb(5p) and the relative cross sections are normalized to the Rb(5p) total cross section.*

Relative Cross Sections	**2 keV**	**5 keV**	**7 keV**
$\frac{\sigma_p}{\sigma_s}$	1.60 ± 0.80	3.70 ± 0.31	2.75 ± 0.01

Table 4.3: *Energy dependent relative total cross sections ($\frac{\sigma_p}{\sigma_s}$) for the Na^+ + Rb(5l), where l = s and p, collision system.*

State	Theory	Experiment
3s	-0.18852	-0.18886
4s	-0.07185	-0.07158
5s	-0.03748	-0.03758
6s	-0.01849	-0.02313
7s	0.09104	-0.01566
8s	0.53203	-0.01131
9s	2.41623	-0.00854
3p	-0.11145	-0.11154
4p	-0.05098	-0.05094
5p	-0.02902	-0.02920
6p	-0.00719	-0.01892
7p	0.10224	-0.01325
8p	0.70719	-0.00980
9p	2.19506	
3d	-0.05563	-0.05594
4d	-0.03126	-0.03144
5d	-0.01984	-0.02011
6d	0.00892	

Table 4.4: *This table is from Ref. [43]. Bound state energies of Na obtained from the model potential and the comparison with experimental data [76]. Even-tempered basis functions are used to diagonalize the atomic Hamiltonian. Energies are in atomic units.*

State	Theory	Experiment
5s	-0.15071	-0.15351
6s	-0.06215	-0.06177
7s	-0.03320	-0.03362
8s	-0.01959	-0.02116
9s	-0.01227	-0.01454
10s	-0.00828	-0.01061
11s	-0.00530	-0.00808
12s	-0.00306	
13s	-0.00162	
14s	0.30795	
15s	1.81277	
5p	-0.10272	-0.09541
6p	-0.04800	-0.04520
7p	-0.02770	-0.02657
8p	-0.01713	-0.01752
9p	-0.01024	-0.01242
10p	-0.00579	
11p	-0.00305	
12p	0.04485	
13p	0.66372	
5d	-0.03360	-0.03640
6d	-0.02111	-0.02279

Table 4.5: *This table is from Ref. [43]. Bound state energies of Rb obtained from the model potential and the comparison with experimental data [76]. Even-tempered basis functions are used to diagonalize the atomic Hamiltonian. Energies are in atomic units.*

Final State	2 keV	5 keV	7 keV
Na(3s)	1.06	6.02	8.41
Na(3p)	19.16	20.59	22.35
Theory	0.055	0.292	0.376
MOTRIMS	0.021±0.001	0.241±0.012	0.244±0.015

Table 4.6: *Theoretical integral cross sections (10^{-16} cm^2) for charge transfer from ground state Rb(5s) to final states [43]. The third and fourth lines show the comparison between theory and experiment for the capture cross section ratio: Na(3s)/Na(3p).*

Discussion of Na^+ + Rb(5s) Results

For collision energies of 2, 5 and 7 keV, the two dominant charge-transfer channels in Na^+ + Rb(5s) collisions are transfer into Na(3s) and Na(3p) states. Table 4.1, shows that in this energy range, capture to Na(3p) dominates over Na(3s). All the other channels are much weaker and are not observed in the experiment. Comparison with calculated cross sections is presented in Table 4.6. The fact that these are the two dominant channels can be understood from the degree of inelasticity for each transition. For Rb(5s) → Na(3s), the transition is an exoergic process with a Q-value of +0.0354 a.u., whereas for Rb(5s) → Na(3p), the process is endoergic, with Q = –0.0419 a.u. From the asymptotic energy levels, it would appear that the dominant transition would be to the Na(3s) state. This is not what is observed experimentally, or from the theoretical calculations.

A proper framework to understand the experimental results is best based on the molecular potential curves [43]. In the AOCC calculations, such curves are not calculated. Based on the model potentials as in Eqs. 4.1 and 4.2, the adiabatic potential

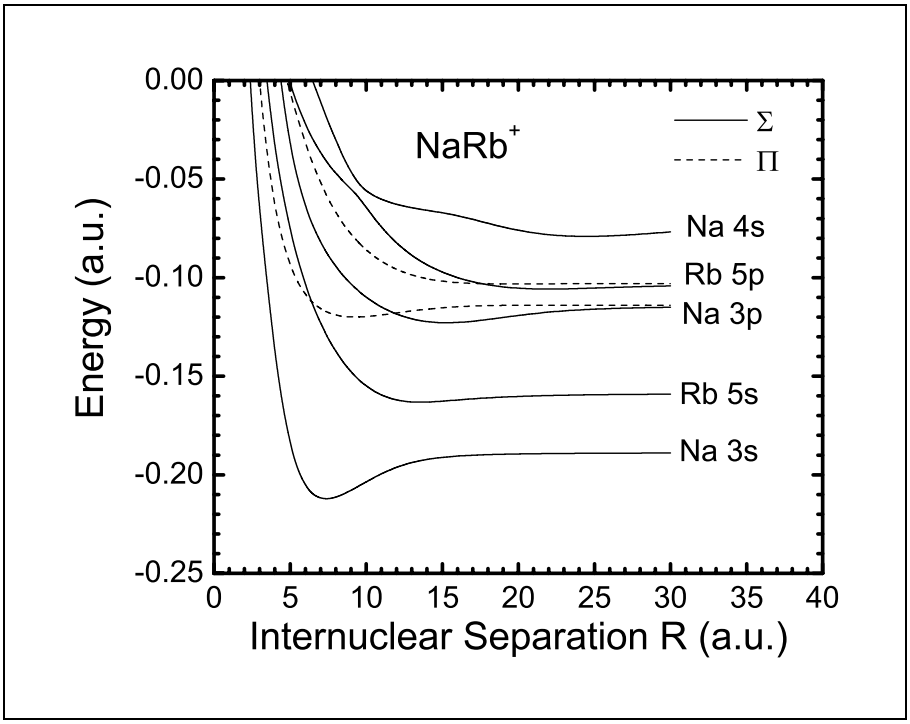

Figure 4.4: *The adiabatic potential curves for the NaRb$^+$ molecule. This figure is from Ref. [43].*

curves of NaRb$^+$ were calculated, and the results are shown in Fig. 4.4.

In fact, these curves are very similar to those calculated by Melius and Goddard *et al* [77] for the Li$^+$ + Na system. From these curves, it is clear that transition to Na(3s) from Rb(5s) is dictated by the radial coupling between the two Σ states, which show an avoided crossing at R near 13 a.u.. For the transition to Na(3p), there are two possibilities. A radial coupling between two Σ curves would populate the Na(3p$_0$) final state, while a rotational coupling between Σ and Π states would populate the NA(3p$_1$) final state. For the latter, the two curves cross at R about 6 a.u., and this crossing is an efficient mechanism for populating the Na(3p) state at low energies.

The differential cross sections for the two dominant channels are shown in Fig. 4.5. In order to compare MOTRIMS measurements with theoretical calculations, the theoretical results were convoluted with the experimental angular resolution of 73.64,

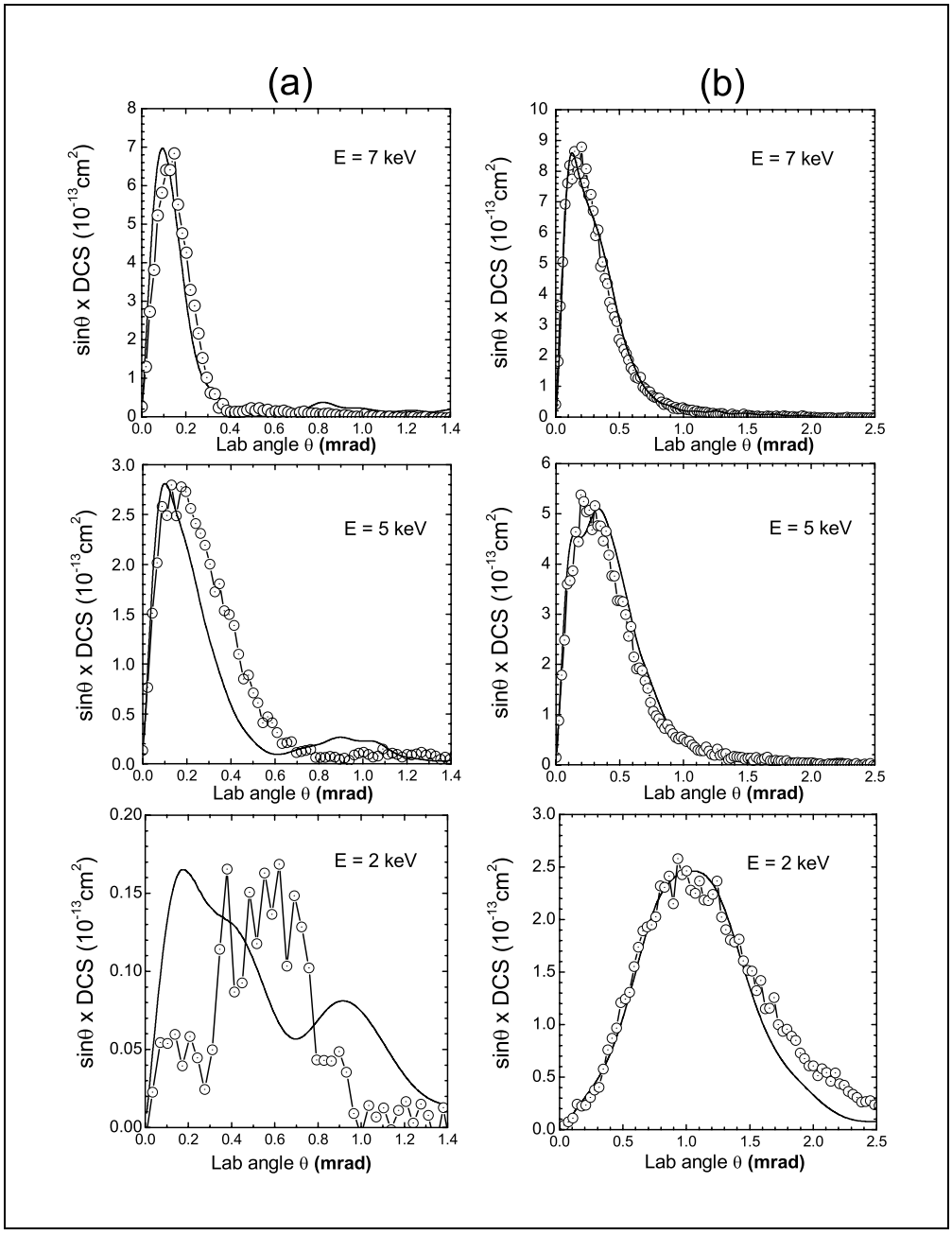

Figure 4.5: *(a) sinθ × DCS as functions of laboratory scattering angle θ for Rb(5s)→Na(3s) at impact energies from 7 to 2 keV. The ⊙ represent the MOTRIMS data and the solid line,—, denotes theoretical calculations folded with experimental angular resolution. The experiment results have been normalized to the theoretical data. (b) is the same as (a) except for the Rb(5s)→Na(3p) channel. Note the difference in the angular scale.*

87.2 and 138.0 μradians for 7, 5 and 2 keV, respectively. The experimental results were normalized to the theoretical predictions at the peak for easy comparison.

From Fig. 4.5(b), it is clear that there is an excellent agreement between experiment and theory for the dominant Rb(5s)→Na(3p) channel. For the weaker Na(3s) channel, shown in Fig. 4.5(b), the agreement is quite good at 7 keV, but significant deviations can be seen at 2 keV. At this energy the total cross section to NA(3s) is only about 5% of the capture to Na(3p). The smaller cross section is reflected by the larger errors in the DCS, both in experiment and theoretical model.

Another observation is that the differential cross section for capture to Na(3s) peaks at smaller angles, reflecting the fact that capture occurs at larger impact parameters. In contrast, capture to Na(3p) occurs at larger scattering angles, reflecting the efficient rotational coupling at internuclear distance at about 6 a.u..

The differential cross sections in Fig. 4.5 for different energies can all be put on the same graph if one were to plot the differential cross section against E$\times\theta$. Fig. 4.6(a) shows the experimental data for capture to the dominant Na(3p) channel. In Fig. 4.6(b) the theoretical calculations for the same system, this time without convolution are shown. It is clearly seen that the predicted differential cross sections show many oscillations with respect to the scattering angle. Such oscillations are expected for collisions at low energies. Unfortunately, limitations in the angular resolution from the current MOTRIMS apparatus makes the observation of such oscillations impossible. However, the trend here is that, for decreasing in energy, the position of the experimental peaks moves away from the origin and theoretical curves show similar trend.

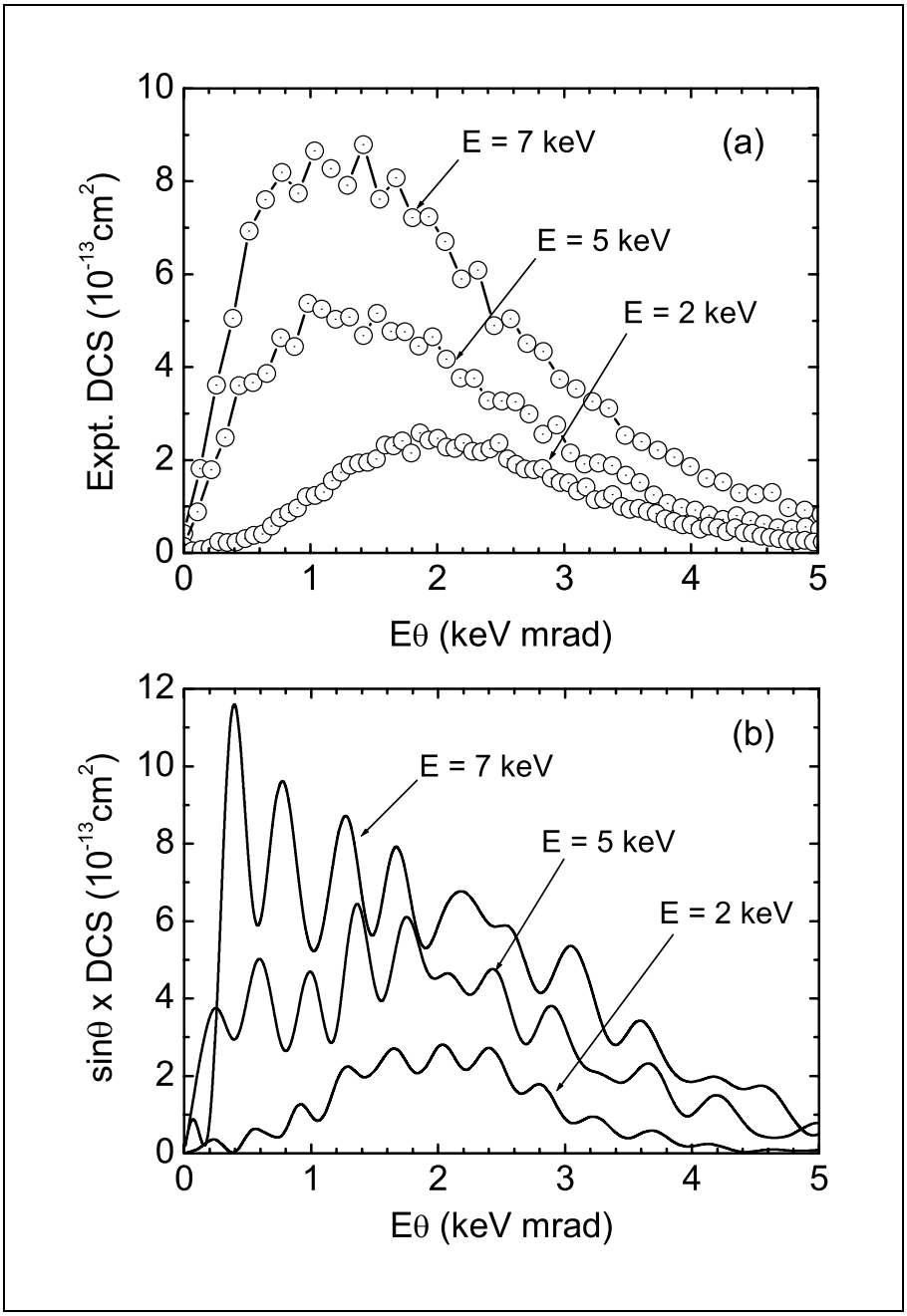

Figure 4.6: *(a) Experimental measured DCS as functions of scaled laboratory scattering angle $E \times \theta$ for Rb(5s)→Na(3p) at impact energies from 7 to 2 keV. Experimental data are normalized to the TCAOCC calculations. (b) is the same as (a) except that this is the results from TCAOCC calculations [43].*

Final State	2 keV	5 keV	7 keV
Na(4s)	10.39	5.03	8.92
Na(3p)	94.20	132.82	129.10
Theory	0.110	0.038	0.069
MOTRIMS	0.133±0.021	0.098±0.009	0.090±0.011

Table 4.7: *Theoretical integral cross sections (10^{-16} cm^2) for charge transfer from Rb(5p) to the indicated final states [43]. The third and fourth lines show the comparisons between theory and experiment for the capture cross section ratio: Na(4s)/Na(3p).*

Discussion of Na^+ + Rb(5p) Results

For collisions of Na^+ with the excited Rb(5p) states at energies of 2, 5, and 7 keV, the dominant processes are electron capture to the Na(3p) and Na(4s) states. This can be anticipated from the energy level diagram, Fig. 4.1, as well as from the potential curves in Fig. 4.4. Table 4.7 shows the experimental cross section ratios for Na(4s) with respect to Na(3p), and compares the results with theoretical calculations. The agreement is quite good except at 5 keV where the calculated result is outside the measured uncertainty.

In terms of the potential curves of Fig. 4.4, the mechanism for electron transfer from Rb(5p)to Na(3p) and Na(4s) can be anticipated. Radial coupling will take an electron from initial Rb($5p_0$) to final Na($3p_0$), and the rotational coupling will take it to Na($3p_1$). The rotational coupling is weak because there is no curve crossing. Thus the radial coupling, which has a slight avoided crossing at large R near 22 a.u., is expected to be the dominant one. Similarly, radial coupling will take electron

from initial Rb($5p_1$) to Na($3p_1$), and the rotational coupling will take it to Na($3p_0$). Again, the radial coupling is expected to dominate, and there is a weak avoided crossing between the two Π curves at R near 15 a.u.. Thus, we expect the transition to Na(3p) to be quite large and to occur at large impact parameters. For transition to Na(4s), the energy gap at large R is larger, therefore transitions at larger impact parameters would be smaller, especially when the collision energy is decreased. At the lower energies, the avoided crossing between the two Σ curves at R near 9 a.u. should be more efficient in populating the Na(4s) state.

In Fig. 4.7, the measured differential cross sections are compared with the convoluted theoretical differential cross sections. For Rb(5p) to Na(3p) channel, the experimental measurement agrees perfectly with the theoretical differential cross section at 7 keV. At 5 keV there is only a small trace of discrepancy. At 2 keV, the experimental differential cross section at larger angles are greater than the theory predicts. For the weak channel (i.e., Rb(5p) to Na(4s)), the overall agreement is less satisfactory. At 7 keV, the agreement at small angles is quite good, but the theory shows a shoulder at larger angle. At 5 keV, the agreement between theory and experiment is only fair, and it appears that the shoulder at 7 keV becomes a pronounced peak at 5 keV. At 2 keV, the experimental signal is too weak to extract useful information, but the shoulder from theory at 7 keV appears to become the major peak. This structure is due to the avoided crossing of the two Σ curves. At 7 keV, the transition is dominated by the coupling at large R, thus the differential cross section is rather forward peaked. As the energy is decreased, the system evolves more adiabatically and probabilities for transitions at large R decrease. At 2 keV, transitions at large R become insignificant, and the major mechanism for transition occurs at the avoided crossing near R=9 a.u.. The mechanism also explains the minimum of the total cross section to Na(4s) at 5 keV. Above this energy, transitions occur mostly at large impact parameters. Below

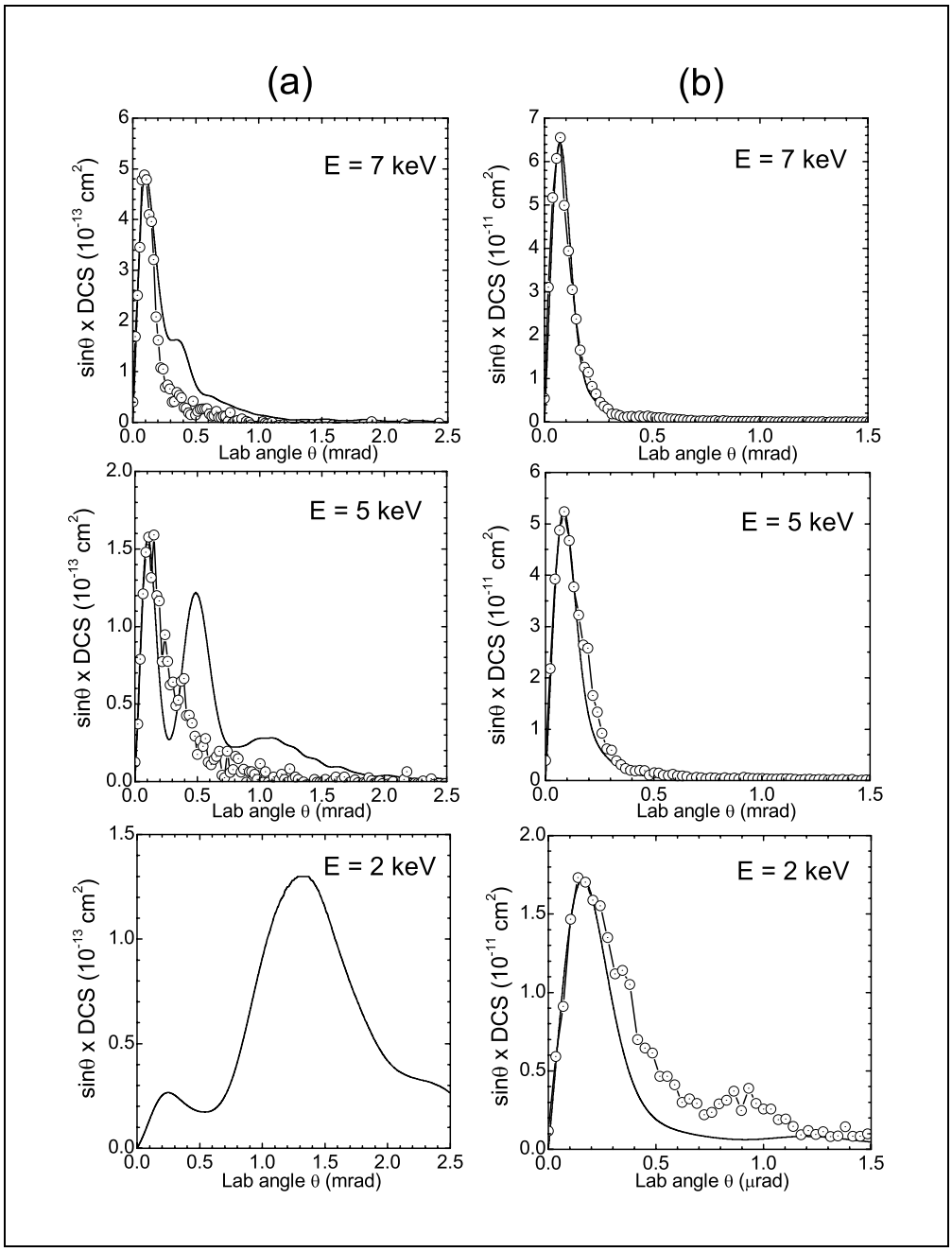

Figure 4.7: *(a) Same as Fig. 4.5 but for charge-transfer from Rb(5p) to Na(4s). Solid lines denote the TC-AOCC and circles represent the experiment data. (b) is the same as (a) except for the Rb(5p)→Na(3p) channel.*

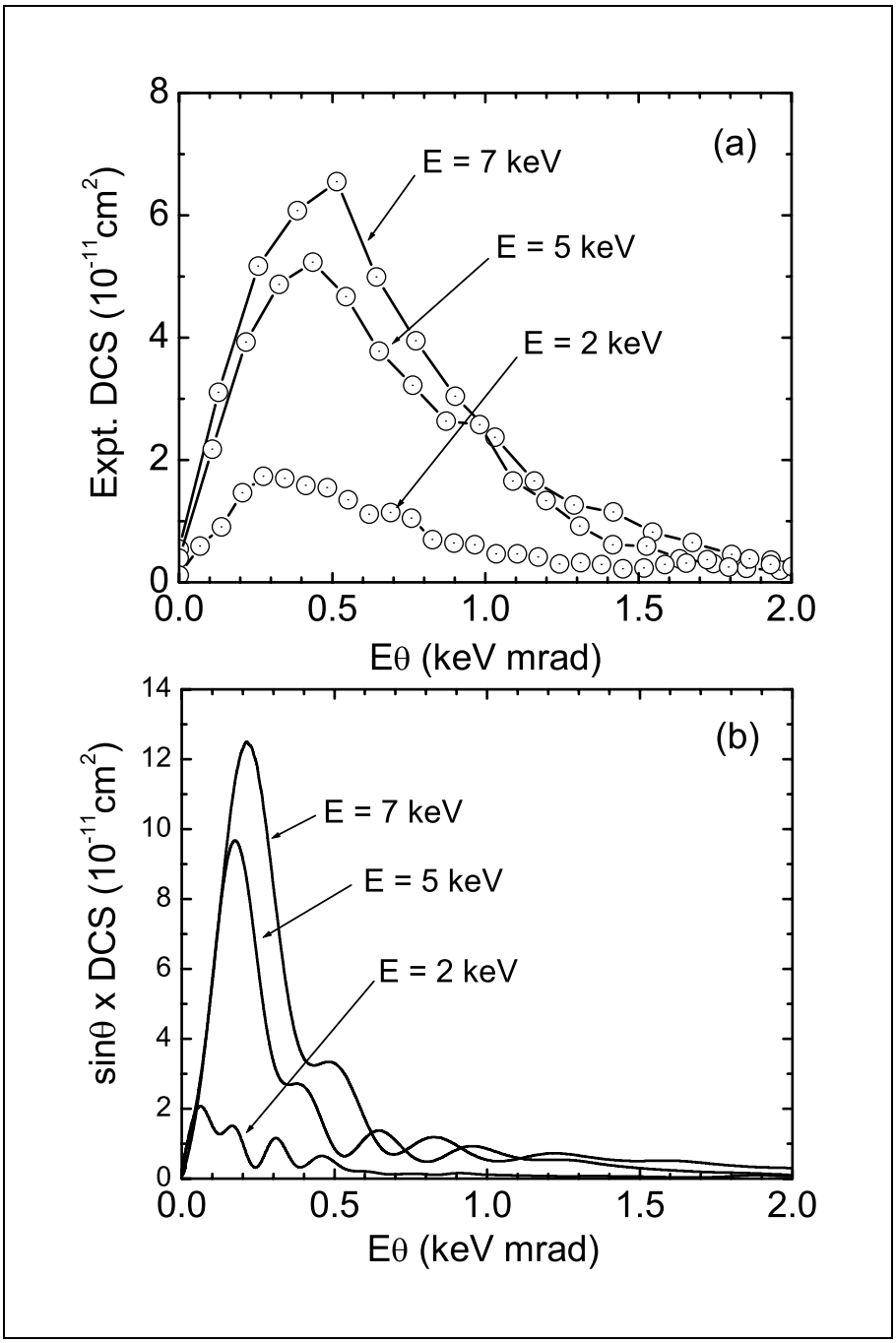

Figure 4.8: *Same as Fig. 4.6 but for charge-transfer from Rb(5p) to Na(3p).*

this energy, the Landau-Zener type transition at R near 9 a.u. becomes more efficient such that the cross section increases with decreasing collision velocity.

In Fig. 4.8, the differential cross sections *versus* E$\times\theta$ for the three collision energies for the Rb(5p) to Na(3p) transition are compared. The experimental results are shown in the top panel. The theoretical results, without the convolution with angular resolution are shown in the bottom panel. The calculated angular distributions are peaked much more in the forward angles than the experimental measurements. The experimental results do not show the predicted rapid oscillations in differential cross sections and the propensity for forward peaking. However, the trend here is that, for decreasing in energy, the position of the experimental peaks moves towards the origin. Theoretical curves show similar trend.

4.1.2 Cs^+ + Rb

Kinematically complete charge exchange for Cs^+ + Rb(l) system is examined with unprecedented longitudinal recoil ion momentum resolution. For 6 keV Cs^+ + Rb($5l$), where l = s and p, initial and final state selective charge exchange cross sections are obtained. For each charge transfer channel, cross sections, differential in scattering angle, are measured. These data are then used to overturn previous long-standing conjecture as to the origin of oscillations seen in total charge exchange cross section measurements, and compare well with an enhanced Demkov model calculation. Furthermore, various energies of Cesium projectile are used to study energy dependent kinematically complete relative charge transfer cross sections.

In Fig. 4.9, the relevant channels for charge exchange from a trapped rubidium target to cesium projectiles can be seen. Figure 4.10 shows relative cross sections, differential in Q value and scattering angle for 6 keV Cs^+ + Rb($5l$). Integration along the vertical axis yields the Q-value spectrum of Fig. 4.11. Setting gates around the

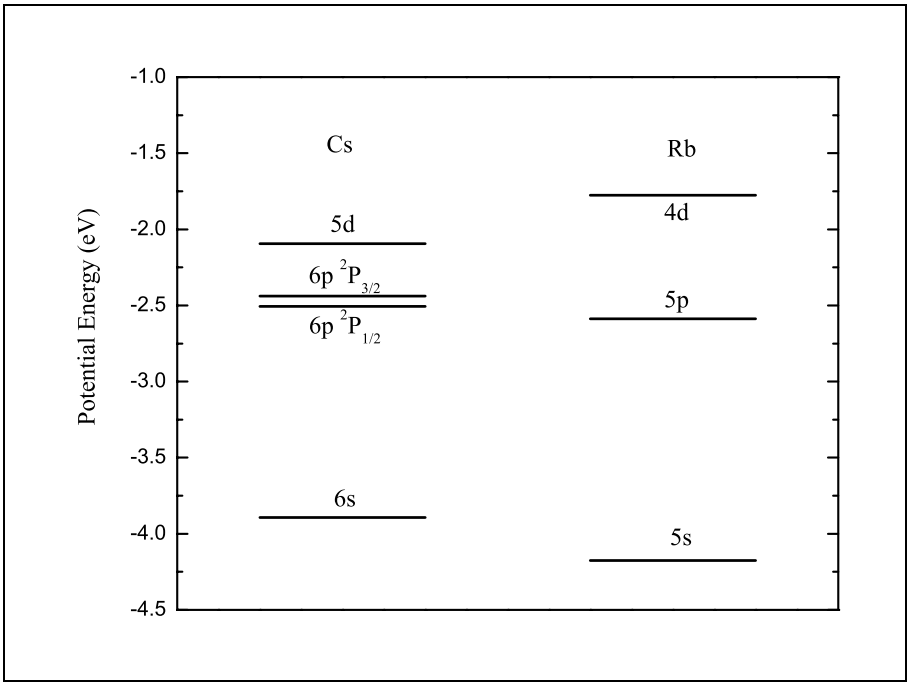

Figure 4.9: *Partial energy level diagram for cesium and rubidium [76].*

appropriate channels in Fig. 4.10, and integrating along the horizontal axis yields the scattering angle results for those channels as shown in Fig. 4.12.

Figure 4.12 shows the charge transfer cross sections, differential in scattering angle, for the two major peaks of Fig. 4.11. The resolution in scattering angle, essentially limited by the resolution of the position sensitive detector, is about 30 microradians. Structure is clearly seen in the Rb(5s)-Cs(6s) case and, to a lesser extent, in the Rb(5p)-Cs(6p) case as well. For both of these channels, oscillations arise from the Hankel transform [6] of the impact parameter dependent scattering amplitude. In the "s-s" channel, $m_i = m_f = 0$ which means exactly one term (and therefore one phase) exists in the transform. However, in the "p-p" channel, $m_i = 0, \pm 1$ and $m_f = 0, \pm 1$. Therefore, the different phases of each of these terms may cause some of the structure to be washed out. Here, m_i and m_f refer to the initial and final magnetic quantum numbers, respectively. For the other transitions, better statistics may reveal

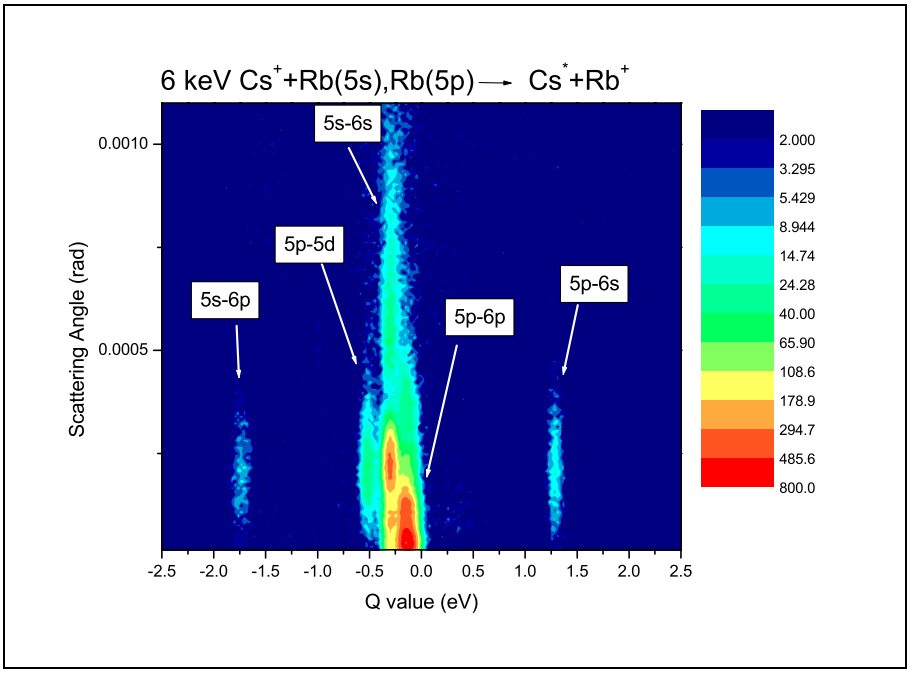

Figure 4.10: *Double Differential Cross Sections for 6 keV Cs^+ + Rb(5l), where l = s and p.*

some structure, but at a greatly reduced level as compared to the Rb(5s)-Cs(6s) and Rb(5p)-Cs(6p) cases. These cross sections are essentially quadruply differential (scattering angle, initial state, final state, and collision energy) and therefore serve as extremely severe tests of theory.

In the late 1960's Perel and coworkers, using then state-of-the-art techniques, were able to detect distinct oscillations in the total charge transfer cross sections as a function of collision energy in alkali ion-alkali atom systems [74]. It was conjectured at that time that the oscillations were caused by the projectile ion polarizing the target atom, thereby putting it into a superposition of s and p states. The ensuing charge transfer process could then follow along two distinct paths, resulting in the observed interference pattern as seen in Fig. 4.13. Theoretical treatments of the collision [41, 78] neither confirmed nor disputed these conclusions, and the hypothesis has remained unchallenged for roughly thirty-five years, at least partly because no experimental

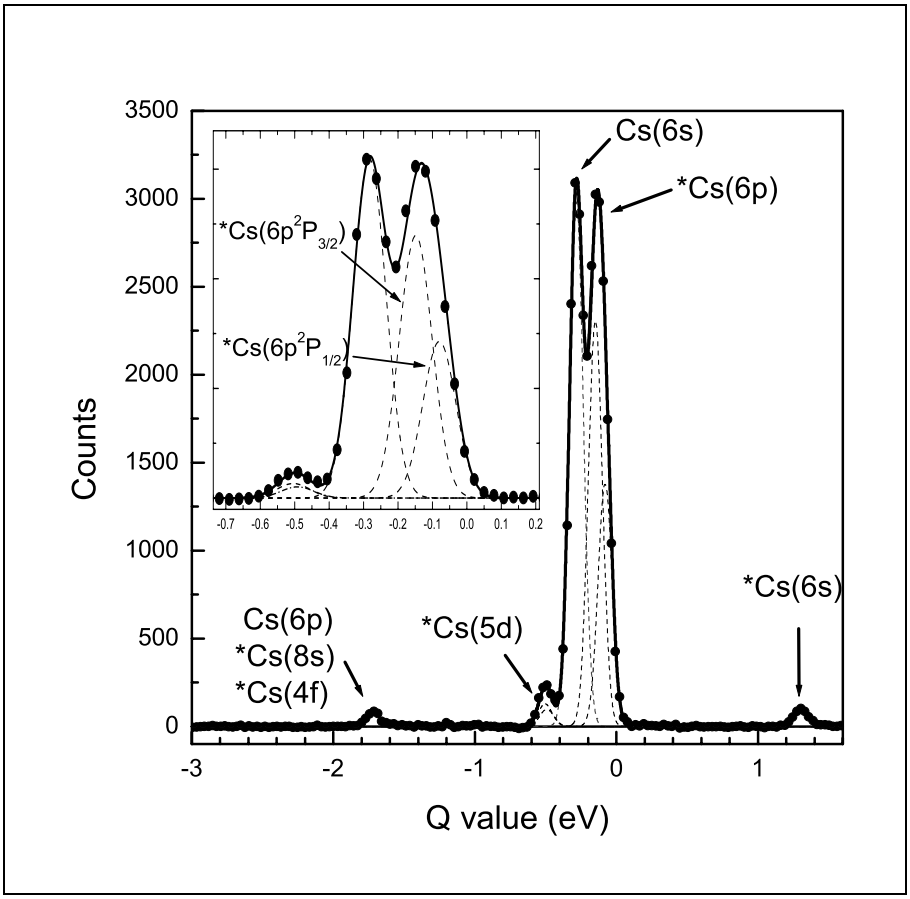

Figure 4.11: *Q-value spectrum for 6 keV Cs^+ + Rb(5l), where l = s and p. The labels identify the final state in cesium; "*" on the labels indicate charge exchange from Rb(5p). The solid points are data; the inset shows the theoretical predictions of individual channel cross sections (dashed lines) and the sum of all the channels (solid line).*

method existed which could test it.

The Q-value results of these experiments show conclusively that the structure observed by Perel [74] can not possibly be due to polarization effects in the incoming channel causing interferences. The evidence is two-fold: First, the laser-excited rubidium lines in Fig. 4.11 shows that Rb(5p) state transfers predominantly to Cs(6p), with some small fraction going to Cs(5d), and an even smaller fraction going to Cs(6s). Second, "direct" charge exchange from Rb(5s) would have precisely the same

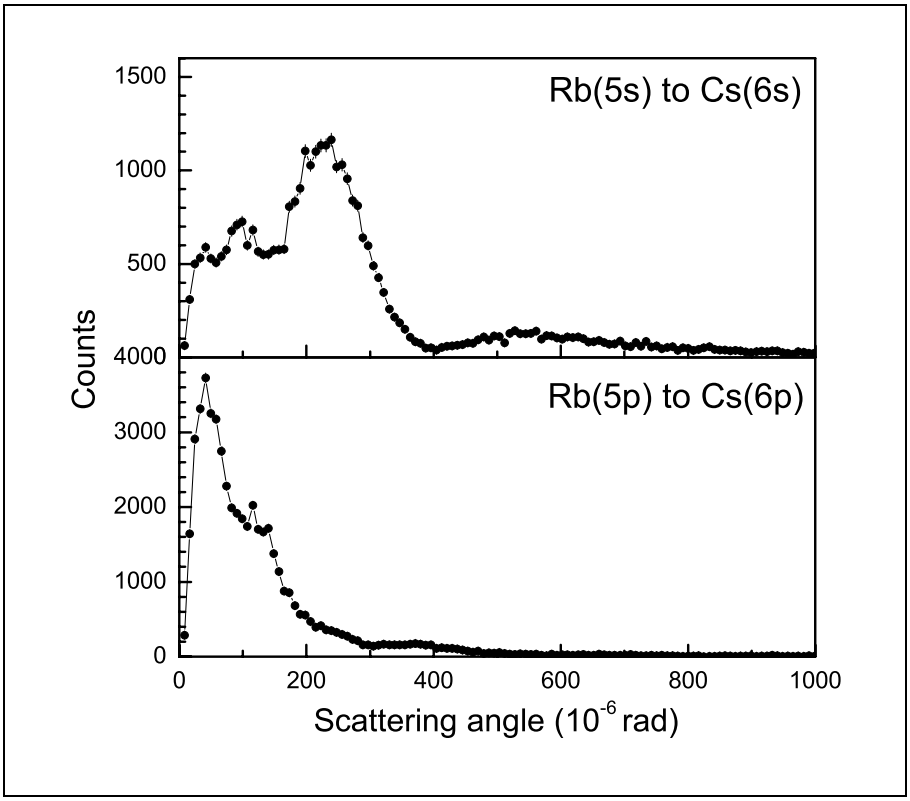

Figure 4.12: *Counts versus scattering angle for the two dominant channels shown in Fig. 4.11. The resolution is approximately 30 microradians (4 points) and the error bars are statistical.*

Q-value as "polarization" charge exchange (the mechanism proposed by Perel *et al.*). Therefore, if Perel's hypothesis were correct, Fig. 4.11 should shows a large peak at a Q-value corresponding to Rb(5s) to Cs(6p), whereas the actual peak at that Q-value is extremely small. Furthermore, the amplitude of the relatively small Rb(5p) to Cs(6s) peak represents an upper limit to the contribution of "polarization" charge exchange to the large Rb(5s)-Cs(6s) peak. This upper limit does not seem large enough to produce the interference structure seen in Perel's measurements. Thus, a different mechanism must be responsible for the oscillations reported by Perel.

In order to theoretically compare the cross sections for the different charge exchange channels with each other, the explicit impact-parameter dependence of the

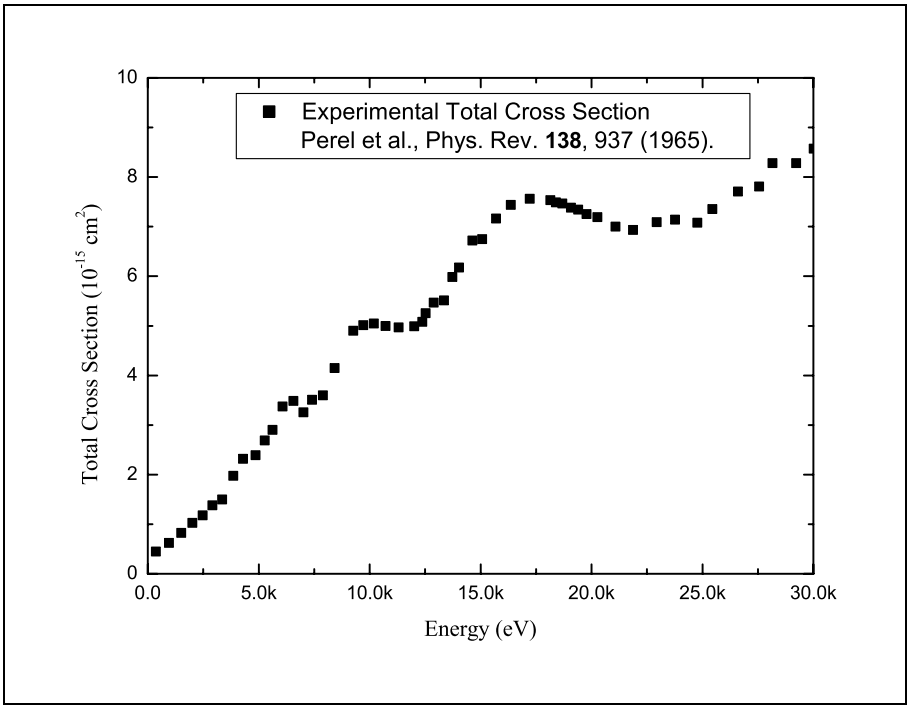

Figure 4.13: *Perel's measured cross sections for Cs^+ + Rb(5s) [74].*

transition probability was derived within the Demkov model [41]. The cross sections for the reaction channels are then evaluated by integration over impact parameter, and compared to the data after folding in the experimental resolution of 96 meV.

Shown in the inset of Fig. 4.11 are the theoretical predictions of individual channel cross sections (dashed lines) and the sum of all the channels (solid line). Two parameters were used to fit the results of this model calculation to experiment. These are an overall multiplicative constant (only relative cross sections were measured) and target excitation fraction. From the fit, an excitation fraction of 15% was determined. This is well within the uncertainty of an independent measurement of excited state fraction of 16±7%. The modified Demkov model greatly underestimated the size of the Rb(5p)-Cs(6s) channel. This is expected since the model is valid only for $H_{12} \gg \Delta$. While this approximation is valid for channels having a Q-value $< \pm$ 0.8 eV, it evidently fails for the larger Q-values.

Energy (keV)	**Rb(5s)-Cs(6s)**	**Rb(5s)-Cs(6p)**
3.2	0.97 ± 0.04	0.03 ± 0.01
4.3	0.97 ± 0.03	0.03 ± 0.01
4.6	0.97 ± 0.03	0.03 ± 0.01
5.5	0.96 ± 0.03	0.04 ± 0.01
6.0	0.97 ± 0.08	0.03 ± 0.01
6.4	0.97 ± 0.02	0.03 ± 0.01

Table 4.8: *Experimental state selective energy dependent relative cross sections for the Cs^+ + Rb(5s) collision system. Here the relative cross sections for each channel are normalized to the ground state Rb(5s) total cross section.*

Various energies of cesium projectiles were used to study energy dependent relative cross sections. Relative capture cross sections of each capture channel from Rb(5s) with respect to total capture from ground state Rb(5s) are given in Table 4.8. The dominant electron capture channel is Rb(5s)-Cs(6s) for the range of energy investigated here. The remaining contribution to the total capture from ground state is the Rb(5s)-Cs(6p) channel. Table 4.9 shows the relative capture from the first excited Rb(5p) state to various final states. The dominant channel is the Rb(5p)-Cs(6p) channel. Energy dependent relative total cross sections are presented in Table 4.10.

Experimental data, differential in Q-value are used to test theoretical models. The solid line shown in Fig. 4.14 is an interpolation of calculated ratio of cross sections for the dominant electron capture channels Rb(5p)-Cs(6p) and Rb(5s)-Cs(6s). The inset is the actual output of the calculation. The experimental relative cross sections for these two dominant channels are also shown. Agreement in the general trend is

Energy (keV)	**Cs(6s)**	**Cs(5d)**	**Cs(7s)**	**Cs(6p)**
3.2	0.03 ± 0.01	0.06 ± 0.01	0	0.91 ± 0.03
4.3	0.02 ± 0.01	0.06 ± 0.01	0.01 ± 0.01	0.92 ± 0.02
4.6	0.03 ± 0.01	0.06 ± 0.01	0.01 ± 0.01	0.90 ± 0.02
5.5	0.03 ± 0.01	0.10 ± 0.01	0	0.87 ± 0.04
6.0	0.02 ± 0.01	0.03 ± 0.02	0	0.95 ± 0.07
6.4	0.03 ± 0.01	0.01 ± 0.07	0	0.90 ± 0.02

Table 4.9: *Experimental state selective energy dependent relative cross sections for the Cs^+ + Rb(5p) collision system. Here the relative cross sections for each channel are normalized to the excited state Rb(5p) total cross section.*

Energy (keV)	$\frac{\sigma_p}{\sigma_s}$
3.2	10.77 ± 3.31
4.3	7.75 ± 1.79
4.6	9.64 ± 1.21
5.5	6.65 ± 0.68
6.0	6.33 ± 0.51*
6.4	4.93 ± 0.53

Table 4.10: *Energy dependent relative total cross section for Cs^+ + Rb(5l) where l = s and p. * indicates excited state fraction was obtained by observing target fluorescence.*

seen through a general decrease in relative cross sections as energy decreases.

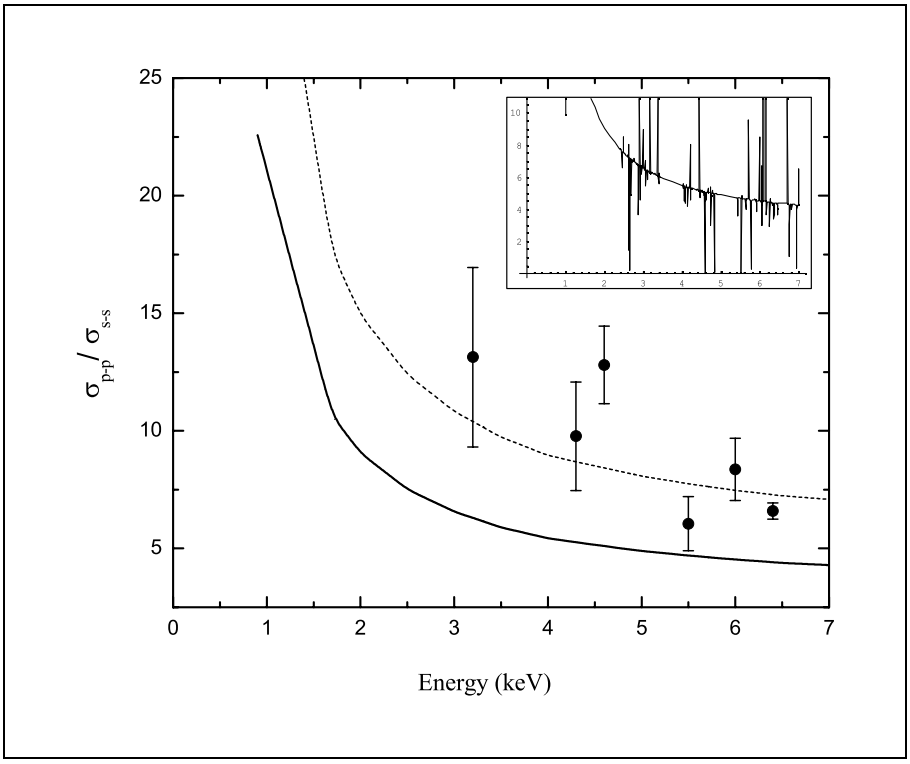

Figure 4.14: *Experimental energy-dependent relative cross sections compared to modified Demkov model. Solid line is the theoretical calculation while the dash line is the solid line × 1.65.*

4.1.3 Rb^+ + Rb

In the early 1960's, Everhart and collaborators investigated resonant charge transfer collisions [79] including He^+ + He and Ne^+ + Ne. Measurements of electron transfer probabilities, differential in scattering angle, were made over a wide range of incident energy. However, collisions with excited targets were not examined due to technical difficulties at the time of the experiments. For alkali systems, Perel *et al.* performed a series of experiments investigating total cross sections [74]. Theoretical and experimental studies for resonant charge transfer cross sections have continued to be investigated. Olson addressed the resonant transfer Rb^+ + Rb theoretically [80].

Meanwhile, Schmidt and co-workers studied resonant charge transfer in low energy collisions of Na^+ with laser excited $Na^*(3p)$ [81]. Relative differential scattering cross sections for charge transfer were measured over a range of collision energies. Uncertainty in measurement of target excited state fraction contributed to an overall large uncertainty in measurement of relative cross sections. Therefore, the theoretical comparisons were only made with the measured ground state cross sections.

Collisions of protons and alkali ions with Na targets have been investigated extensively by Nils Andersen and coworkers in the 1990's [82]. However, for these systems, it is unclear as to how energetically degenerate electron capture channels can be resolved even for the apparatus having the best resolution. How to determine the target excited state fractions was a question which also remained. The setup presented in this dissertation allows a unique probe of target excited state fraction as well as the determination of state-selective charge transfer differential cross section for systems having energetically degenerate channels. Experimental results are shown here to further demonstrate the power of the MOTRIMS method.

For the symmetric system, 7 keV Rb^+ + Rb($5l$), the main capture channels are the resonant ones referred to as Rb(5s)-Rb(5s) and Rb(5p)-Rb(5p). Because these two channels are resonant, they both have Q-values of zero and hence are indistinguishable in a Q-value spectrum. However, for the projectile energy investigated here, probability for charge transfer through non resonant channels is large enough to allow the accurate measurement of these channels. Using these side peaks along with our proven method of chopping the trapping lasers on and off, as presented in section 4.1.1, target excited state fraction was measured.

Figure 4.15 shows experimental results differential in Q-value and scattering angle. The distinct groups of capture channels are clearly visible. Integration along the vertical axis would yield the total Q-value spectrum. As before, setting proper time

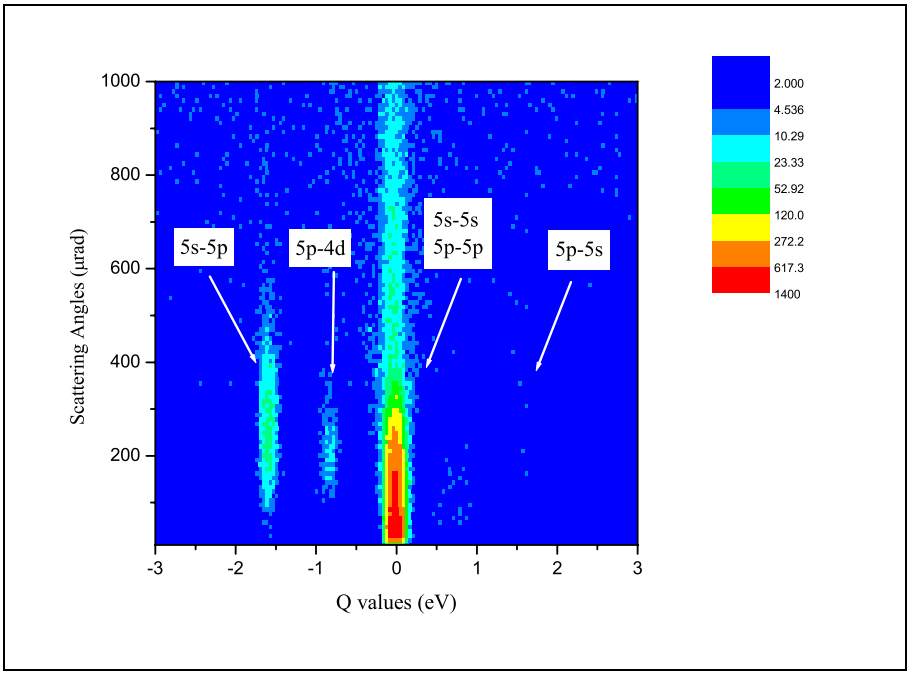

Figure 4.15: *Double Differential Cross Sections for 7 keV Rb^+ + Rb(5l) where l = s and p.*

gates corresponding to the lasers chopping cycle yielded Q-value spectra for trapping lasers on and off. Figure 4.16(a) is the Q-value spectrum taken while the lasers were blocked and Fig. 4.16(b) is the Q-value spectrum taken while the lasers were unblocked. Thus, the former represents capture from the ground state only, while the latter represents capture from both the ground and the excited states. In comparing these two plots, the additional channel opened up through capture from Rb(5p) is readily visible. With the measured excited state fraction, these two curves yield relative cross sections for capture from a pure ground state and a pure excited state into all of the various final states. The excited state fraction, f, is measured by observing the change in the area of a single peak corresponding to capture from the target ground state when the lasers are on and off. In this case, the Rb(5s)-Rb(5p)

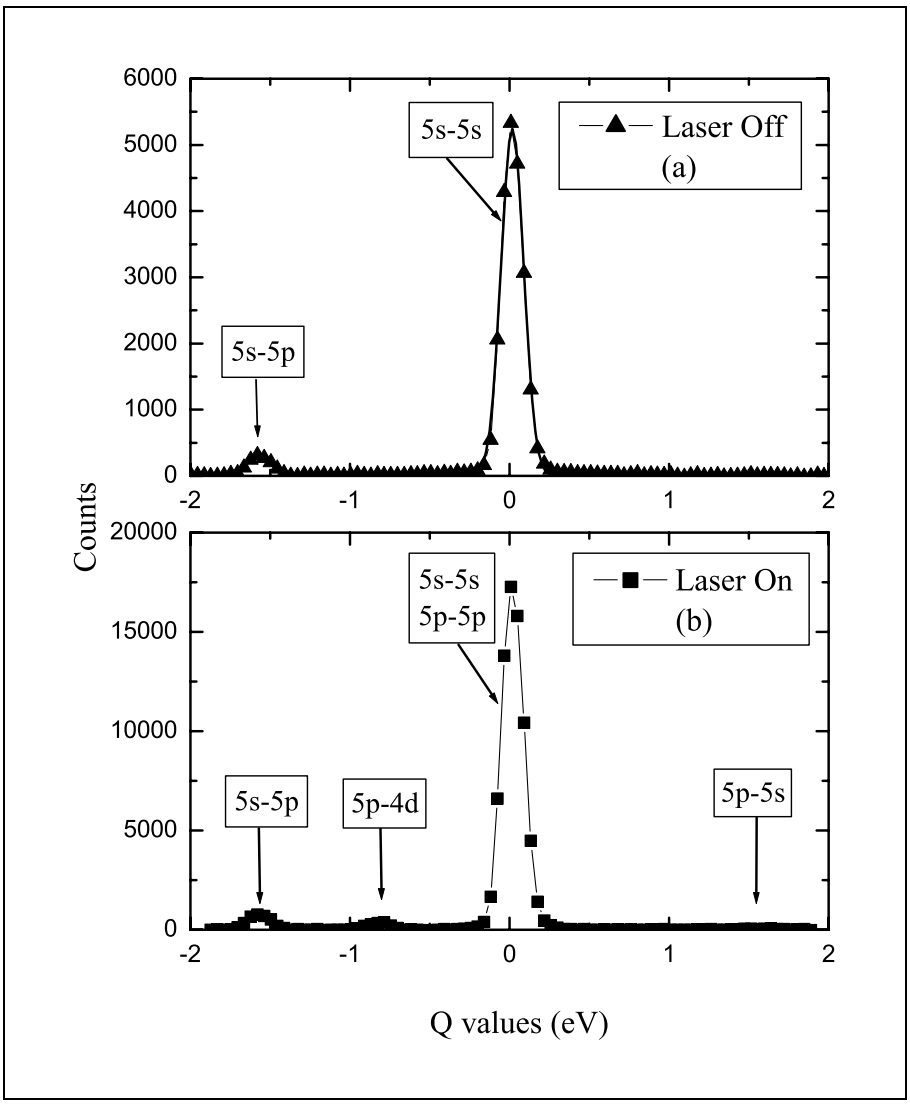

Figure 4.16: *Counts versus Q-value for 7 keV Rb^+ + Rb(5l) where l = s and p. In (a) the trapping lasers are blocked, while in (b) they are unblocked.*

channel was used to measured target excited state fraction:

$$f = 1 - \frac{A_{sp}^{on} T^{off}}{A_{sp}^{off} T^{on}}, \tag{4.3}$$

where A_{sp}^{on} and A_{sp}^{off} are the areas under the Rb(5s) to Rb(5p) peak while the lasers are on and off, respectively. T^{on} and T^{off} are the times when the laser are on and off, respectively. The excited state fraction for this particular experiment was found to be 0.23 ± 0.02. From the excited state fraction information, contribution to the zero

Channels	Relative Cross Sections
$\frac{\sigma_{5p-5p}}{\sigma_{5p}}$	0.89 ± 0.10
$\frac{\sigma_{5p-4d}}{\sigma_{5p}}$	0.09 ± 0.01
$\frac{\sigma_{5p-5s}}{\sigma_{5p}}$	0.02 ± 0.01
$\frac{\sigma_{5s-5s}}{\sigma_{5s}}$	0.94 ± 0.11
$\frac{\sigma_{5s-5p}}{\sigma_{5s}}$	0.06 ± 0.01
$\frac{\sigma_{5p}}{\sigma_{5s}}$	0.95 ± 0.13

Table 4.11: *Experimental relative charge transfer cross sections for 7 keV Rb^+ + Rb(5l), where l = s and p.*

Q-value peak from Rb(5s) to Rb(5s) (A_{ss}^{on}) and Rb(5p) to Rb(5p) (A_{pp}^{on}) channels are given by:

$$A_{ss}^{on} = A_{ss}^{off} \frac{T^{on}}{T^{off}} (1 - f), \tag{4.4}$$

and

$$A_{ss,pp}^{on} = A_{ss}^{on} + A_{pp}^{on}. \tag{4.5}$$

From these expressions, one can easily obtain the relative cross sections. They are reported in Table 4.11. The dominant process is in resonant charge transfer channels. Furthermore, the relative total cross sections from ground and excited states differ

by a factor of 0.95.

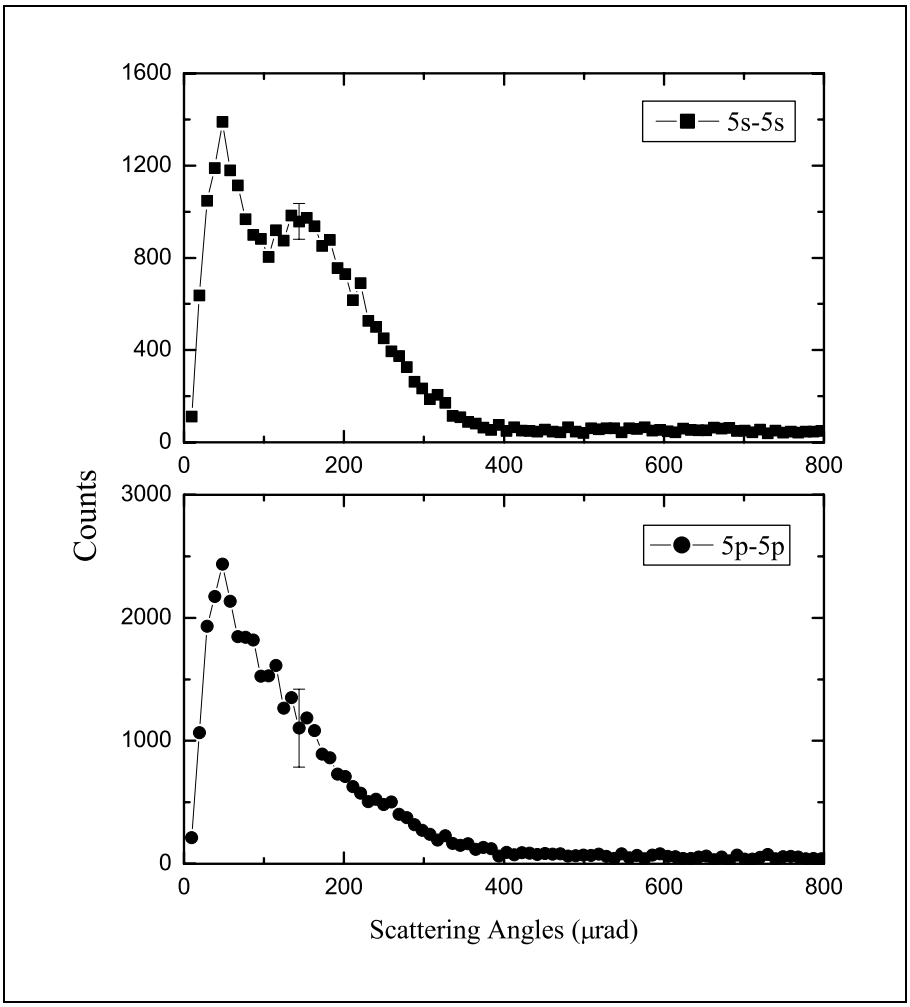

Figure 4.17: *Resonant charge transfer differential cross sections for 7 keV Rb(5s)-Rb(5s) and Rb(5p)-Rb(5p).*

Differential cross sections for the completely degenerate channels, namely, capture from Rb(5s) to Rb(5s) and capture from Rb(5p) to Rb(5p) are measured and are presented in Fig. 4.17. Figure 4.18 shows differential cross sections for the non-resonant charge transfer channels. Note in Fig. 4.15 that there is a strong preference for the endoergic electron transfer channels in term of energy defect. Namely, even though the magnitude of the Q-values are equal, capture channel Rb(5s)-Rb(5p) is dominant over that for the Rb(5p)-Rb(5s) channel. This is somewhat counterintuitive

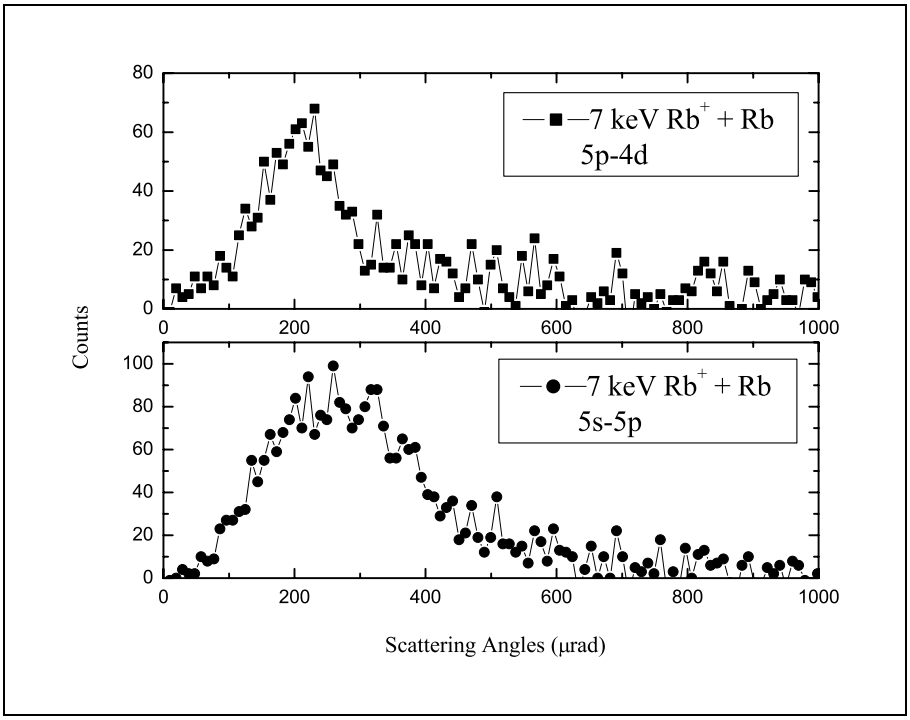

Figure 4.18: *Differential charge transfer cross sections for 7 keV Rb(5p)-Rb(4d) and Rb(5s)-Rb(5p).*

since for this collision system, having symmetry in term of energy defect, one would expect that the exoergic process would prevail and be dominant over the endoergic process simply from the standpoint of increase in entropy in the system when collision occurs.

Theoretical Interpretation

For symmetric systems, all things being equal, one might expect that the exoergic processes be preferred. This counterintuitive feature can be understood through inspection of the potential curves in Fig. 4.19. For the exoergic channel Rb(5p)-Rb(5s), the main transfer mechanism is the rotational coupling between Σ and Π at internuclear separation of about 7 a.u.. However, this has to compete with the radial coupling of the endoergic charge exchange channel Rb(5p)-Rb(4d) which takes place

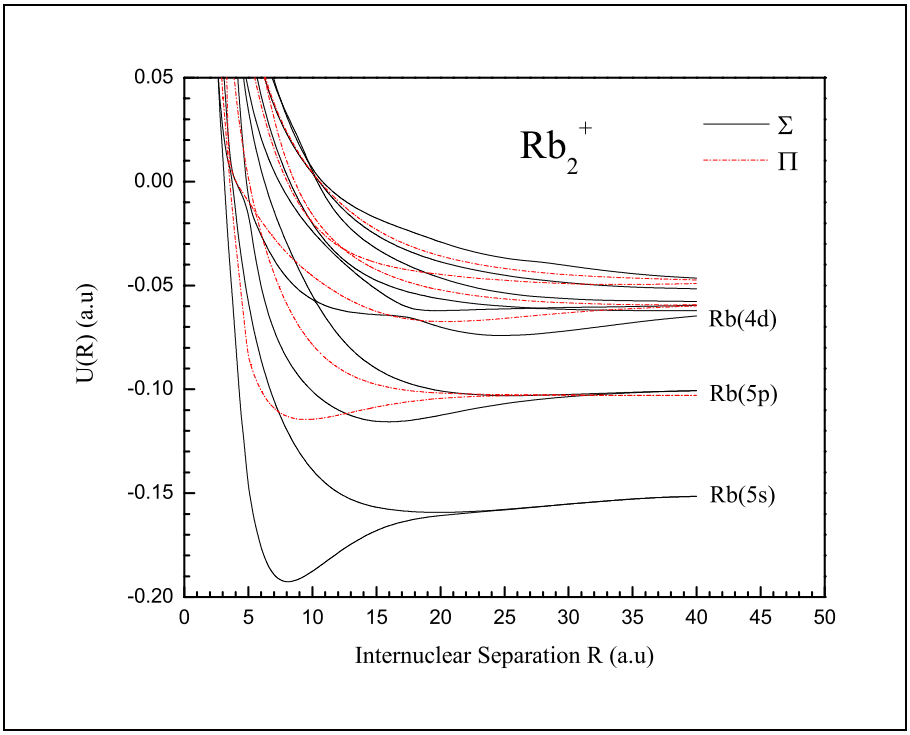

Figure 4.19: *Rubidium molecular potential curves.*

at internuclear separation of about 10 a.u.. Whereas for the endoergic channel with the same magnitude in energy defect, Rb(5s)-Rb(5p), the rotational coupling is the overwhelmingly dominant process for capture into Rb(5p).

Another observation is that the angular differential cross sections for resonant electron capture channels are peaked at smaller angles, reflecting the fact that capture occurs at larger impact parameters. In contrast, for non-resonant channels, namely Rb(5s)-Rb(5p) and Rb(5p)-Rb(4d), capture occurs at larger scattering angles, reflecting the efficient rotational coupling at internuclear distances at about 10 a.u.. Furthermore, the angular capture cross section for channel Rb(5s)-Rb(5s) exhibits oscillatory structure, which can be seen in Fig. 4.17. This is due to the radial coupling of the ground state potential curves, Σ_u and Σ_g, which give rise to the interference effect. For the capture channel Rb(5p)-Rb(5p), this effect is significantly lessened

since the interference is no longer due to only two states but rather of four states including the Π_u and Π_g. The oscillatory structure might be washed out because of the summing over many phase differences.

4.1.4 The Dual Beam Method

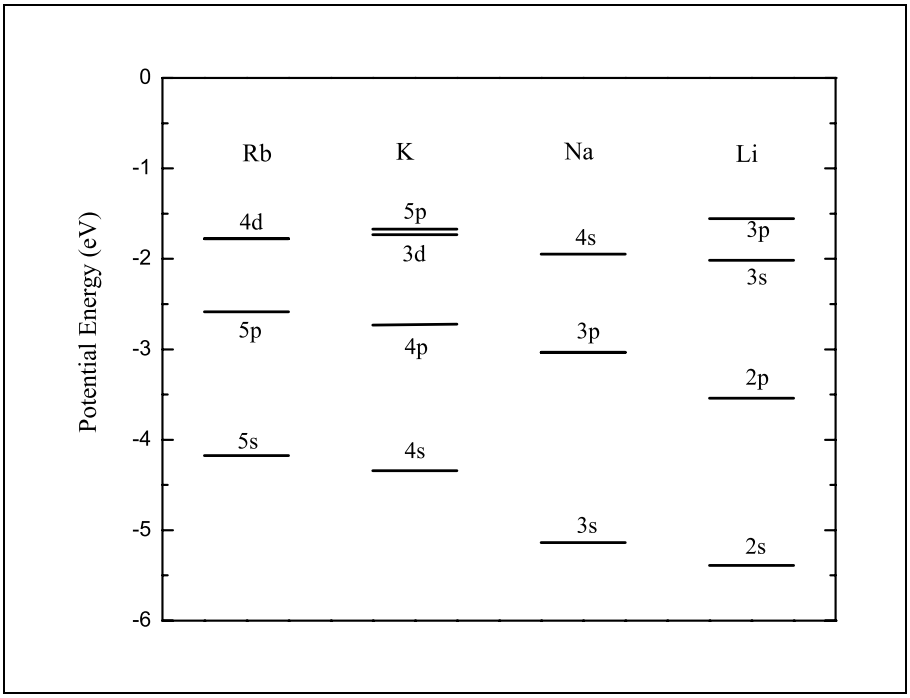

Figure 4.20: *Energy levels of alkali atoms [76].*

Through the superior Q-value resolution of MOTRIMS, the task of obtaining excited state fractions and relative cross sections is relatively trivial for systems with non-degenerate channels such as $Na^+ + Rb(5l)$ [83]. However, even with MOTRIMS's superior Q-value resolution, it is unclear how relative capture cross sections or differential cross sections can be measured for systems with capture channels that are nearly energetically degenerate *e.g.* $Li^+ + Rb(5l)$ or $K^+ + Rb(5l)$, since excited state fractions can not measured from Q-value spectra. Figure 4.20 shows some of the energy levels relevant to the alkali ion - alkali atom systems [76]. From this figure,

one can see that for the above mentioned systems, no pure single peak corresponding to capture from ground state Rb(5s) exists. In this case, an ion source producing two different type of projectiles, one of which is Na^+ was used. Because the two ion species have the same energy, but different masses, the capture channels for the different projectile species are well-separated in the time of flight or Q-value spectra. In this way, the Na^+ ion can be used to obtain the excited state fraction, while the capture cross sections are measured for the other projectile species.

7 keV K^+ + Rb(5l)

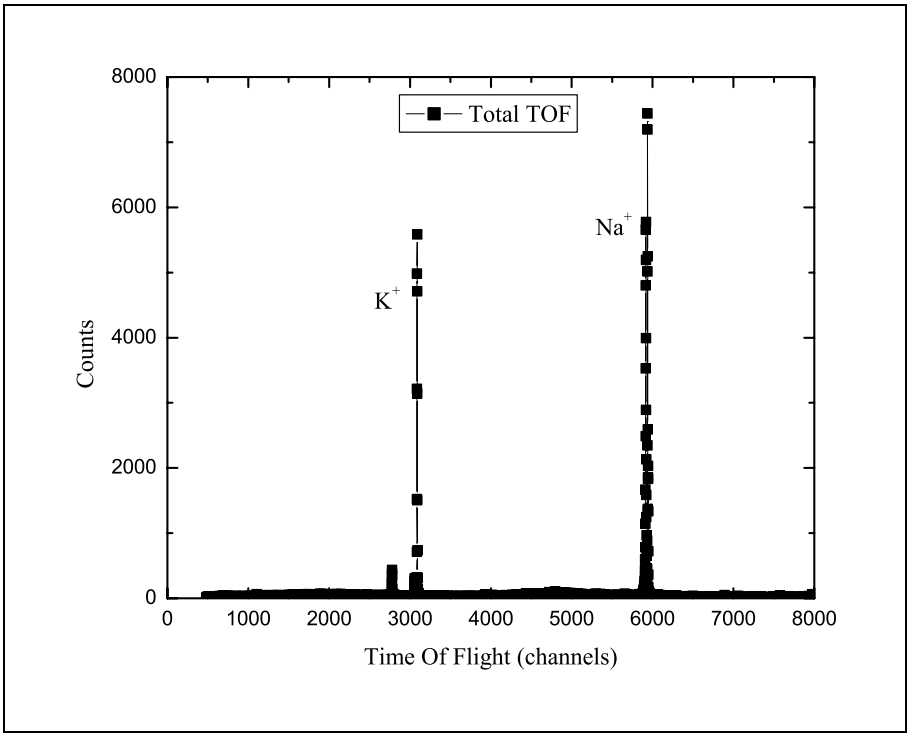

Figure 4.21: *Total time of flight for coincidences from both Na^+ + Rb(5l) and K^+ + Rb(5l), where l = s and p, in the dual beams method.*

Here, the dual beam method is employed to investigate the 7 keV K^+ + Rb(5l) system. Figure 4.21 shows a total time of flight spectrum which includes recoil ion signatures for coincidences from both the Na^+ and K^+ projectiles. By "zooming

in" on the Na^+ portion of the spectrum, one can measure the excited state fraction of the Rb target in the usual way. Figure 4.22 shows coincidences with the Na^+

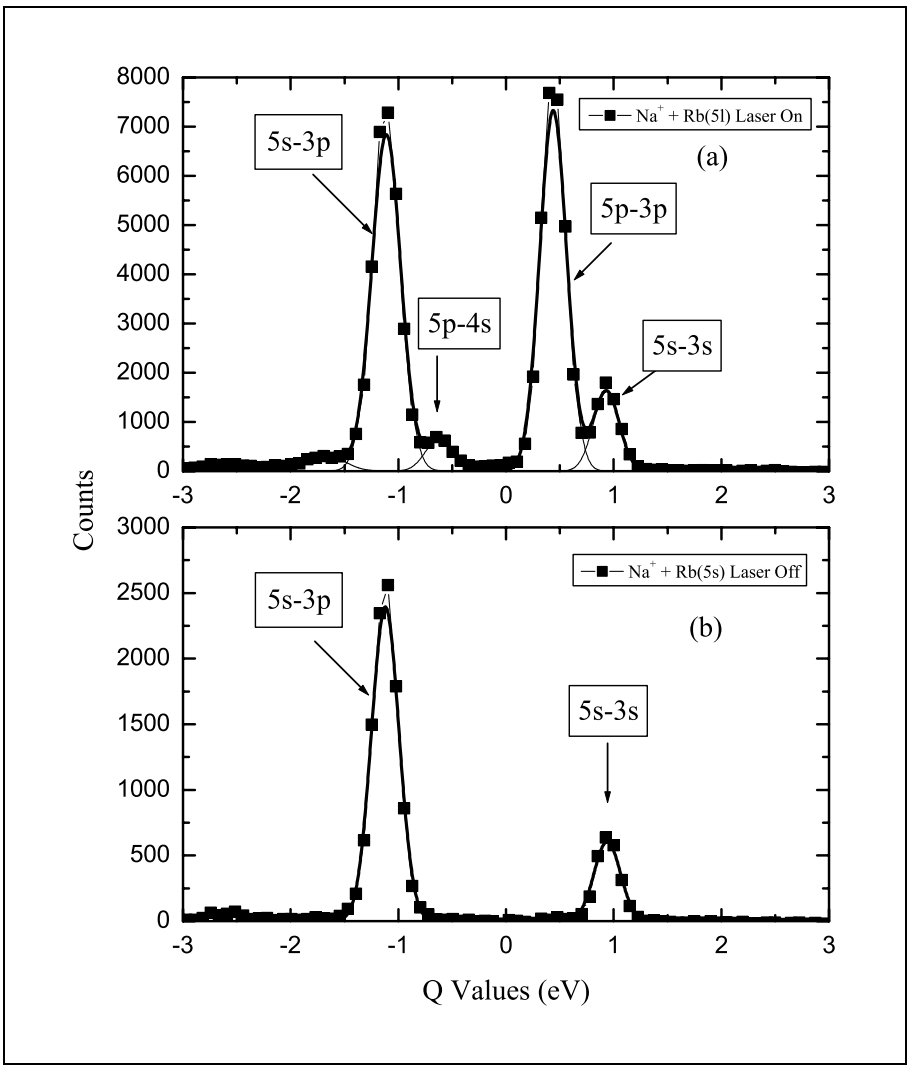

Figure 4.22: *The 7 keV Na^+ + Rb(5l),where l = s and p, collision system used to probe target excited state fraction.*

projectile. The upper and lower panels show the Q-values when then lasers are on and off, respectively. The target excited state fraction is obtained from (similar to Eq. 4.3):

$$f = 1 - \frac{A_{ss}^{on} T^{off}}{A_{ss}^{off} T^{on}}, \tag{4.6}$$

where A_{ss}^{on} and A_{ss}^{off} are amplitudes of capture from Rb(5s) to Na(3s) when the lasers are on and off, respectively. For this particular experiment the excited state fraction was 0.21 ± 0.02.

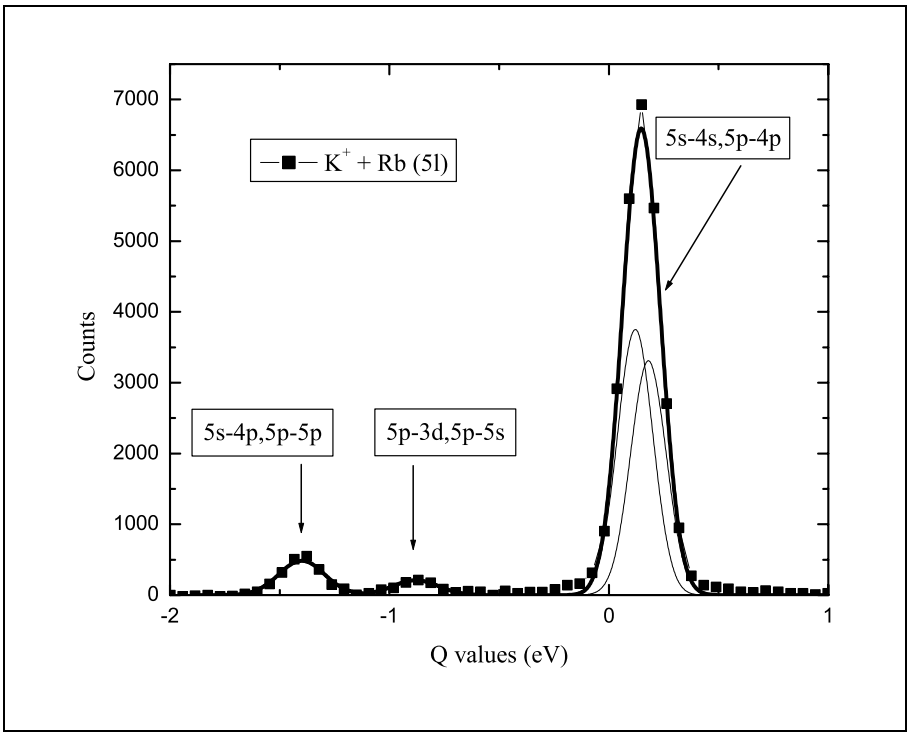

Figure 4.23: *Q-value spectrum for 7 keV K^+ + Rb(5l), where l = s and p, collision system.*

Knowing the target excited state fraction, one can deduce the kinematically complete relative cross sections for the system 7 keV K^+ + Rb(5l) from the Q-value spectrum of Fig. 4.23. That is,

$$\frac{\sigma_p}{\sigma_s} = (\frac{1}{f} - 1)\frac{\sum A_p}{\sum A_s}, \tag{4.7}$$

where f is the measured excited state fraction of Rb target deduced from the Na^+ measurement. $\sum A_p$ and $\sum A_s$ represent the combined areas under all the Q-value

Channels	Relative Cross Sections
$\frac{\sigma_{5p-5p}}{\sigma_{5p}}$	0.004 ± 0.025
$\frac{\sigma_{5p-4p}}{\sigma_{5p}}$	0.848 ± 0.183
$\frac{\sigma_{5p-3d}+\sigma_{5p-5s}}{\sigma_{5p}}$	0.148 ± 0.037
$\frac{\sigma_{5s-4s}}{\sigma_{5s}}$	0.909 ± 0.043
$\frac{\sigma_{5s-4p}}{\sigma_{5s}}$	0.091 ± 0.007
$\frac{\sigma_{5p}}{\sigma_{5s}}$	1.381 ± 0.302

Table 4.12: *Experimental relative charge transfer cross sections for 7 keV K^+ + Rb(5l), where l = s and p.*

peaks for all channels capture from Rb(5p) and Rb(5s), respectively. In order to differentiate between overlapping channels in $\sum A_p$ and $\sum A_s$ we again use the excited state fraction information:

$$A^{on}_{nl-nl'} = A^{off}_{nl-nl'} \frac{T^{on}}{T^{off}}(1-f). \tag{4.8}$$

where nl and nl' are initial and final states, respectively. The experimental relative cross section results for this system are presented in Table 4.12.

Scattering angle results for the main charge exchange channels were also obtained and are reported in Fig. 4.24. The dominant process for capture from ground state Rb(5s) is the Rb(5s)-K(4s) channel. The dominant process for capture from the

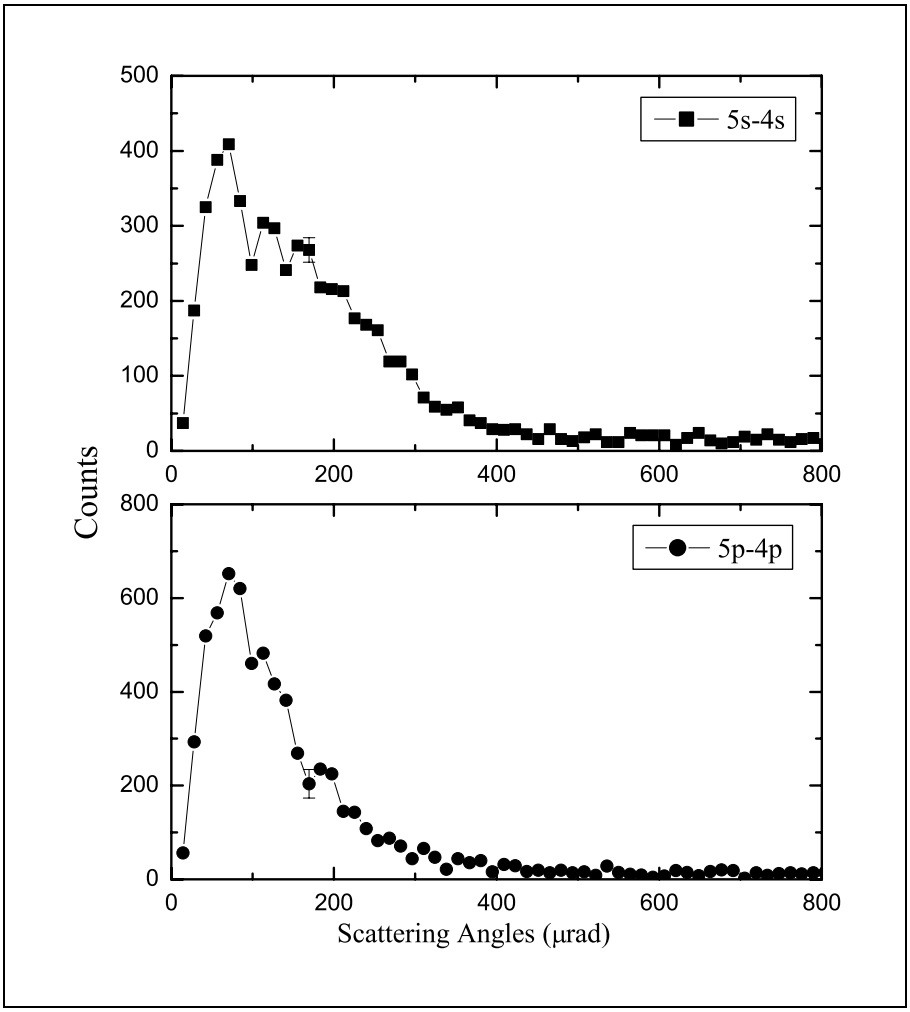

Figure 4.24: *Differential cross sections for 7 keV K^+ + Rb(5l), where l = s and p, collision system.*

excited state Rb(5p) is the Rb(5p)-K(4p) channel.

7 keV Li^+ + Rb(5l)

The dual beam method is again used to measure relative cross sections for the system 7 keV Li^+ + Rb(5l). Here, because the Na^+ component of our dual beam source was so weak, the Na^+ + Rb collision system used to deduce excited state fraction yielded inadequate counts in the Rb(5s)-Na(3p) channel as can be seen in Fig 4.25. This would have presented a problem with large error bars in the excited state fraction

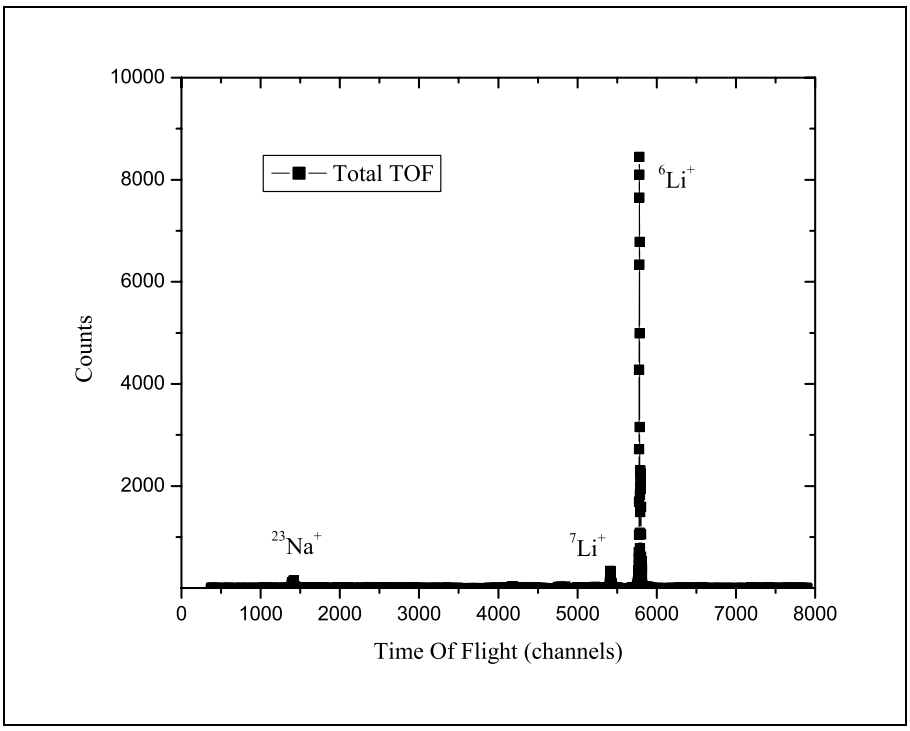

Figure 4.25: *Total time of flight for both coincidences from Na^+ + Rb(5l) and Li^+ + Rb(5l), where l = s and p, observed for dual beam method.*

determination.

However, from first principles,

$$A_s^{off} \propto \sigma_s(n_s^{on} + n_p^{on})T^{off}, \tag{4.9}$$

$$A_s^{on} \propto \sigma_s n_s^{on} T^{on}, \tag{4.10}$$

$$A_p^{on} \propto \sigma_p n_p^{on} T^{on}, \tag{4.11}$$

where A_s^{on} and A_s^{off} are total capture areas from Rb(5s) when the lasers are on and off, respectively. A_p^{on} is the total capture from Rb(5p) when the lasers are on. From the equations above, the target excited fraction, f, can be obtained *via*:

$$f = \frac{A_p^{on} T^{off} \sigma_s}{A_s^{off} T^{on} \sigma_p}. \tag{4.12}$$

The ratio $\frac{\sigma_p}{\sigma_s}$ is known with high accuracy through the completely independent experiments of section 4.1.1 and are in good agreement with theoretical prediction [83].

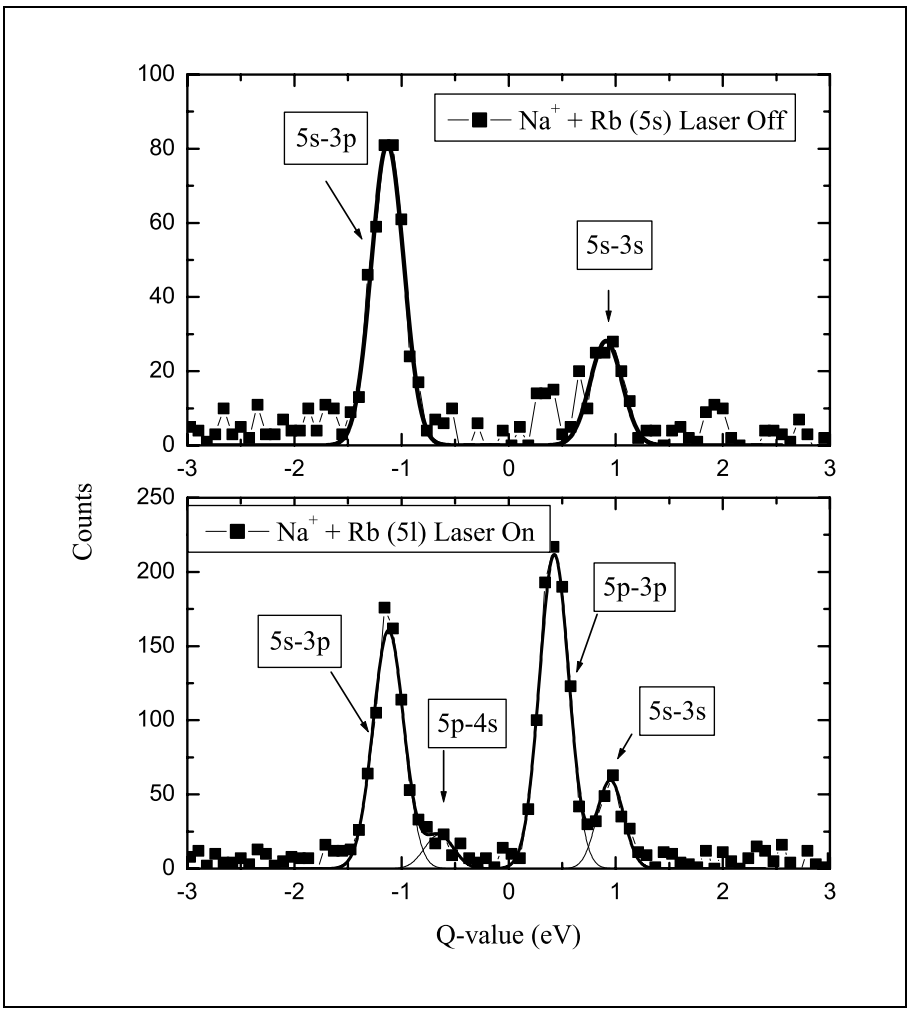

Figure 4.26: *Na^+ + Rb(5l),where l = s and p, collision system used to probe target excited state fraction.*

The ratio $\frac{A_p^{on}}{A_s^{off}}$ was measured from the Q-value spectrum gated on the Na^+ + Rb(5l) collisions as in Fig. 4.26. For this particular experiment, the target excited state fraction was measured to be 0.19 ± 0.04.

From Eqs. 4.9 and 4.11,

$$\frac{\sigma_p}{\sigma_s} = \frac{A_p^{on} T^{off}}{A_s^{off} T^{on} f}. \tag{4.13}$$

Here, A_s^{off} and A_p^{on} are total areas in capture from Rb(5s) when the lasers are off, and total areas in capture from Rb(5p) when the lasers are on for the Li^+ + Rb(5l)

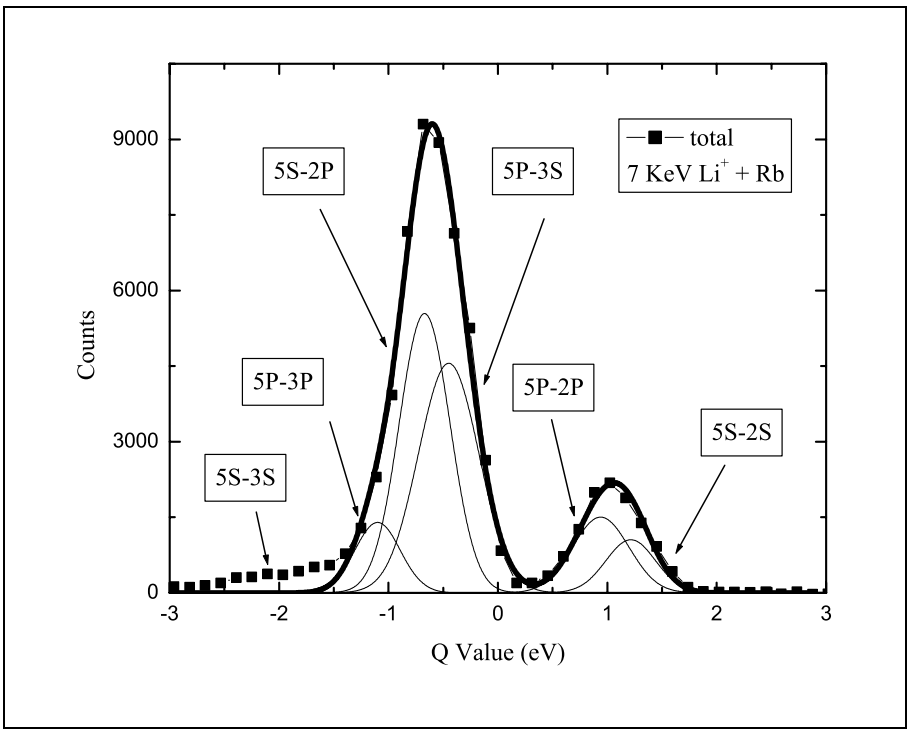

Figure 4.27: *Q-value spectrum for 7 keV Li^+ + Rb(5l), where l = s and p, collision system.*

collision system. These areas can be extracted from Fig. 4.27.

In order to differentiate between overlapping channels, as seen in Fig. 4.27, we again used the excited state fraction information through the formalism presented in Eq. 4.8. The experimental relative cross section results for this system are presented in Table 4.13. The charge transfer channel Rb(5s)-Li(2p) dominates the total capture from Rb(5s). Charge transfer from Rb(5p) is more uniformly distributed among the three major channels.

Differential cross sections in term of scattering angles are also measured. Shown in Fig. 4.28 are the differential cross sections for the two dominant capture channels Rb(5p)-Li(2p) and Rb(5s)-Li(2s). In both of these, a hint of structure can be seen just beyond the present resolving power of the apparatus.

Channels	**Relative Cross Sections**
$\frac{\sigma_{5p-3p}}{\sigma_{5p}}$	0.33 ± 0.04
$\frac{\sigma_{5p-3s}}{\sigma_{5p}}$	0.47 ± 0.06
$\frac{\sigma_{5p-2p}}{\sigma_{5p}}$	0.20 ± 0.03
$\frac{\sigma_{5s-2s}}{\sigma_{5s}}$	0.17 ± 0.08
$\frac{\sigma_{5s-2p}}{\sigma_{5s}}$	0.83 ± 0.02
$\frac{\sigma_{5p}}{\sigma_{5s}}$	0.67 ± 0.09

Table 4.13: *Experimental relative charge transfer cross sections for 7 keV* Li^+ + *Rb(5l), where* $l = s$ *and* p.

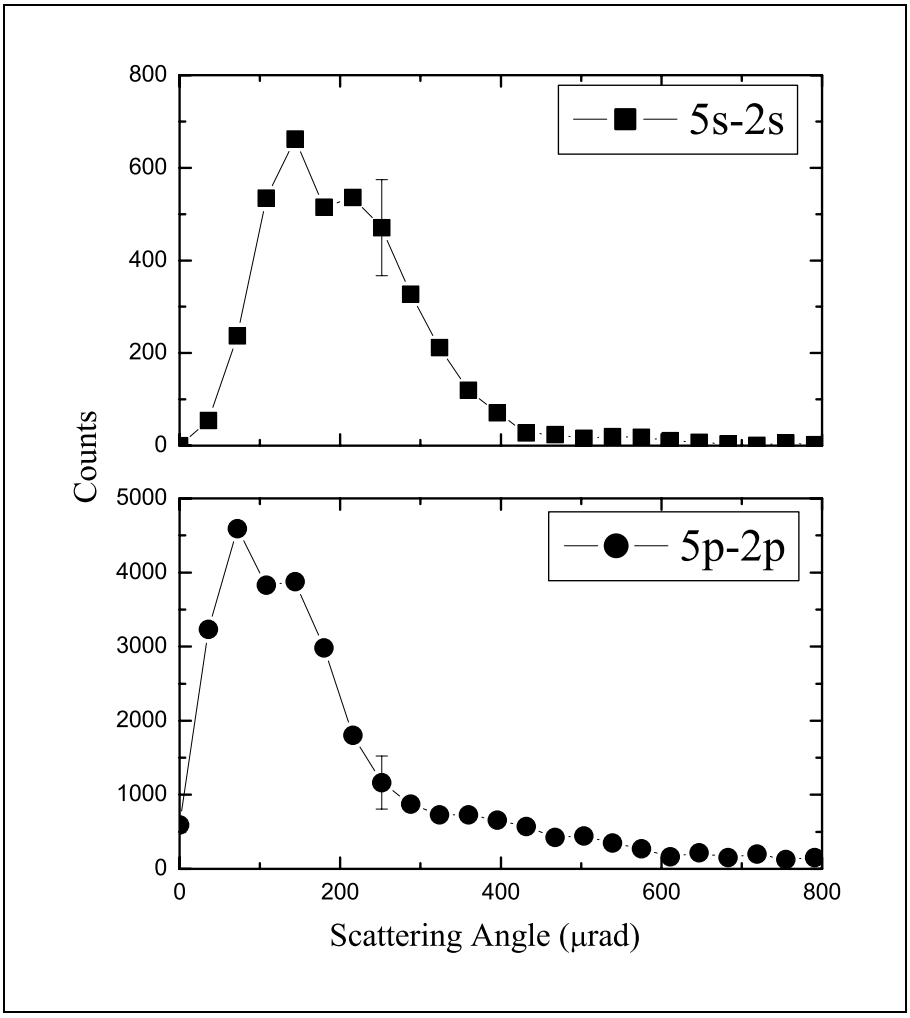

Figure 4.28: *Differential cross sections for 7 keV Li^+ + Rb(5l), where l = s and p, collision system.*

4.2 Magneto Optical Trap Population

Magneto Optical Trap (MOT) has become an enabling technology for many areas of atomic, molecular, and optical physics. Examples include Bose-Einstein condensate and degenerate Fermi gas formation, photo-association, slowing of the speed of light, electromagnetically induced transparency, high resolution spectroscopy, etc. In many of these studies, knowledge of population dynamics can provide greatly needed insight. However, reliable measurements of excited state populations, either dynamic or steady

state, are often difficult. The determination of the relative populations in a laser-excited system generally relies on some model-dependent measurement[65, 75] and can often become the dominant source of uncertainty in the understanding of the process under study. It is important to distinguish here between uncertainty in a measurement from uncertainty in a model. Both lead to uncertainty in population, but often only the former source of uncertainty is represented in experimental error bars. In addition, if the excitation of the trapped atoms is not steady-state, then the level populations are dynamic, requiring more complicated models and even greater uncertainty. Often, lasers are used to probe the system under study. This can have the unfortunate side effect of modifying the very populations one wishes to measure.

A specific case in which knowledge of excited state fraction is critical is the measurement of relative charge transfer cross sections from excited targets as is the main focus of this dissertation. Because measured charge transfer rates are proportional to the product of the cross section for transfer from some state and the population of that state, one must have an independent measurement of the relative populations in order to obtain the cross sections.

The conditions essential for the success of using MOTRIMS as a probe at MOT population dynamics are that the relative capture rates from, and into the various channels can be distinguished, and that the target is cold. Both conditions are met by the method previously explained in Chapter 3. The method can be generalized to an arbitrary number of excited levels in the target, the only limitation being the Q-value resolution of the MOTRIMS technique. Any target atom or molecule undergoing charge transfer is effectively "destroyed". However, singly charged ions interact much less strongly with the target than do near-resonant photons, which are highly perturbative. Thus only a very small fraction of the target is modified through interaction with an ion beam. The new method is independent of the mechanism

by which the target has been excited, and is essentially non-intrusive which makes it ideal as a probe of physical processes in magneto-optical traps which result in excited states. Thus the method described in this dissertation may be considered as a powerful tool not just for charge transfer measurements but a dynamical tool for using charge transfer to probe population dynamics in a magneto-optical trap.

The prototypical collision system used as a probe is the 7 keV Na^+ + Rb($5l$). A typical Q-value spectrum for this collision is shown in Fig. 4.29. The points represent data, while the solid line is the sum of Gaussian fits to the individual peaks.

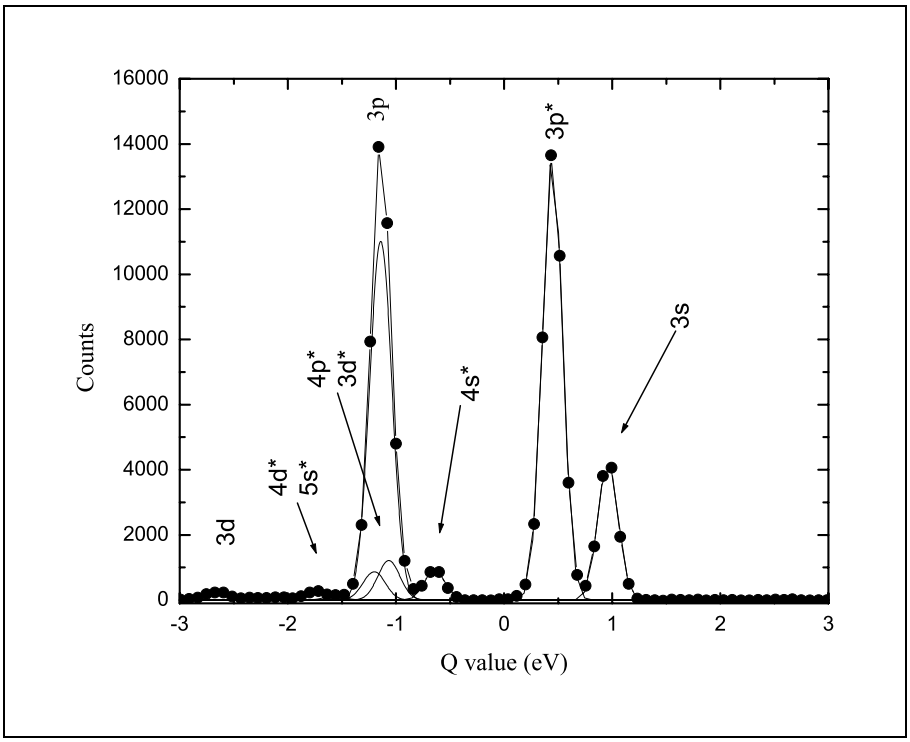

Figure 4.29: *Q-value plot for the 7 keV Na^+ + Rb(5l), where l = s and p, collision system. Both lasers driving the Rb(5s)-Rb(5p) transition are on. Peak labels containing a star indicate channels where capture is from the Rb(5p) state. Other peaks represent capture from the ground state Rb(5s). The solid line is the sum of Gaussian fits to the individual peaks.*

The basic use of the MOTRIMS method has already been demonstrated [45] and described in detail in previous sections for measurements of final and initial

state dependent, differential in scattering angle, charge transfer cross sections for a rubidium target in a mixture of RB(5s) and Rb(5p) states. The key notion is that the high resolution Q-value measurement allows one to determine which capture events came from the ground state and which came from the excited state. Thus, by chopping the trapping lasers and comparing the change in charge transfer rates from the ground and excited states for lasers on and lasers off, one can determine the excited state fraction and, independently, the relative capture cross section from both states. If A_i refers to the area under a Q-value peak corresponding to charge transfer from the target's i^{th} initial state whose relative population is given by n_i, to a particular final state, then

$$A_s \propto \sigma_s n_s \tag{4.14}$$

$$A_p \propto \sigma_p n_p, \tag{4.15}$$

where the constant of proportionality contains acquisition time and geometric factors. With a high enough chopping frequency (in the case of this work, greater than 10 kHz)

$$n_s + n_p = constant, \tag{4.16}$$

and therefore

$$\Delta A_s \propto \sigma_s \Delta n_s \tag{4.17}$$

$$\Delta A_p \propto \sigma_p \Delta n_p \tag{4.18}$$

$$\Delta n_s + \Delta n_p = 0, \tag{4.19}$$

where Δn_i refers to changes in the ith population as the trapping (and/or re-pumping) laser goes from the on condition to the off condition. Note that it is the low temper-

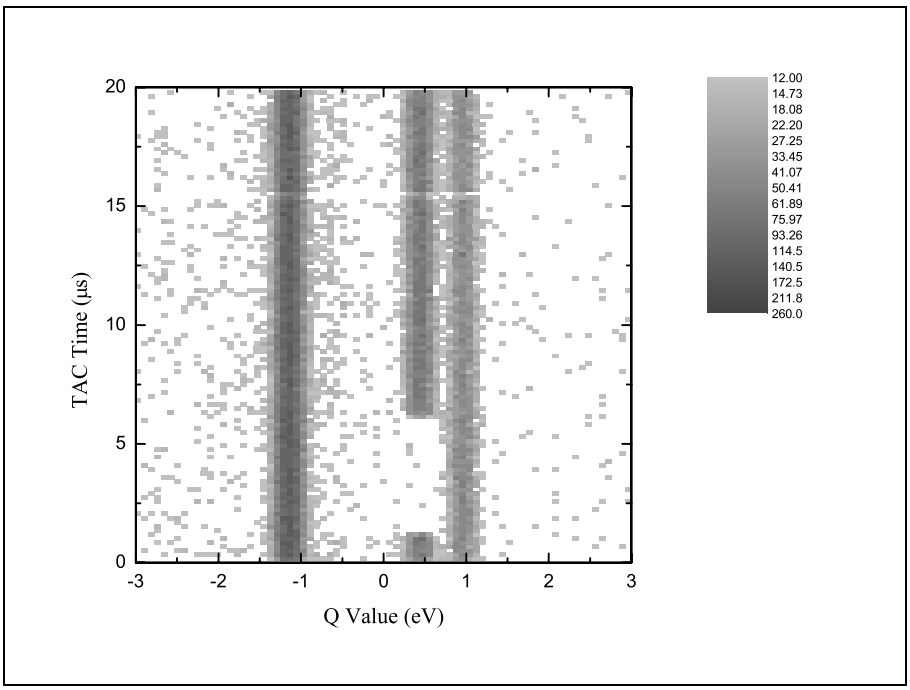

Figure 4.30: *TAC signal versus Q-value. The vertical lines can be compared with the peaks of Fig. 4.29. Broken lines correspond to capture from excited states.*

ature of the target which allows Eqs. [4.16] and [4.19] to be satisfied at relatively low chopping frequencies.

Taking the ratio of Eq. [4.18] to Eq. [4.17], and using Eq. [4.19] we obtain

$$\frac{\Delta A_p}{\Delta A_s} = \frac{\sigma_p}{\sigma_s}\frac{\Delta n_p}{\Delta n_s} = -\frac{\sigma_p}{\sigma_s}. \tag{4.20}$$

Then, using this with Eqs. [4.2] and Eq. [4.16],

$$\frac{n_p}{n_s} = \frac{\sigma_s}{\sigma_p}\frac{A_p}{A_s} = -\frac{A_p}{A_s}\frac{\Delta A_s}{\Delta A_p}. \tag{4.21}$$

A plot of TAC output *versus* Q-value is shown in Fig. 4.30. One can readily set a gate on selected individual capture channels in this figure and directly measure A_i, ΔA_i, n_i, and Δn_i for use in Eq. 4.20 and 4.21. Here, we use the cross section ratio for the Rb(5p)-Na(3p) channel to the Rb(5s)-Na(3s), and then use the entire Q-value

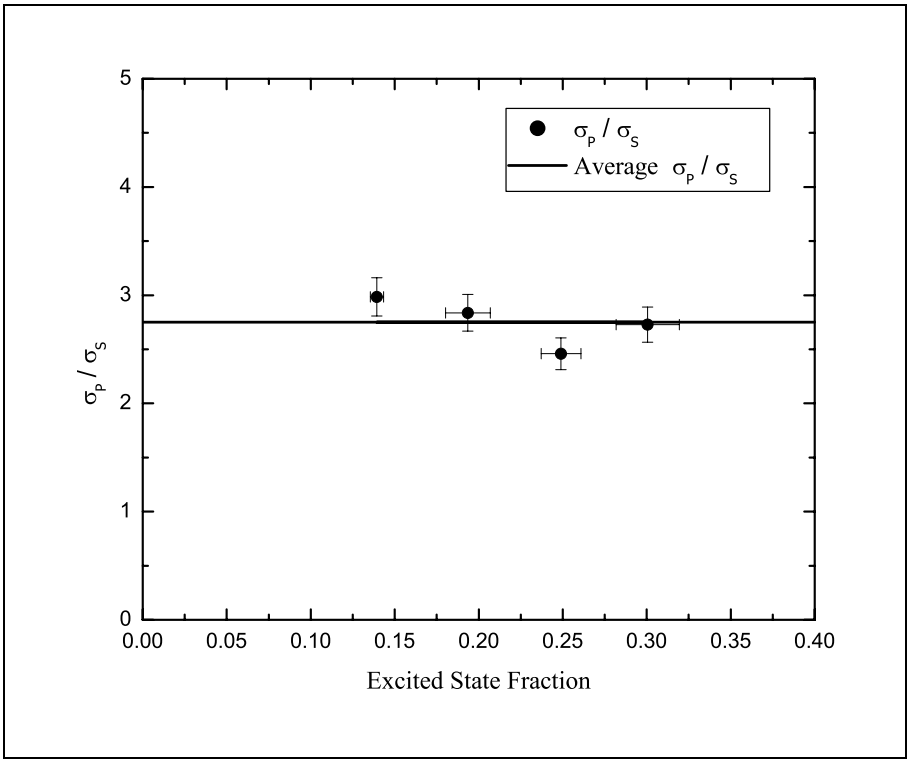

Figure 4.31: *Ratio of capture cross sections* versus *measured excited state fraction. Error bars are absolute.*

spectrum to convert from this ratio of partial cross sections to a ratio of total cross sections.

To show the validity of this technique for measuring f, a series of measurements was made in which the excited state fraction in the MOT was varied by changing the detuning of the trapping laser. In each of these measurements the ratio of the capture cross sections and the excited state fractions were independently determined using the above equations.

The results are shown in Fig. 4.31. The capture cross sections discussed here refer to randomly oriented targets since both the trapping and re-pumping beams are incident from all three orthogonal directions. The error in the measurements is dominated by counting statistics. The figure shows that within the error bars shown, the cross section ratio is a constant, independent of excited state fraction - as it

must be. The measured cross section ratio of 2.75 ± 0.01 is completely consistent with coupled channel calculation [83]. Figure 4.31 shows that with the MOTRIMS technique one can readily measure even small variations in excited state fraction. If, instead, fluorescence were used to try to measure the fraction, one would have to somehow measure and correct for the varying total MOT number. With the methodology described here, this is clearly not necessary.

As a demonstration of the versatility of the technique for studying MOT dynamics on a long time scale, the AOM was left on (*i.e.* it passes both the trapping and re-pump beams) and only the re-pump laser beam was mechanically chopped at 200Hz with an on-time duty cycle of 75%. In order to measure the time dependence of the Rb(5s) and Rb(5p) populations, a triangle wave signal, synchronous with the mechanical chopper, was sent to the analog-to-digital converter of the data acquisition computer, in place of the TAC signal. Q-value spectra were then sorted by triangle-wave voltage and phase, and Eq. 4.21 was used to obtain the temporal evolution of the Rb(5s) and Rb(5p) states of the target. This can be done now that σ_p/σ_s has been measured. One can readily see the decay of the Rb(5p) population, resulting from optical pumping to the F=1 of the ground state.

The technique used to determine the charge transfer cross sections and relative populations is completely general, and could in principle be used to determine cross sections and populations for a system containing N levels. Eqs. 4.20 and 4.21 can be generalized to expressions for the kth level ($2 \leq k \leq N$):

$$\frac{\sigma_k}{\sigma_1} = -\Delta A_k \left(\sum_{i=1}^{k-1} \Delta A_i \frac{\sigma_1}{\sigma_i} \right)^{-1} \tag{4.22}$$

$$\frac{n_k}{n_1} = \frac{\sigma_1}{\sigma_k} \frac{A_k}{A_1}, \tag{4.23}$$

where the subscript "1" indicates the lowest level, and the Δ refers to changes as the

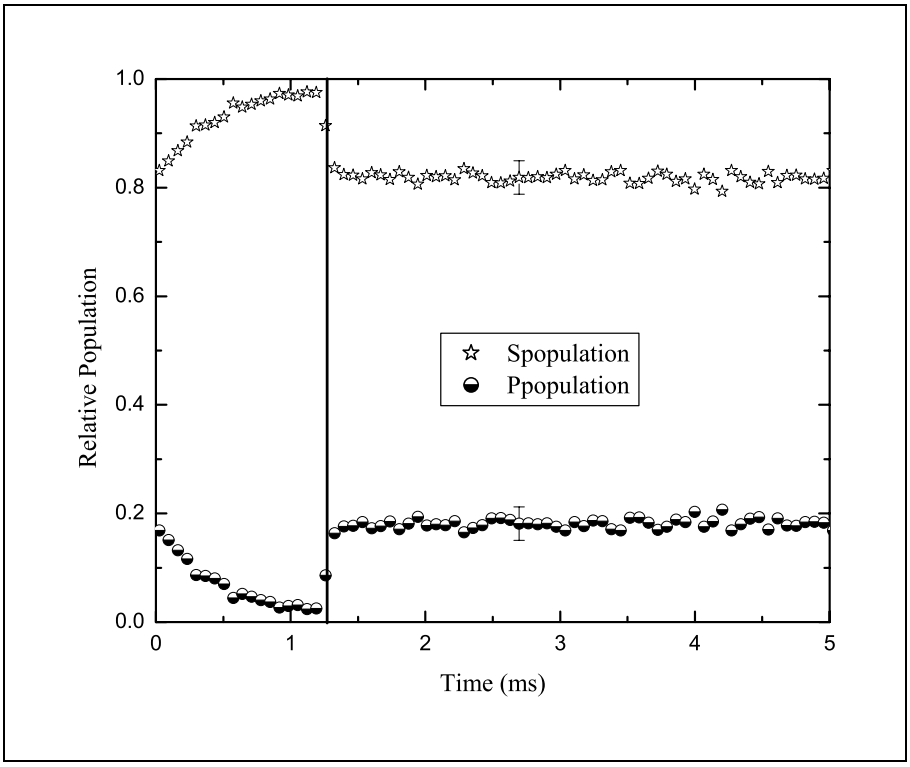

Figure 4.32: *Time dependence of relative Rb(5s) and Rb(5p) populations. At $t = 0$, the light from the "repump" laser was blocked. The vertical line near 1.2 ms indicates at which point the beam was turned back on. Representative error bars are absolute; relative error is smaller than the size of the points.*

laser driving the kth level is chopped on and off. The terms σ_i/σ_1 are sequentially determined for all $i \leq k$ by iteratively using Eq. 4.22. Once all of the relative cross sections are determined, Eq. 4.23 can be used to determine the temporal evolution of each of the N levels.

Using the MOTRIMS technique, resolution in the time evolution of the populations in a system is limited only by the TAC resolution, here, a few nsec. It is apparent that this technique is more than just a tool for the determination of charge transfer cross sections, but rather is a very general and powerful method for studying the temporal evolution of level populations in a MOT under the influence of some perturbation. Example systems which one might study include the formation of cold

molecules [84] or cold Rydberg plasmas [85, 86]. One could as well study the dynamics of a MOT being dressed by a fast laser pulse, or the influence on populations by the "coupling" laser in an electromagnetically induced transparency experiment [87].

The limitations of the technique are determined by the resolution in the Q-value spectrum, and the amount of degeneracies in Q-value for the charge transfer channels available. From Eq. 3.12 the resolution in Q-value is directly related to the resolution in $P_{R_\parallel}$ and to the projectile velocity. The number of channels available in a charge transfer collision, and thus the possibility for Q-value degeneracy, also increases with projectile velocity. Thus it is important that one implement this method with the slowest projectiles which are convenient. In the case of the work presented here in which Na^+ at 7 keV produced a spectrum with adequate resolution and minimal Q-value degeneracies. Partly this is due to the extremely low $\Delta P_{R_\parallel}$ obtained in our apparatus. The best $\Delta P_{R_\parallel}$ obtained to date with the Na^+ projectile is 0.033 atomic units.

Chapter 5

Conclusion and Outlook

To conclude this dissertation, an overview of the experiment and elucidation of the implications of the associated results will given. Looking further out beyond the scope of this dissertation, the possibilities for future improvements as well as suggestions for future experimental investigations of interest in atomic molecular and optical physics will be given.

5.1 Conclusion

Rubidium has been cooled, trapped, and prepared as a target for collision studies. The technique presented in this dissertation, Magneto Optical Trap Recoil Ion Momentum Spectroscopy, allows kinematically complete experiments with unprecedented recoil ion momentum resolution. Complete details of the experimental setup were given. Using this MOTRIMS approach, charge transfer cross sections, differential in initial and final state, as well as in scattering angle have been presented for the collision systems of alkali ions on cooled and trapped rubidium in the ground and first excited states. In particular, the experimental results from Na^+ + Rb($5l$), where l = s and p, collision system at various energies were used to compare with TC-AOCC calculations. Excellent agreement was found for both the relative capture cross sections as

well as differential cross sections in terms of scattering angles. In other words, not only the relative cross sections agreed but the angular differential cross sections of collision process were found to be in agreement. However, oscillatory structure seen in the calculated angular distribution could not yet be resolved with the present experimental $\Delta P_{R_\perp}$. The experimental results from the Cs^+ + Rb($5l$) collision system were used to test a modified version of the Demkov model. Comparison between calculation and experiments shows good agreement. However, differential cross sections where experimental results shows oscillatory structure were not reproduced by theory. Thus, the experimental results have provided a rigorous testing ground for the Two Center Atomic Orbital Closed Coupling Calculation as well as a simple Demkov model.

Furthermore, using the MOTRIMS method presented in this dissertation, resonant and energetically degenerate collision systems were studied experimentally. The power of MOTRIMS was demonstrated with a specially prepared projectile source which produced dual beams as a method to investigate energetically degenerate channels. For a symmetric charge transfer collision system, physical insights into a counter-intuitive endoergic preference in charge transfer collisions were obtained with the aid of the appropriate molecular potential curves.

Advantages of the new methodology are increased recoil ion momentum resolution and the extension of the basic COLTRIMS technique to systems with optically active electrons. Furthermore, it was shown that the MOTRIMS methodology can be exploited to provide accurate real-time measurements of excited state fractions in the target.

5.2 Outlook

MOTRIMS can be used as a powerful diagnostic of physical processes taking place in a MOT [88]. For example, one could "dress" the trapped atoms with a short intense pulse of light. At the end of the pulse, the dressed states collapse into some distribution of excited states, as measured in the field-free basis set of the target atoms. These states would immediately begin to decay through a series of cascades. If the "probe" ion beam were on during the entire sequence, the population dynamics of the system could be measured with a time resolution of a few nanoseconds. Exotic schemes, such as STIRAP (stimulated Raman adiabatic passage), coherent population trapping, and electromagnetically induced transparency, all of which can result in the production of "dark states", could be studied to advantage using the MOTRIMS apparatus.

Not stopping there, Photo-Association (PA) of a cooled and trapped sample of atoms could also be studied to advantage since it may be possible using standard MOTRIMS analysis to determine the orientation of the molecules formed during PA. In the target region of MOTRIMS, molecules can be formed using standard method of Photo-Association (PA) [84], break up and be detected to directly probe the molecular orientation with respect to the association laser polarization [89].

Bibliography

[1] A. Dalgarno and S. Lepp, in *Atomic, Molecular, and Optical Physics Handbook*, edited by G. W. F. Drake, (American Institute of Physics, Woodbury, New York, 1996) p. 919.

[2] J. Weisheit, *ibid.*, p. 978.

[3] E. T. Jensen, *ibid.*, p. 1007.

[4] H. Bichsel, *ibid.*, p. 1032.

[5] M. Inokuti, *ibid.*, p. 1045.

[6] W. Fritsch and C. D. Lin, Phys. Rep. **202**, 1 (1991)

[7] R. E. Olson, Phys. Rev. A **27** 1871 (1980)

[8] M. Kimura, R. E. Olson and J. Pascale, Phys. Rev. A **26** 3113 (1982).

[9] T. Nagata, J. Phys. Soc. Jpn. **48** 2068 (1980).

[10] R. M. Stier and C. F. Barnett, Phys. Rev. **109**, 385 (1958).

[11] J. H. Montague, Phys. Rev. **81**, 1026 (1951).

[12] F. Ribe, Phys. Rev. **83**, 217 (1951).

[13] J.W. McConkey, A. Crowe, and M. A. Hender, Phys. Rev. Lett. **29**, 1 (1972).

[14] L.J. Puckett and D.W. Martin, Phys. Rev. A **5**, 1432 (1976).

[15] W. Steckelmacher, R. Strong, and M. W. Lucas, J. Phys. B **11**, 1553 (1978).

[16] R. E. Olson, J. Ullrich, and H. Schmidt-Böcking, Phys. Rev. A **39**, 5572 (1987).

[17] J. Ullrich, R. E. Olson, R. Dörner, V. Dangendorf, S. Kelbch, H. Berg, and H. Schmidt-Böcking, J. Phys. B **22**, 627 (1989).

[18] R. Dörner, J. Ullrich, H. Schmidt-Böcking, and R. E. Olson, Phys. Rev. Lett. **63**, 147 (1989).

[19] J. Ullrich, R. Dörner, R. E. Olson, H. Schmidt-Böcking, in: The Physics of Electronic and Atomic Collisions, Invited Papers of the ICPEAC, Vol. XVI, A. Dalgarno, R. S. Freund, P. M. Kock, M. S. Lubell, T. B. Lucatorto (Eds.) AIP, New York, 1989, p. 372.

[20] R. Dörner, J. Ullrich, O. Jagutzki, A. Gensmantel, H. Schmidt-Böcking, in: The Physics of Electronic and Atomic Collisions, W. R. MacGillivray, I. E. McCarthy and M. C. Standage Eds. (Adam Hilger, Bristol, 1991) p. 351.

[21] R. Dörner, J. Ullrich, O. Jagutzki, S. Lencinas, H. Schmidt-Böcking, R. E. Olson, Z. Phys. D **21**, 57 (1991).

[22] R. Dörner, J. Ullrich, R. E. Olson, O. Jagutzki, H. Schmidt-Böcking, Phys. Rev. A **47**, 3845 (1993).

[23] J. Ullrich, R. Dörner, S. Lencinas, O. Jagutzki, H. Schmidt-Böcking, U. Buck, Nucl. Instr. and Meth B **61**, 415 (1991).

[24] V. Frohne, S. Cheng, R. Ali, M. Raphaelian, C. L. Cocke, R. E. Olson, Phys. Rev. Lett. **71**, 696 (1993).

[25] R. Ali, V. Frohne, C. L. Cocke, M. Stockli, S. Cheng, M. L. A. Raphaelian, Phys. Rev. Lett. **69**, 2491 (1992).

[26] R. Dörner *et al.*, Nucl. Instr. and Meth. B **127**, 225 (1997).

[27] V. Mergel *et al.* Phys. Rev. Lett. **79**, 387 (1997).

[28] V. Mergel, Diploma Thesis, Johann-Wolfgang-Goethe Universität Frankfurt (1994).

[29] V. Mergel, R. Dörner, J. Ullrich, O. Jagutzki, S. Lencinas, S. Nüttgens, L. Speilbeger, M. Unverzagt, C. L. Cocke, R. E. Olson, M. Schulz, U. Buck, E. Zanger, W. Theisinger, M. Isser, S. Geis and H. Schmidt-Böcking, Phys. Rev. Lett. **74**, 2200 (1995).

[30] "Hot recoils from cold atoms," Ph.D. Thesis, Kernfysisch Versneller Instituut, Atomic Physics, Rijksuniversiteit Groningen, Zernikelaan 25, NL-9747 AA Groningen, The Netherlands. J. W. Turkstra, (2001).

[31] "Construction of a COLTRIMS spectrometer with a laser cooled target for electron transfer studies," Ph.D. Thesis, Niels Bohr Institute, Faculty of Science, University of Copenhagen, Denmark. M. van der Poel, (2001).

[32] M. van der Poel, C. V. Nielsen, M. Rybaltover, S. E. Nielsen, M. Machholm and N. Andersen, J. Phys. B: At. Mol. Opt. Phys. **35**, 4491 (2002).

[33] L. Landau, Phys. Z. Sow. **2**, 46 (1932).

[34] C. Zener, Proc. R. Soc. A **137**, 696 (1932).

[35] R. E. Olson and A. Salop, Phys. Rev. A **14**, 579 (1976).

[36] I. Y. Yurova, J. Phys. B: At. Mol. Opt. Phys. **28**, 999 (1995).

[37] E. I. Dashevskaya and E. E. Nikitin, J. Chem. Soc. Faraday Trans. **89**, 1567 (1993).

[38] I. V. Hertel, B. S. Schmidt, and E. Meyer, Phys. Prog. Rep. **48**, 375 (1985).

[39] B. H. Bransden and M. R. C. McDowell, "Charge Exchange and Theory of Ion-Atom Collisions" (1992). (The International series of monographs on Physics; 82).

[40] M. F. V. Lundsgaard, S. E. Nielsen, H. Rudolph, and J. P. Hansen, J. Phys. B: At. Mol. Opt. Phys. **31**, 3215 (1998).

[41] Yu. N. Demkov, Sov. Phys. JETP **18**, 138 (1964).

[42] W. E. Meyerhof, Phys. Rev. Lett. **31**, 1341 (1973).

[43] "Theoretical Investigation of Inelastic Process in Slow to Fast Ion-Atom Collision," Ph.D. Thesis, Department of Physics, Kansas State University, Manhattan, Kansas, USA. T. G. Lee, (2003).

[44] J. Kuang and C. D. Lin, J. Phys. B **29**, 1207 (1996).

[45] X. Flechard, H. Nguyen, E. Wells, I. Ben-Itzhak, and B. D. DePaola, Phys. Rev. Lett. **87**, 123203 (2001).

[46] M. van der Poel, C. V. Nielsen, M. -A. Gearba, and N. Andersen, Phys. Rev. Lett. **87**, 123201 (2001).

[47] J. W. Turkstra, R. Hoekstra, S. Knoop, D. Meyer, R. Morgenstern, and R. E. Olson, Phys. Rev. Lett. **87**, 123202 (2001).

[48] J. Ullrich, R. Moshammer, O. Jagutzki, V. Mergel, H. Schmidt-Böcking, and L. Spielberger, J. Phys. B: At. Mol. Opt. Phys. **30**, 2917 (1997).

[49] R. Dörner, V. Mergel, O. Jagutzki, L. Spielberger, J. Ullrich, R. Moshammer, and H. Schmidt-Böcking, Phys. Rep. **330**, 95 (2000).

[50] R. Moshammer, M. Unverzagt, W. Schmitt, J. Ullrich, and H. Schmidt-Böcking, Nucl. Instrum. Phys. Res. B **108**, 425 (1996).

[51] H. Kollmus, W. Schmitt, R. Moshammer, M. Unverzagt, and J. Ullrich, Nucl. Instrum. Phys. Res. B **124**, 377 (1997).

[52] Phrasor Scientific, 1536 Highland Ave, Duarte, CA 91010.

[53] E. Raab, M. Prentiss, A. Cable, S. Chu, and D. Pritchard, Phys. Rev. Lett. **59**, 2631 (1987).

[54] C. Wieman, G. Flowers, S. Gilbert. Am. J. Phys. **63** 4 (1995).

[55] H. Metcalf and P. van der Straten. *Cooling and Trapping of Neutral Atoms.* Springer. New York 1999.

[56] C. Townsend, Ph.D. Thesis, Merton College, Oxford (1995).

[57] M. S. Feld and V. S. Letokhov, *Laser Spectroscopy*, Sci. Am. **229**, 69 (1973).

[58] L. Ricci, M. Weidemüller, T. Esslinger, A. Hemmerich, C. Zimmermann, V. Vuletic, W. König, and T. W. Hänsch, Optics Comm. **117**, 541 (1995).

[59] New Focus, 5215 Hellyer Avenue, San Jose, CA 95138-1001.

[60] TOPTICA Photonics AG Fraunhoferstr.14 D-82152 Martinsried/Munich Germany.

[61] R. Kowalski, S. Root, S. D. Gensemer, and P. L. Gould, Rev. Sci. Instrum. **72**, 2532 (2001).

[62] For example, Neos Technologies, Inc., 4300 C Fortune Place, Melbourne, FL 32904.

[63] SAES Getters USA Inc., 1122 East Cheyenne Mountain Blvd., Colorado Springs, CO 80906.

[64] Y.-C. Chen,Y.-A. Liao, L. Hsu, and I. A. Yu, Phys. Rev. A **64**, 031401 (2001).

[65] T. P. Dinneen, C. D. Wallace, K-Y. N. Tan, and P. L. Gould, Optics Letters **17**, 1706 (1992).

[66] W. C. Wiley and I. H. McLaren, Rev. Sci. Instrum. **26**, 1150 (1955).

[67] The SIMION 3D software package was developed by D. A. Dahl, MS 2208 Idaho National Engineering and Enviromental Laboratory, P.O. Box 1625, Idaho Falls, ID 83415.

[68] Galileo Electro-Optics model 1390-2500. Galileo Electro-Optics Corp. Galileo Park, PO Box 550, Sturbridge, MA, 01566, USA.

[69] H. C. Straub, M. A. Mangan, B. G. Lindsay, K. A. Smith, and R. F. Stebbings, Rev. Sci. Intrum. **70**, 4238 (1999).

[70] Del Mar Ventures 12595 Ruette Alliante 148 San Diego, CA 92130

[71] Buckbee-Mears, 245 E. 6th Street, St. Paul, MN 55101.

[72] O. Jagutzki, V. Mergel, K. Ulmmmann-Pfelger, L. Spielberger, U. Meyer, R. Dorner, and H. Schmidt-Böcking, SPIE 98, Conf. Proceedings.

[73] XSYS/IUCF Data Acquisition Software, Indiana University Cyclotron Facility, Bloomington, IN 47405.

[74] J. Perel, R. H. Vernon and H. L. Daley, Phys. Rev. **138**, A937 (1965).

[75] C. G. Townsend, N. H. Edwards, C. J. Cooper, K. P. Zetie, and C. J. Foot, Phys. Rev. A **52**, 1423 (1995).

[76] C. E. Moore, Atomic Energy Levels, Volume I and II, (1971).

[77] C. F. Melius and W. A. Goddard III, Phys. Rev. A **10**, 1541 (1974).

[78] D. Rapp and W. E. Francis, J. Chem. Phys. **37**, 2631 (1962).

[79] G. J. Lockwood, H. F. Helbig, and E. Everhart, Phys. Rev. **132**, 2078 (1963).

[80] R. E. Olson, Phys. Rev. **187**, 153 (1969).

[81] A. Bähring, I. V. Hertel, E. Meyer, and H. Schmidt, Phys. Rev. Lett. **53**, 1433 (1984).

[82] D. Dowek *et al* J. Phys. B **35**, 2051 (2002).

[83] T. G. Lee, H. Nguyen, X. Fléchard, B. D. DePaola, and C. D. Lin, Phys. Rev. A **66**, 042701 (2002).

[84] J. Weiner, V. S. Bagnato, S. Zilio, and P. S. Julienne, Rev. Mod. Phys., **71**, 1 (1999).

[85] W. R. Anderson, J. R. Veale, and T. F. Gallagher, Phys. Rev. Lett. **80**, 249 (1998).

[86] I. Mourachko, D. Comparat, F. de Tomasi, A. Fioretti, P. Nosbaum, V. M. Akulin, and P. Pillet, Phys. Rev. Lett. **80**, 253 (1998).

[87] M. D. Lukin and A. Imamoglu, Nature **413**, 273 (2001).

[88] R. Brédy, H. Nguyen, H. Camp, X. Fléchard, and B. D. DePaola, Nucl. Instr. and Meth. B **205**, 191 (2003).

[89] T. Jahnke, *et al.*, Phys. Rev. Lett. **88**, 073002 (2002).

[90] C. J. Dedman, K. G. H. Baldwin, and M. Colla, Rev. Sci. Instrum. **72**, 4055 (2001).

[91] T.W. Hänsch and A.L. Schawlow, *Cooling of gases by laser radiation.* Opt. Commun. **13**, 68-69 (1975).

[92] J. R. Parrington, H. D. Knox, S. L. Breneman, E. M. Baum, and F. Feiner, *Chart of Nuclides and Isotopes*, General Electric Co. and KAPL, INC., **15**th ed., p. 28 (1996).

[93] K. B. MacAdam, A. Steinbach, and C. Wieman, Am. J. Phys. **60**, 1098 (1992).

[94] C. D. Wallace, T. P. Dinneen, K. N. Tan, T. T. Grove, and P. L. Gould, Phys. Rev. Lett **69**, 897 (1992).

[95] K. L. Corwin, Z. T. Lu, C. F. Hand, R. J. Epstein, and C. E. Wieman, Appl. Opt. **37**, 3295 (1995).

[96] A. S. Arnold and P. J. Manson, J. Opt. Soc. Am. B, **17**, 040497 (2000).

[97] P. D. Lett, N. Watts, C. I. Westbrook, W. D. Phillips, P. L. Gould, and H. J. Metcalf, Phys. Rev. Lett. **61**, 169 (1988).

[98] S. Chu, L. Hollberg, J. E. Bjorkholm, A. Cable, and A. Ashkin, Phys. Rev. Let. **55**, 48 (1985).

Appendix A

Acquisition Program

Data acquisition and analysis programs were written in the XSYS EVAL language [73]. The sorting program is just an expanded version of the acquisition program. Therefore, presented here is the acquisition program only. The .COM file is used to initialize and allocate memory available for data accumulation. Normally, in the .COM file included in this appendix, the listed allocations are sufficient for a typical MOTRIMS experiment. Furthermore, the TOF drift correction file is also included to help guide the sorting procedure.

A.1 Acquisition Program

```
! ********************************************************************
! ***                    MOTRIMS6.EVL                              ***
! ***      EVL FILE FOR ION-ATOM COLLISION EXPERIMENTS             ***
! ***      WITH BOTH BACKGAMMON AND RESISTIVE ANODE                ***
! ***                  H NGUYEN X. FLECHARD                        ***
! ***                   last modified May 2001                     ***
! ***                                                              ***
! ***                                                              ***
! ***                                                              ***
! motrim6.EVL
!*******************************************************************
!* EVL FILE FOR Projectile-Recoil coincidence studies *
!* Code for use with Ortec AD811 and TDC *
!* Germanium WSA for Projectile *
!* Resistive anode for Recoil ion *
!*******************************************************************
! OPTION TAPE !          ! GENERAL PURPOSE PARAMETERS
!*******************************************************************
INTEGER I1=1
INTEGER I255=255
INTEGER I511=511
INTEGER I1023=1023
INTEGER I2047=2047
INTEGER Seed=8723645          !random number seed
```

```
INTEGER INEG=-1
REAL dChannel
REAL R2=2.0
REAL temp                ! temporary variable !
!*********************************************************************
! Recoil position parameters
!*********************************************************************
REAL RX1sig              ! Recoil X1 signal
REAL RX2sig              ! Recoil X2
signal REAL RY1sig               ! Recoil Y1 signal
REAL RY2sig              ! Recoil Y2 signal
REAL RSsig               ! Recoil SUM X1 +X2 + Y1 + Y2
REAL RX1thre=25                  ! Recoil X1 threshold
REAL RX2thre=25                  ! Recoil X2 threshold
REAL RY1thre=25                  ! Recoil Y1 threshold
REAL RY2thre=25                  ! Recoil Y2 threshold
REAL RSthre=150                  ! Recoil SUM theshold
REAL RX1offse=11.3                 ! Recoil X1 offset
REAL RX2offse=9.40                 ! Recoil X2 offset
REAL RY1offse=11.8                 ! Recoil Y1 offset
REAL RY2offse=10.5                 ! Recoil Y2 offset
REAL RX1gain=0.9961                  ! Recoil X1 gain
REAL RX2gain=0.9930                  ! Recoil X2 gain
REAL RY1gain=0.9582                  ! Recoil Y1 gain
REAL RY2gain=0.9987                  ! Recoil Y2 gain
REAL RXipos              ! Recoil X intermediate position
```

```
REAL RYipos              ! Recoil Y intermediate position
INTEGER RXpos            ! Recoil X position
INTEGER RYpos            ! Recoil Y position
REAL RcosAng=1.0         ! Recoil PSD rotation angle cosinus
REAL RsinAng=0.0         ! Recoil PSD rotation angle sinus
INTEGER RXpos0=290
INTEGER RYpos0=230
!*****************************************************************
! Projectile position parameters
!*****************************************************************
REAL PXsig               ! Projectile X signal
REAL PYsig               ! Projectile Y signal
REAL PRsig               ! Projectile R signal
REAL PSsig               ! Projectile SUM X + Y + R
REAL PXthre=50           ! Projectile X threshold
REAL PYthre=50           ! Projectile Y threshold
REAL PRthre=50           ! Projectile R threshold
REAL PSthre=140          ! Projectile SUM threshold
REAL PXoffse=0           ! Projectile X offset
REAL PYoffse=0           ! Projectile Y offset
REAL PRoffse=0           ! Projectile R offset
REAL PXgain=1.0          ! Projectile X gain
REAL PYgain=1.0          ! Projectile X gain
REAL PRgain=1.0          ! Projectile X gain
REAL PRamp=2.55          ! Projectile R amplification factor(1.46*1.75)
REAL PDetScal=5          ! Scaling factor for Projectile Detectorsize
```

```
REAL PSHIFT=68.              ! Shift of x , y of Projectile detector image
REAL PXipos              ! Projectile x intermediate position
REAL PYipos              ! Projectile y intermediate position
INTEGER PXpos              ! Projectile x position
INTEGER PYpos              ! Projectile y position
REAL PcosAng=1.0              ! Projectile PSD rotation angle cosinus
REAL PsinAng=0.0              ! Projectile PSD rotation angle sinus
INTEGER PXmin=150
INTEGER PXmax=350
INTEGER PYmin=150
INTEGER PYmax=350
!
! TDC parameters !**************************************************
REAL Tsig              !TDC signal
INTEGER TIsig              ! TDC signal
INTEGER TNUM              ! number of multihits
REAL Tmin1=75000.0              ! Time window minimum
REAL Tmax1=85000.0
REAL Tmin2=7000.0              ! Time window min for refine sorting
REAL Tmax2=7255.0              ! Time window max for refine sorting
REAL TRXfact=0.21              ! Time Xpos correction
REAL TRYfact=-0.046              ! Time Ypos correction
REAL Tdrift=0              ! Time shift to correct drift
! ! Chopper parameters !*******************
Integer Tacmin=100
Integer Tacmax=200 ! !
```

```
!*********************************************************************
!* SORTING *
!*********************************************************************
OPTION ALLSPEC
! this defines the spectra and 2-d gates !
!REAL DATA IS 11 BITS.
HERE 12TH BIT IS INCLUDED FOR OVERFLOW DETECTION !
FORMAT ST1 1 24 1 LONGSIGNED
FORMAT SRIP 3 12 1
FORMAT STAC 4 12 1
FORMAT SRX1 5 12 1
FORMAT SRX2 6 12 1
FORMAT SRY1 7 12 1
FORMAT SRY2 8 12 1
FORMAT SPY 9 12 1          ! Wedge
FORMAT SPX 10 12 1          ! Strip
FORMAT SPR 11 12 1          ! Remainder !
! EVENT BEGIN TAPE ! EVENT 2 !
!*********************************************************************
!* Time of flight *
!*********************************************************************
! RAN (Seed)          ! Randomize to prevent beats
STA dChannel
GET ST1          ! Get TDC timing signal
FLOAT
ADD dChannel
```

```
STA Tsig              ! Store as real variable
IF LE Tmin1 exit              ! EXIT IF TOF TOO SMALL
IF GT Tmax1 exit              ! EXIT IF TOF TOO LARGE
! TAPE              ! RECORD ONLY IF TOF BIGGER THAN TMIN1 !
LDA Tsig
SUB Tmin1
STA Tsig
IF GE 65535.0 exit
FIX
! ******************************************************************
TINC Tspec              ! Increment full Time spectrum *
! ******************************************************************
!*****************************************************************
!* Recoil Position *
!*****************************************************************
! RAN (Seed)              ! Randomize to prevent beats
STA dChannel
GET SRX1              ! Get X1 Recoil PSD signal
FLOAT
ADD dChannel
SUB RX1offse
MUL RX1gain
IF GE I2047 EXIT              ! Exit if it is an overflow
IF LE RX1thre EXIT              ! Exit if less than lower threshold
STA RX1sig              ! Store as real variable FIX
! ******************************************************************
```

```
TINC RX1spec            !Increment RX1 spectrum *
! ******************************************************************
! RAN (Seed)            ! Randomize to prevent beats
STA dChannel
GET SRX2            ! Get X2 Recoil PSD signal
FLOAT
ADD dChannel
SUB RX2offse
MUL RX2gain
IF GE I2047 EXIT            ! Exit if it is an overflow
IF LE RX2thre EXIT            ! Exit if less than lower threshold
STA RX2sig            !Store as real variable FIX
! ********************************
TINC RX2spec            ! Increment RX2 spectrum
!********************************
! RAN (Seed)            ! Randomize toprevent beats
STA dChannel
GET SRY1            ! Get Y1 Recoil PSD signal
FLOAT
ADD dChannel
SUB RY1offse
MUL RY1gain
IF GE I2047 EXIT            ! Exit if it is an overflow
IF LE RY1thre EXIT            ! Exit if less than lower threshold
STA RY1sig            ! Store as real variable FIX
!********************************
```

```
TINC RY1spec              ! Increment RY1 spectrum *
!*******************************
! RAN (Seed)              ! Randomize to prevent beats
STA dChannel
GET SRY2 ! Get Y2 Recoil PSD signal
FLOAT
ADD dChannel
SUB RY2offse
MUL RY2gain
IF GE I2047 EXIT              ! Exit if it is an overflow
IF LE RY2thre EXIT              ! Exit if less than lower threshold
STA RY2sig              ! Store as real variable
FIX
! ********************************
TINC RY2spec              ! Increment RY2 spectrum *
! ******************************** !
LDA RX1sig
ADD RX2sig
ADD RY1sig
ADD RY2sig
IF LE RSthre EXIT              ! Exit if less than lower threshold
STA RSsig              ! Resistive anode Recoil PSD charge signal
FIX
! ********************************
TINC RSspec              ! Increment RS spectrum *
!******************************** !
```

```
!************************Position calculation****
!
IF RSsig EQ 0. EXIT                ! prevent devide by zero !
LDA RY2sig
ADD RX1sig
DIV RSsig
MUL I511
SUB I255
STA RYipos              ! Store for 11 bit position later !
LDA RY1sig
ADD RX1sig
DIV RSsig
MUL I511
SUB I255
STA RXipos              ! Store for 11 bit position later !
!*************************Rotation**************
MUL Rsinang
STA temp
LDA RXipos
MUL Rcosang
SUB temp
ADD I255
STA RXpos               ! Recoil X coordinate !
LDA RXipos
MUL Rsinang
STA temp
```

```
LDA RYipos
MUL Rcosang
ADD temp
ADD I255
STA RYpos              ! Recoil Y coordinate !
!****************************************
TINC RXpos RYpos RXYspec              ! Increment Recoil 2D position spectrum *
! ***************************************** !
!*************************************************
!* Projectile Position *
!*************************************************
!
RAN (Seed)              ! Randomize to prevent beats
STA dChannel
GET SPX              ! Get X Projectile PSD signal
FLOAT
ADD dChannel
SUB PXoffse
MUL PXgain IF GE I2047 EXIT              ! Exit if it is an overflow !
IF LE PXthre EXIT              ! Exit if less than lower threshold
STA PXsig              ! Store as real variable FIX
! ********************************
TINC PXspec              ! Increment PX spectrum *
! ********************************** !
RAN (Seed)              ! Randomize to prevent beats
STA dChannel
```

```
GET SPY              ! Get Y Projectile PSD signal
FLOAT
ADD dChannel
SUB PYoffse
MUL PYgain
IF GE I2047 EXIT              ! Exit if it is an overflow !
IF LE PYthre EXIT              ! Exit if less than lower threshold
STA PYsig              ! Store as real variable
FIX
! ********************************
TINC PYspec              ! Increment PY spectrum *
! ********************************* !
RAN (Seed)              ! Randomize to prevent beats
STA dChannel
GET SPR              ! Get R Projectile PSD signal
FLOAT
ADD dChannel
SUB PRoffse
MUL PRgain
IF GE I2047 EXIT              ! Exit if it is an overflow !
IF LE PRthre EXIT              ! Exit if less than lower threshold
STA PRsig              ! Store as real variable
FIX
! ********************************
TINC PRspec              ! Increment PR spectrum *
! ********************************* !
```

```
LDA PRsig
MUL PRamp
ADD PXsig
ADD PYsig !
IF LE PSthre EXIT              ! Exit if less than lower threshold
STA PSsig              ! Resistive anode Recoil PSD charge signal
FIX
! ********************************
TINC PSspec              ! Increment PS spectrum *
! ********************************* !
!*****************Position calculation******************!
IF PSsig EQ 0. EXIT              ! prevent devide by zero !
LDA PXsig
DIV PSsig
MUL I511
SUB PSHIFT              ! Shift detector image
MUL PDetScal              ! Detector scaling factor
SUB I255
STA PXipos              ! Store for 11 bit position later !
LDA PYsig
DIV PSsig
MUL I511
SUB PSHIFT              ! Shift detector image
MUL PDetScal              ! Detector scaling factor
SUB I255
STA PYipos              ! Store for 11 bit position later !
```

```
!*******************Rotation****************************
MUL Psinang
STA temp
LDA PXipos
MUL Pcosang
SUB temp
ADD I255
STA PXpos              ! Projectile X coordinate !
LDA PXipos
MUL Psinang
STA temp
LDA PYipos
MUL Pcosang
ADD temp
ADD I255
STA PYpos              ! Projectile Y coordinate !
! ****************************************
TINC PXpos PYpos PXYspec              ! Increment Proj. 2D position spectrum *
! ****************************************** !
!*********************************************
! !
IF PXpos GT PXmax EXIT              ! EXIT if not in Projectile window !
IF PXpos LE PXmin EXIT              ! EXIT if not in Projectile window !
IF PYpos GT PYmax EXIT              ! EXIT if not in Projectile window !
IF PYpos LE PYmin EXIT              ! EXIT if not in Projectile window !
! LDA Tsig
```

```
IF GT Tmax2 EXIT              ! Exit if not in time window
IF LE Tmin2 EXIT              ! Exit if not in time window
SUB Tmin2
SUB Tdrift
STA Tsig
! ******************************************
TINC PXpos RXpos PXRXspec       ! Increment Recoil/proj.X position spectrum*
! ******************************************
! ******************************************
TINC PYpos RYpos PYRYspec       ! Increment Recoil/proj.Y position spectrum*
! ******************************************
! ****************************************
TINC Tsig RXpos TRXspec       ! Increment Time/Rec.X position spectrum*
! ****************************************
LDA RXpos
SUB RXpos0
MUL TRXfact
ADD Tsig
STA Tsig !
LDA RYpos
SUB RYpos0
MUL TRYfact
ADD Tsig
STA Tsig !
! ************************************************
TINC Tsig RXpos TRXspec2       ! Increment correct Time/Rec.X position spectrum*
```

```
! ********************************************** ! !
! ****************************************
TINC Tsig RYpos TRYspec        ! Increment Time/Rec.Y position spectrum*
! ****************************************
! ****************************************
TINC Tsig Tspec2        ! Increment corrected Time spectrum*
! **************************************** !
GET SRIP
FLOAT DIV 8.0
FIX
STA SRIP
! ****************************************
TINC RIPLspec        ! Increment ripple spectrum *
! **************************************** !
****************************************
Tinc Tsig
SRIP TRIPspec        ! Increment Time/ripple spectrum *
! ****************************************
GET STAC
MUL 0.25
sta STAC
! ******************************
TINC STAC TACspec        ! Increment TAC spectrum *
! ****************************** ! ! **********************************
TINC Tsig STAC TTACspec        ! Increment Time/TAC spectrum *
! **********************************
```

```
IF STAC LE TACmax THEN
IF STAC GE TACmin THEN
! ********************************
TINC Tsig TspecCF        ! Increment Time spectrum CH OFF*
! ********************************
TDEC Tsig TspecDF        ! DecremenT Time spectrum CH DIF*
! ********************************
else
! ********************************
TINC Tsig TspecCN        ! IncremenT Time spectrum CH ON *
! ********************************
TINC Tsig TspecDF        ! IncremenT Time spectrum CH DIF*
! ********************************
ENDIF
ENDIF
!
! ****************************************
TINC RXpos RYpos RXYspec2        ! Increment Recoil X Y position spectrum*
! ****************************************
TINC RXpos RXspec        ! Increment X pos *
! ****************************************
TINC RYpos RYspec        ! Increment Y pos *
! ****************************************
END
```

A.2 MOTRIM6.com file

DMEM	ALL GLOBAL FILE	
AMEM	NEW 22000 PAGES*	
AMEM	1	Tspec 65536
AMEM	2	TspecCN 256
AMEM	3	TspecCF 256
AMEM	4	TspecDF 256
AMEM	5	Tspec2 256
AMEM	6	CHOPspe 2048
AMEM	7	TNUMspec 4
AMEM	8	TRONspe 512
AMEM	9	TROFFspe 512
AMEM	10	RX1spec 2048
AMEM	11	RX2spec 2048
AMEM	12	RY1spec 2048
AMEM	13	RY2spec 2048
AMEM	14	RSspec 8192
AMEM	15	RXYspec 512 512
AMEM	20	PXspec 2048
AMEM	21	PYspec 2048
AMEM	22	PRspec 2048
AMEM	23	PSspec 8192
AMEM	25	PXYspec 512 512
AMEM	30	TRXspec 256 512
AMEM	35	TRYspec 256 512
AMEM	40	RXYspec2 512 512
AMEM	41	RXspec 512
AMEM	42	RYspec 512
AMEM	45	PXRXspec 512 512
AMEM	46	PYRYspec 512 512
AMEM	50	TRXspec2 256 512
AMEM	51	Proj1 512
AMEM	52	Proj2 512
AMEM	53	Proj3 512
AMEM	54	Proj4 512
AMEM	55	TVtspec 256 256
AMEM	60	VXVYspec 512 512
AMEM	65	TTROspec 256 512
AMEM	70	TTRFspec 256 512
CLEARFLAGS	CLEAR ALL	

A.3 Time of Flight Drifts

Typically, when running and experiment with high resolution in Q value, TOF drifts become **VERY** important. These drifts are due to several sources. The applied pushing voltage changing by a few tens of a volts could cause a drift equivalent to a few 10^{-9} seconds. MOT position could also slightly deviate within the trapping region, causing a change of distance between recoil ion origin to the recoil ion detector. To prevent a blurring of timescale due to these, runs of 5 or 10 minutes are required. The following command file will reread the runs with appropriate parameters associated with each run.

```
!Always start with a dollar sign. A ! indicates a comment line
TPE VAR Tmax1=
TPE VAR Tmin1=
TPE VAR Tmax2=
TPE VAR Tmin2=
TPE VAR Tmax3=
TPE VAR Tmin3=
TPE VAR Trxpos0=
TPE VAR Trypos0=
TPE VAR Trxfact=
TPE VAR Tryfact=
TPE VAR Tdrift=
TPE NEXT DATA:[MOT7]MOTRIMS100.EVT
TPE BEGIN WAIT
TPE VAR Tdrift=
TPE NEXT DATA:[MOT7]NEXTDATA.EVT
```

TPE BEGIN WAIT

WRT HAIDATA ALL

EXIT

Appendix B

Simulations

SIMION [67] simulations show that time of flight (TOF) and position focusing are simultaneously achieved in a plane placed 1024 mm from the collision region using a ratio $V_P/V_f = 1.42$ as shown in Fig. B.1. With the detector in this focal plane, a $^{87}Rb^+$ recoil ion created in the collision region with initial momentum components P_{R_x}, P_{R_y}, and P_{R_z} will have flight times (in μs) given by:

$$T = T_0 - 3.45\frac{P_{R_z}}{V_P}, \tag{B.1}$$

with

$$T_0 = 876.4V_P - 0.5. \tag{B.2}$$

Here, P_{R_z} is in atomic units and V_P is in Volts. The simulated TOF is shown in Fig. B.2 as a function of $P_{R_\parallel}$.

The ions will be detected on the PSD at coordinates (in mm) given by:

$$x = x_0 + 13.00P_{R_x}V_P - 0.5 \tag{B.3}$$

$$y = y_0 + 13.00P_{R_y}V_P - 0.5, \tag{B.4}$$

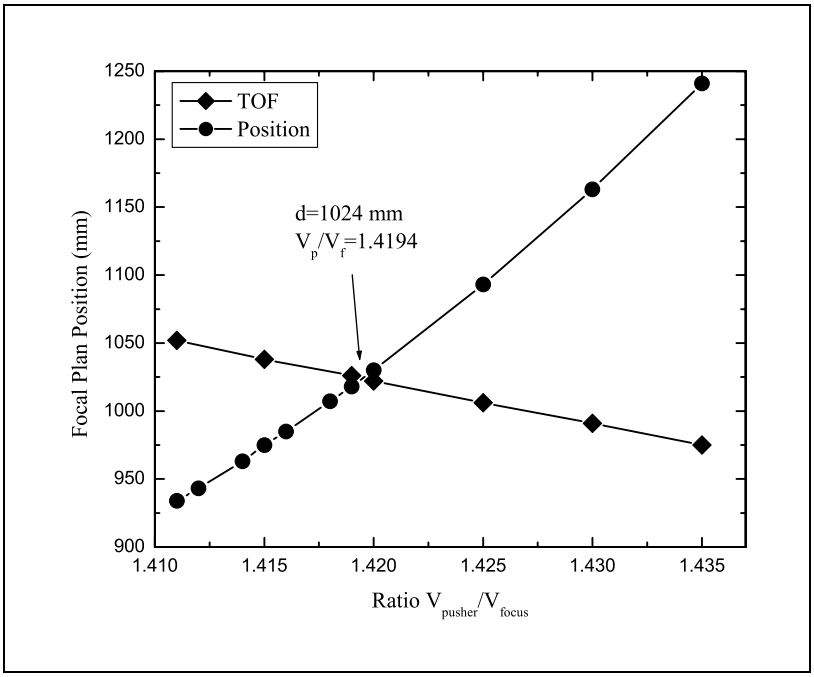

Figure B.1: *Simulation for focal plane position.*

where x_0 and y_0 indicate the center of the PSD. The simulation of both x and y positions as a function of $P_{R_\perp}$ are shown in Figs. B.3 and B.4.

Then, if one can neglect the effect of the thermal motion of the target (as the MOT allows one to do here) the resolution limitations of the system are simply given by the size of the PSD (diameter=101.6 mm), its spatial resolution ($\Delta x = \Delta y = 0.25$ mm) and the TOF measurement resolution ($\Delta T = 2$ ns). A 4π steradian detection angle is achieved for a pusher voltage, V_P, and ions having maximum recoil momenta, $P_{R_{max}}$, such that:

$$P_{R_{max}} = 1.54\sqrt{V_p}. \tag{B.5}$$

The resolution of the different momentum components can be expressed as

$$\Delta P_{R_z} = 0.29 \Delta T V_P, \tag{B.6}$$

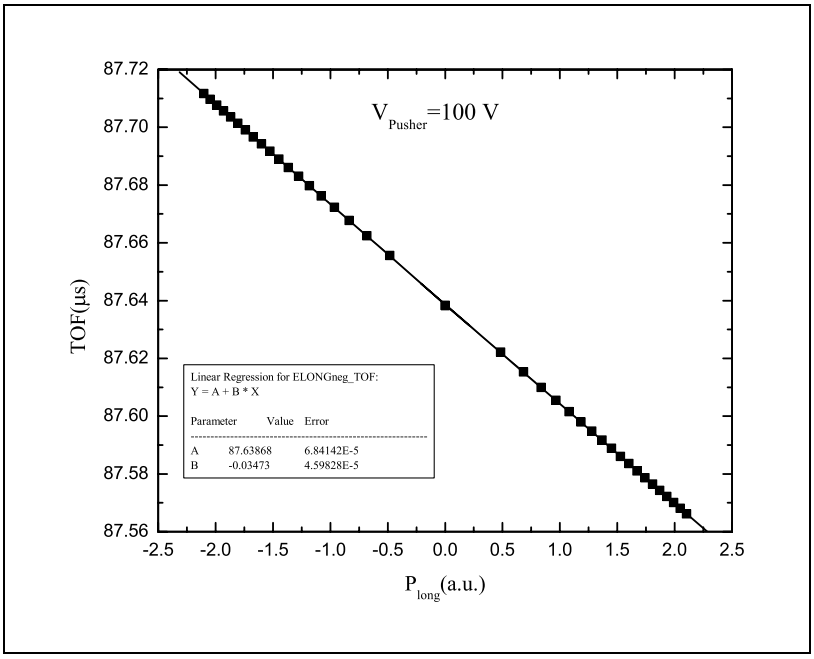

Figure B.2: *Simulation for TOF vs.* $P_{R_{\|}}$.

$$\Delta P_{R_{x,y}} = 0.077\Delta x, y\sqrt{V_P}. \tag{B.7}$$

With the TOF and PSD spatial resolution of the apparatus described here, these become

$$\Delta P_{R_z} = 0.58 \times 10^{-3} V_p \tag{B.8}$$

$$\Delta P_{R_{x,y}} = 0.19 \times 10^{-3}\sqrt{V_P}. \tag{B.9}$$

Expressions B.2, B.3, and B.4 show that one can trade resolution for detection solid angle through the value of V_P. For the collision systems discussed in this paper $P_{R_{max}}$ is always below 7.5 a.u., which implies a 4π steradian detection solid angle for $V_P \geq 25$ Volts. However, for such a low voltage the mean TOF, T_0, is rather large and limits the coincidence count rate. In addition, at some point the energy of the recoil ions becomes so low that loss of resolution due to stray electric or magnetic fields

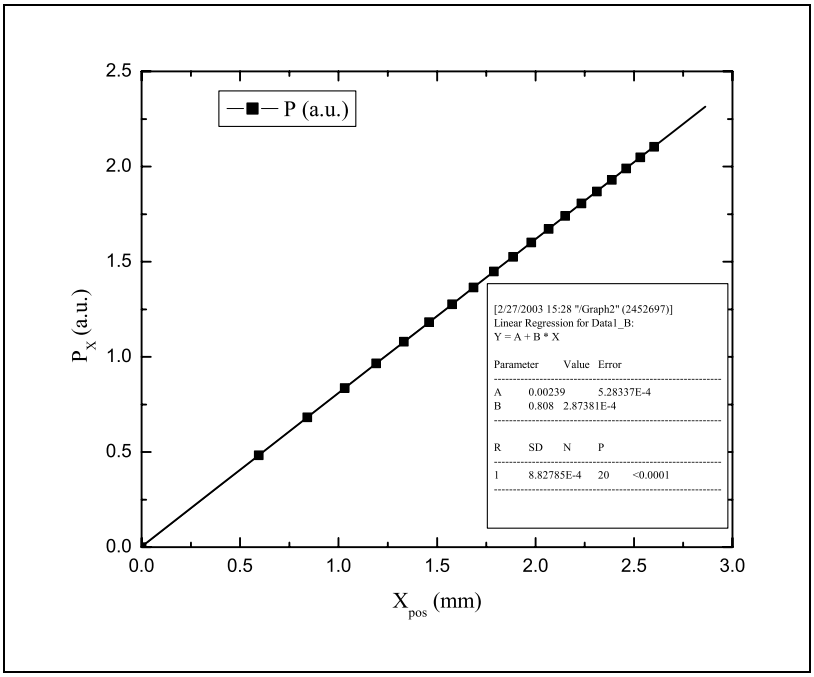

Figure B.3: *Simulation for $P_{R_\perp}$ vs. X position.*

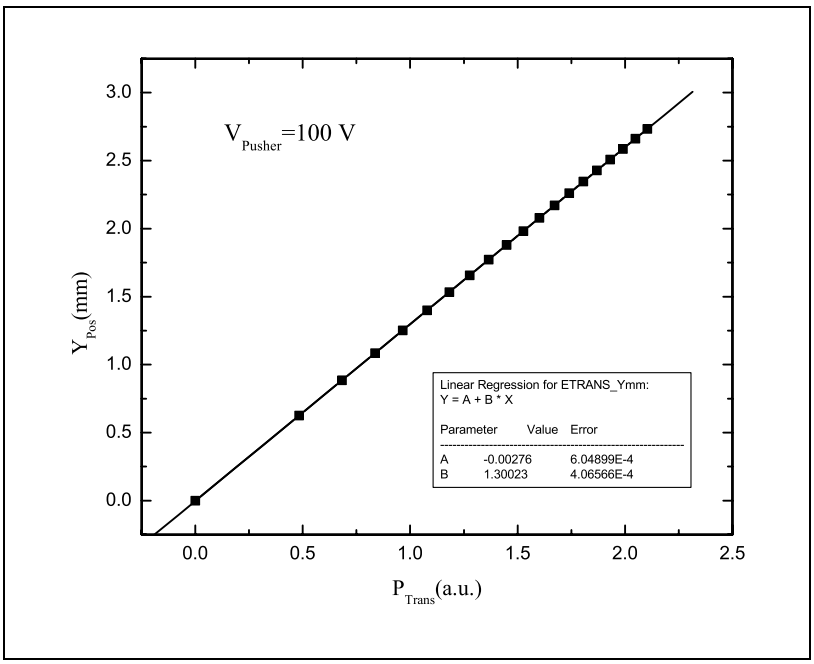

Figure B.4: *Simulation for $P_{R_\perp}$ vs. Y position.*

becomes significant. Therefore, we typically use $V_P = 100$ Volts or $V_P = 50$ Volts, leading respectively to the values $\Delta P_{R_z} = 0.06$ a.u., $\Delta P_{R_{x,y}} = 0.19$ a.u., $T_0 = 88\mu$s at 100 Volts, and $\Delta P_{R_z} = 0.03$ a.u., $\Delta P_{R_{x,y}} = 0.13$ a.u., and $T_0 = 124\mu$s. These resolutions indicate that the component for which maximum resolution is desired must be oriented along the spectrometer axis. In order to get the best resolution on the longitudinal component of the recoil ion momentum $P_{R_\perp}$, and therefore in Q-value, a quasi-longitudinal extraction geometry was chosen for this setup: the projectile ion beam enters the spectrometer *via* a 0.5 mm diameter aperture in the pusher and intersects the target at a small (3.5^o) angle with respect to the spectrometer axis in the horizontal plane. For this configuration the following expressions for the longitudinal and transverse components of the recoil momenta, with their resolutions are:

$$P_{R_\parallel} = \cos 3.5^\circ P_{R_z} - \sin 3.5^\circ P_{R_x}, \tag{B.10}$$

$$\Delta P_{R_\parallel} = 0.998 \Delta P_{R_z} + 0.061 \Delta P_{R_x} \simeq \Delta P_{R_z}, \tag{B.11}$$

$$P_{R_\perp} = \sqrt{(0.061 P_{R_z} + 0.998 P_{R_x})^2 + P_{R_y}^2}, \tag{B.12}$$

$$\Delta P_{R_\perp} \simeq \Delta P_{R_{x,y}}. \tag{B.13}$$

The recoil ion TOF is obtained by measuring the time between the detection of a recoil ion, and a once-less-charged projectile the recoil ion. Consequently, the projectile beam energy spread (of the order of 1 eV out of $\sim$ 6 keV) is of primary importance and is thus far what limits the TOF resolution. Another limitation to resolution is that the spatial and temporal focussing described above is not perfect. The optimum trade-off between spatial and TOF resolution can be found by slightly

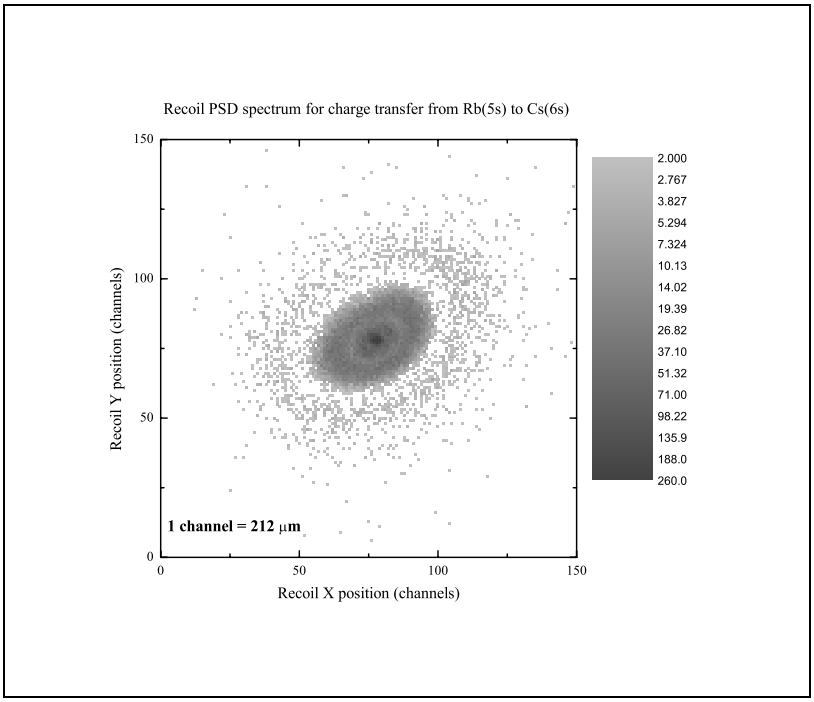

Figure B.5: *Raw recoil ion image.*

changing the time focusing conditions without noticeably affecting the spatial focusing. Operationally, for fixed V_P, the value of V_f is adjusted, minimizing the width of the peaks observed in the Q-value spectra.

Even if the trapping magnetic field B(x,y,z) is rather small (the maximum of the B-field on the recoil ions trajectory is about 100 Gauss), it still affects the trajectories of very slow recoil ions. Figure B.5 shows that the image of actual recoil ion impacts on the PSD is a tilted ellipse pattern instead of the expected circular pattern. This distortion is due to the B-field effect in this quasi-longitudinal extraction configuration.

Since the geometry of the B field is not perfectly known, an exact simulation of its effect could not be done. However, Fig. B.6 shows an estimate of the distortion using an idealized B-field geometry. Consistent with experiment, the calculation predicts a tilted ellipse pattern. Furthermore, it shows that the mean radius of

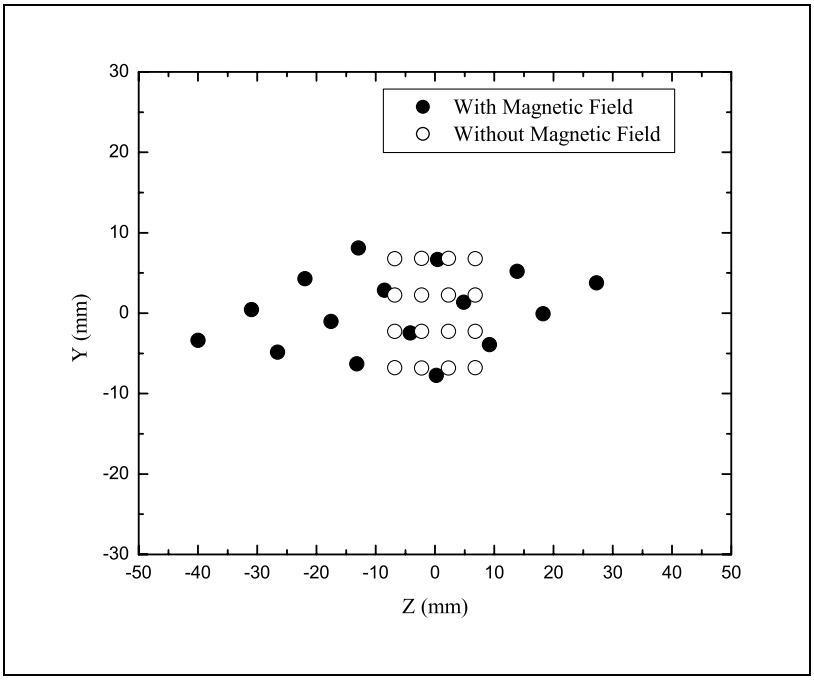

Figure B.6: *Simion magnetic field distortion effect.*

the ellipse is equal to the radius of the circle expected without any B-field effect. For the experiments discussed in this dissertation, the distortion due to the B-field was corrected in software, under the assumption that this is a consistent effect. An example of corrected position data is shown in Fig. B.7. Because of the imperfections in this correction method, a small degradation exists in the measurement's resolution. Other simulations showed that for large values of $P_{R_\perp}$, the resolution of $P_{R_\parallel}$ is also slightly affected. This was not the case for the experiments discussed here in which $P_{R_{max}}$ is always less than 7.5 a.u. If higher resolution is required in the transverse dimension, the B-field can be switched on and off with a period of a few hundreds of microseconds [90], totally eliminating this source of uncertainty.

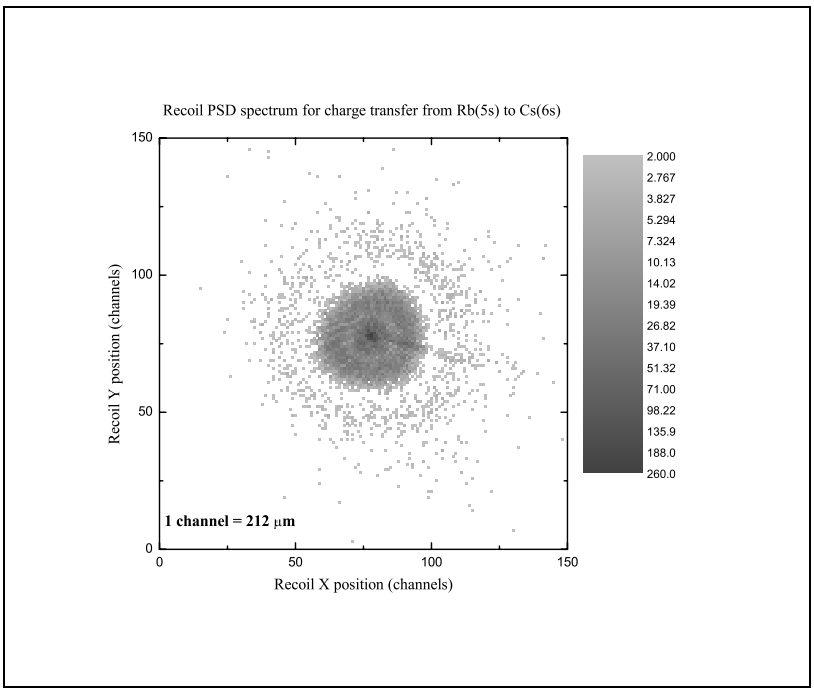

Figure B.7: *Corrected recoil ion image.*

Appendix C

Detectors

The choice of detectors used in this experiment was determined by the availability of anodes. A resistive anode was used for the detection of recoil ions and a backgammon anode for the projectiles. The detector arrangements are the same as described by Straub [69]. Here, principle of operation as well as the detector assembly and measured characteristics detectors are discussed.

C.1 Recoil Ion Detector

A resistive anode two dimensional position sensitive detector was used to measure the x,y coordinates as well as time of arrival of the recoil ions. A picture of the recoil ion detector is shown in Fig. C.1. More detailed schematics of the assembly are shown in Figs. C.2 and C.3.

C.1.1 Principle of Operation

A Z-stack configuration of micro channel plates (MCP) was employed for the recoil ion detector. When a charged particle impacts onto the first MCP, secondary electrons are emitted from its back side. This first generation electron cluster continues on to impact upon the second MCP and daughter a electron cluster is generated. Again, this daughter electron cluster arrives at the third MCP to generate a granddaughter

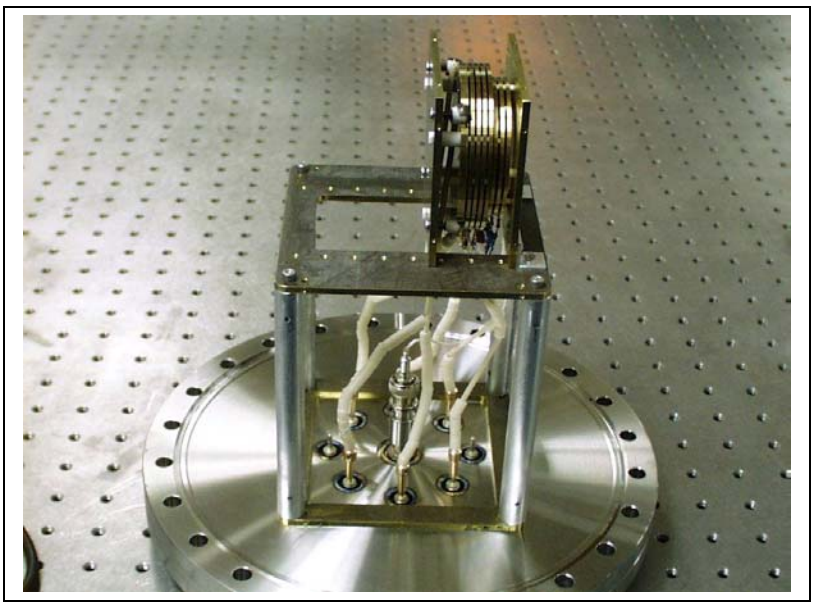

Figure C.1: *Photo of recoil ion detector.*

electron cluster. The average gain for the three consecutive channel plates is in the order of 10^7 under normal voltages applied to the plates. The granddaughter electron cluster hits the anode and acts like a current source which directly flows out of each of the anode's four corners. These currents are labelled as I_1, I_2, I_3, I_4 from each corner, respectively. An artist depiction of the resistive anode is shown in Fig. C.4.

The two dimensional position is given by the following equations:

$$x = \frac{I_1 + I_2}{I_1 + I_2 + I_3 + I_4} \tag{C.1}$$

$$y = \frac{I_1 + I_4}{I_1 + I_2 + I_3 + I_4} \tag{C.2}$$

C.1.2 Efficiency

It is desirable that the ion detection efficiency for a charged particle hitting the detector is independent of the location of the ion hit. However, due to the manufacturing processes, the channel plates might have position dependent conversion gains and thickness of resistive layer (in the case of the resistive anode detector). Other vari-

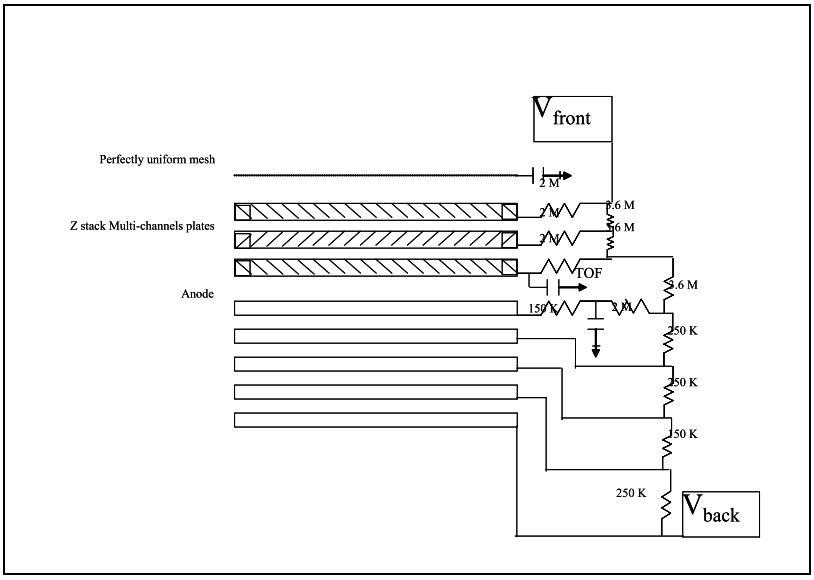

Figure C.2: *Recoil ion detector assembly.*

ables which can influence the detection efficiency include the species of the impacting particle, the angle of impact and the flux. These factors must be taken into account when measuring the relative efficiency of a detector.

C.1.3 Resolution Calibration

To test the position resolution of the detector, a mask was used. An image of the mask is shown in Fig. C.5. From measured values for the hole sizes, the distance between the mask and the anode, and from the measured ion position, we can deduce the resolution. Also, the conversion from position to channel number can be measured. For the resistive anode used,

$$1\ channel = 106\mu m \tag{C.3}$$

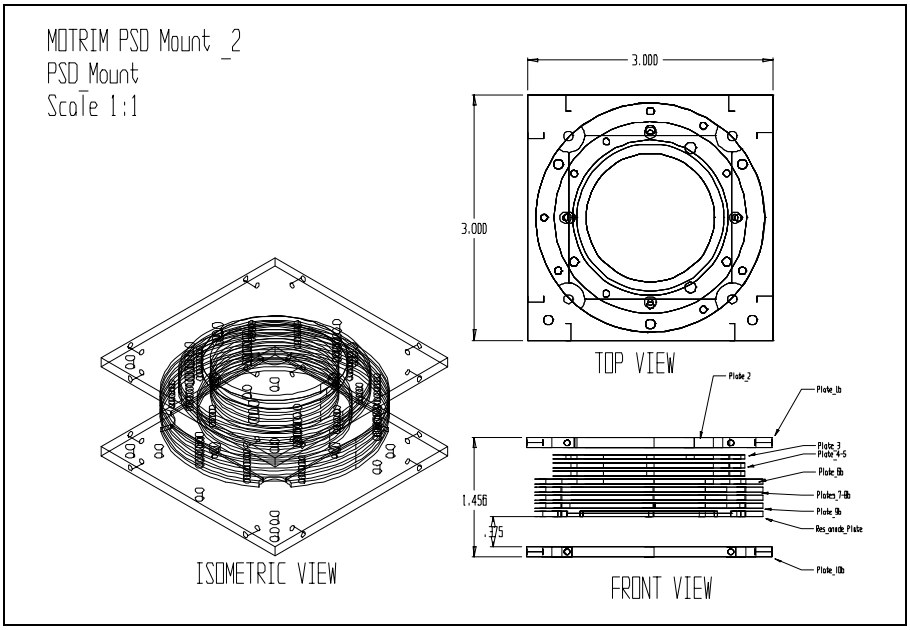

Figure C.3: *Detector mounting scheme.*

C.2 Projectile Detector

A different type of position sensitive detector was used for detecting neutral projectile particles. The backgammon anode may be thought of as a sheet of copper divided into three differently shaped and electrically isolated regions, X, Y, R. The X region is composed of a series of strips with equal horizontal spacing. The widths of these strips increase by a discrete value along the horizontal side. For the ith strip, the width w_i can be expressed as follow.

$$w_i = w_o + (i-1)\delta x \tag{C.4}$$

where w_o is the width of the first strip, and δx is the incremental value. The Y region is composed of a series of equally spaced identical wedges. Vertically from top to bottom, the width of the wedge is diminishing. For the distance of y from the top the width can be expressed as

$$w_y = w_{yo} - \alpha y \ , \tag{C.5}$$

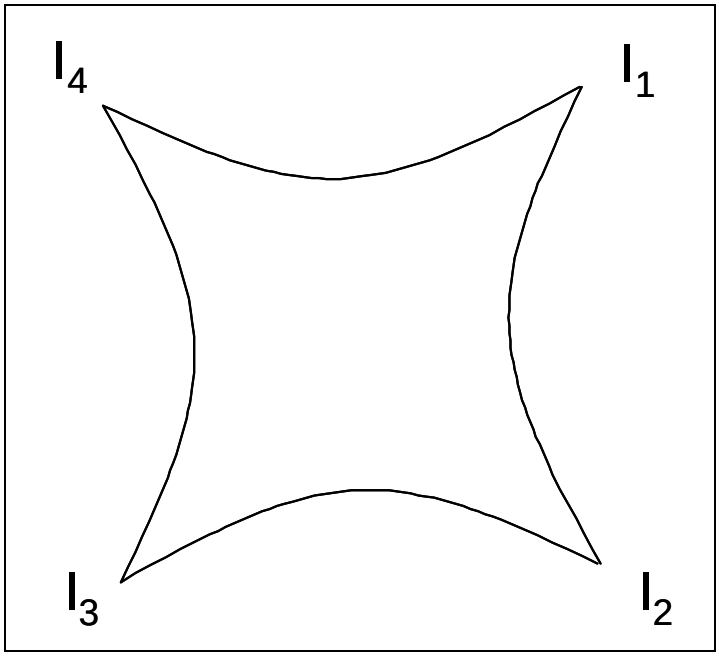

Figure C.4: *Resistive anode.*

where w_{yo} is the width on the top, and α is the slope of the wedge. The remaining area not belonging to regions X or Y is the region R.

C.2.1 Principles of Operations

A Z-stack configuration of MCPs was also employed for the projectile detector. The circular electron cluster delivers a certain amount of current to the anode. The current to each region X, Y, R is proportional to that region's surface area. By normalizing the charge from the region X or the region Y to the total charge received, the x and y position information is obtained:

$$x \propto \frac{I_X}{I_X + I_Y + I_R}, \tag{C.6}$$

$$y \propto \frac{I_Y}{I_X + I_Y + I_R}. \tag{C.7}$$

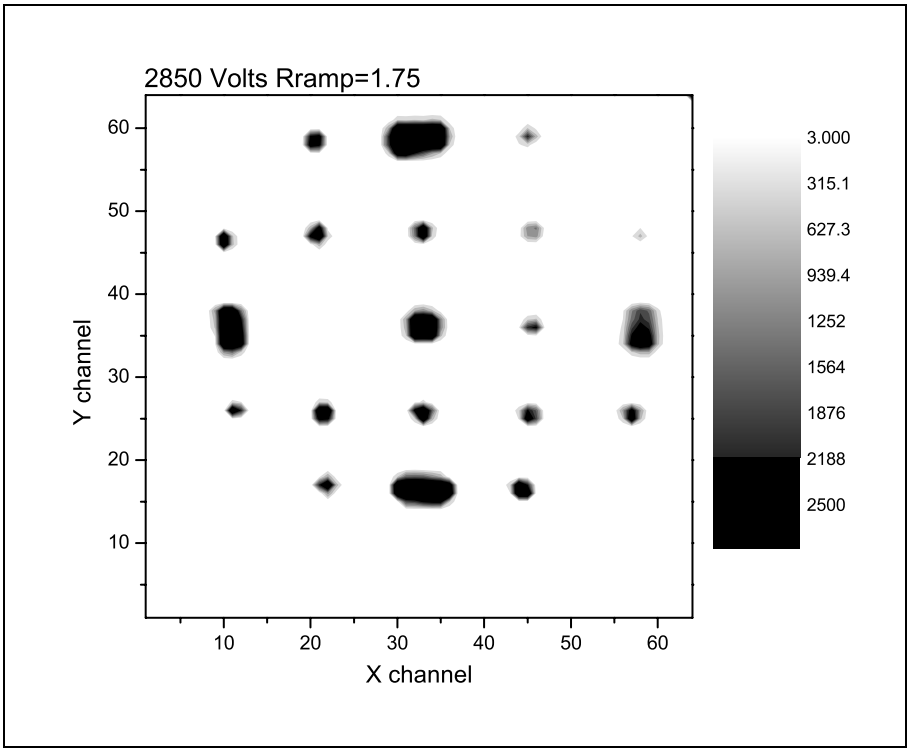

Figure C.5: *Image of the mask used to calibrate the detector.*

Appendix D

Rubidium Magneto Optical Trap

Detailed descriptions of the principles by which magneto optical trap operates are very extensive in the literature [54, 55, 91]. Within the framework of this dissertation, the target density, excited state fraction and temperature are the most important MOT characteristics. Presented here are details of rubidium atomic structure as well as the experimental methods and measurement techniques used to cool, trap, and analyze the target. To begin, examination of the rubidium fundamental properties are appropriate. This section is then followed by an explanation of the trapping and cooling mechanisms. The methods for measuring MOT characteristics are then reviewed.

D.1 Rubidium Atom

According to [92], the natural abundances, nuclear spins and masses for the two dominant rubidium isotopes are

	Relative Abundance	Nuclear Spin I	Mass a.u.
^{85}Rb	72.16	$\frac{5}{2}$	85.912
^{87}Rb	27.84	$\frac{3}{2}$	86.909

Table D.1: *Rubidium isotope natural abundances, nuclear spins, and masses.*

D.1.1 Doppler-free Saturated Absorption Spectroscopy

Doppler-free saturated absorption spectroscopy is one of the many standard techniques spectroscopists used to study atomic structure [93]. Saturated absorption spectroscopy is able to resolve the hyperfine transitions in rubidium. Using this technique to lock a laser gives good frequency stability but has some drawbacks; mainly, it has a small locking range (a few Mega-hertz). In a glass cell, Rubidium atoms are moving with a Maxwell-Boltzmann distribution

$$P(v_x) \propto e^{-\frac{mv_x^2}{2k_\beta T}}. \tag{D.1}$$

The atoms having atomic transition frequency ν_t and a velocity

$$v_x = \left(\frac{\nu_t}{\nu_L} - 1\right) \tag{D.2}$$

will interact with laser light of frequency ν_L because of the Doppler shift, given by

$$\nu' = \nu_L \left(1 + \frac{v_x}{c}\right) \tag{D.3}$$

By scanning the laser frequency across the transition and observing the absorption signal, a Doppler broadened spectrum can be seen as in Fig. D.1, since the laser light interacts with all atoms having all velocities in its path. This is referred to as the reference spectrum.

However, this would not allow hyperfine structure of rubidium atoms to be seen. We need to be able to resolve the hyperfine structure of rubidium in order to lock our lasers to a particular hyperfine transition for cooling and trapping. The trapping levels for ^{87}Rb are shown in Fig. D.2.

To see the hyperfine structure of rubidium, a setup as in Fig. D.3 is required. This is the pump-probe configuration. The pump and probe beams counter propagate and were aligned to maximize overlapping within rubidium cell. Because the beams are

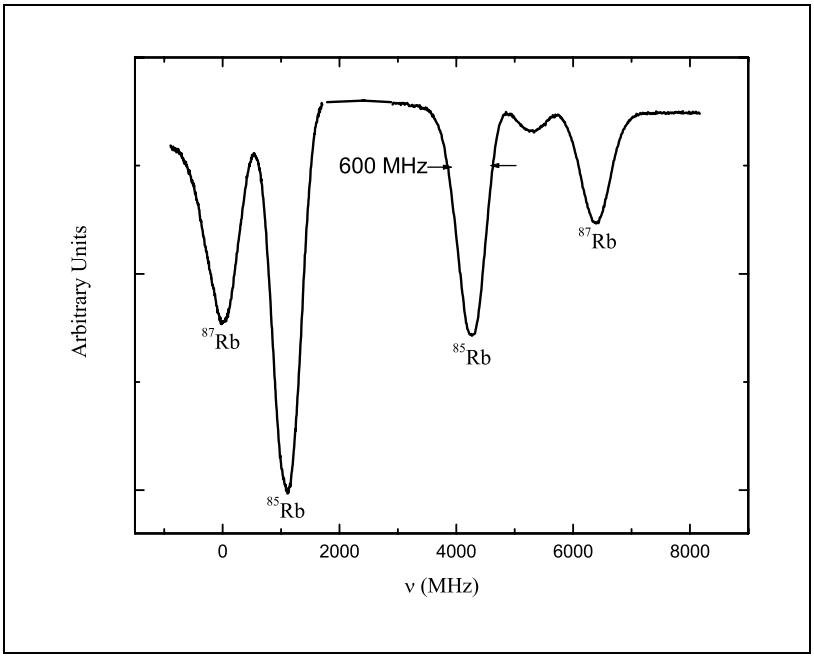

Figure D.1: *Doppler broadened spectrum.*

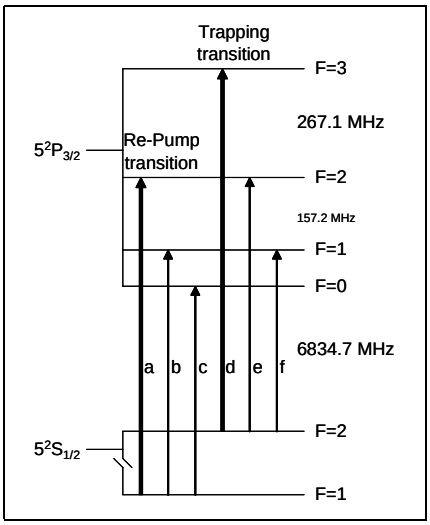

Figure D.2: ^{87}*Rb trapping levels*

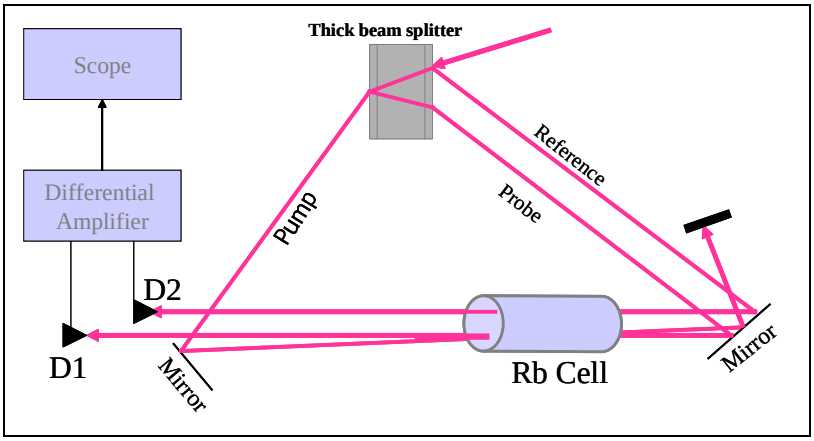

Figure D.3: *Optics setup for saturated absorption spectroscopy.*

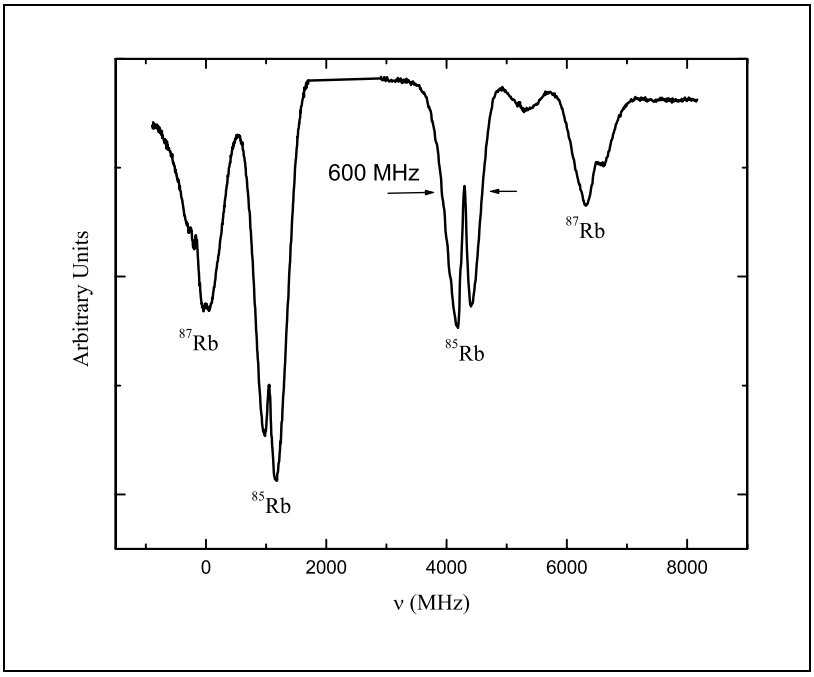

Figure D.4: *The probe beam absorption spectrum.*

counter propagating, only a narrow class of atoms with velocity around $v_x = 0$ will interact with both beams. Notice also that the intensity of the pump, being higher than the intensity of the probe, will saturate the transition and leave less atoms in the ground state to absorb the probe light. The probe beam absorption is shown in Fig. D.4.

When the absorptions of the probe beam and the reference beam are compared using the circuit shown in Fig. D.5, the Doppler-free hyperfine spectrum of rubidium is revealed. However, even though the natural abundance of ^{85}Rb is higher than that of ^{87}Rb, on the Doppler-free saturated absorption spectrum for ^{85}Rb is not as clearly resolved as ^{87}Rb, and therefore, locking lasers to the ^{85}Rb trapping lines is more challenging. Moreover, it has been shown [94] that trap loss due to inelastic collisions involving excited atoms exhibits strong isotopic dependence. Namely, the loss rate for ^{85}Rb is 3.3 times that of ^{87}Rb. This leads to a thinner target for collisions and therefore reduced count rates. It is therefore better to cool and trap ^{87}Rb for the applications presented in this dissertation.

Focusing the attention on the D2 transition for ^{87}Rb as in Fig. D.2, the Doppler-free saturated absorption spectrum is shown in Fig. D.6. The top panel shows the Doppler-free spectrum for the repump and the bottom panel shows the Doppler-free spectrum for the trapping.

D.1.2 Laser Locking

There exist a few laser locking schemes. In this work, the Dichroic Atomic Vapor Laser Lock [DAVLL] scheme was employed to lock both the master and the re-pump lasers [95]. A schematic of the DAVLL setup is shown in Fig. D.7. DAVLL requires no more than a mW of laser power. The magnetic field of roughly 80 Gauss is provided by a set of hollowed out magnetic plates. The direction of the field is parallel to the $\overrightarrow{k}$ vector of the laser beam. The Zeeman shift induced by this permanent magnetic field is 1.4 MHz/Gauss. Because of this shift, the absorption frequencies for σ^+ and σ^- components of linearly polarized light are different as shown in Fig. D.8. The quarter wave plate along with the beam splitter separate the left and right circularly polarized light exiting the cell. The difference between these two signals is used to

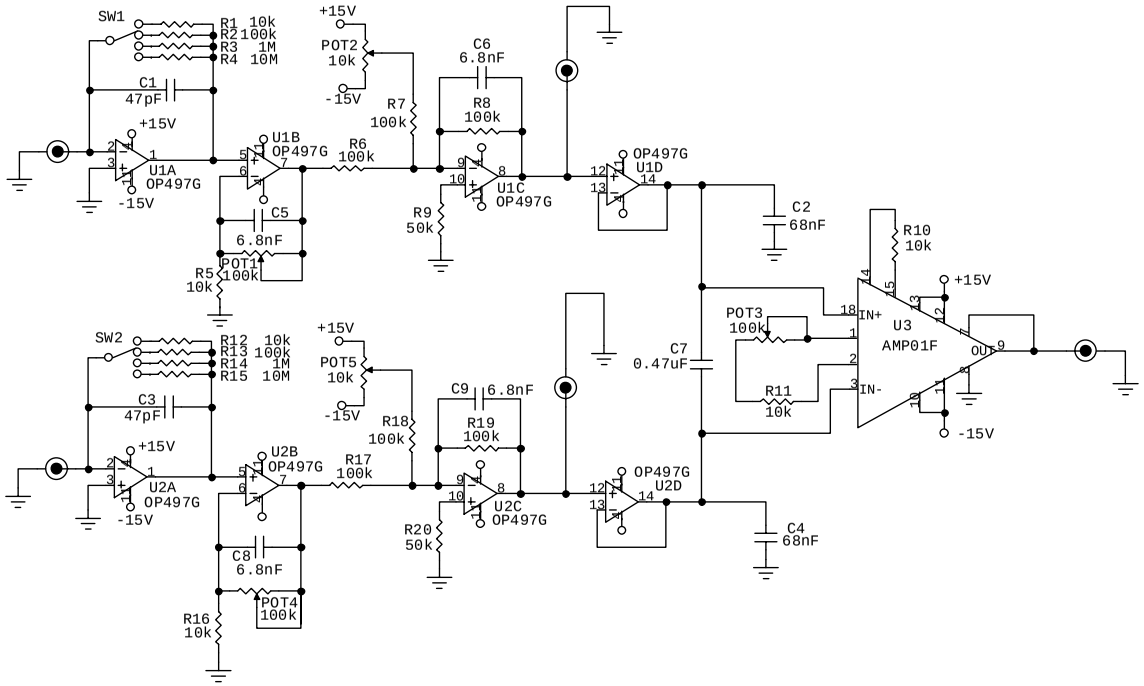

Figure D.5: Circuit electronics to take the difference of two signals.

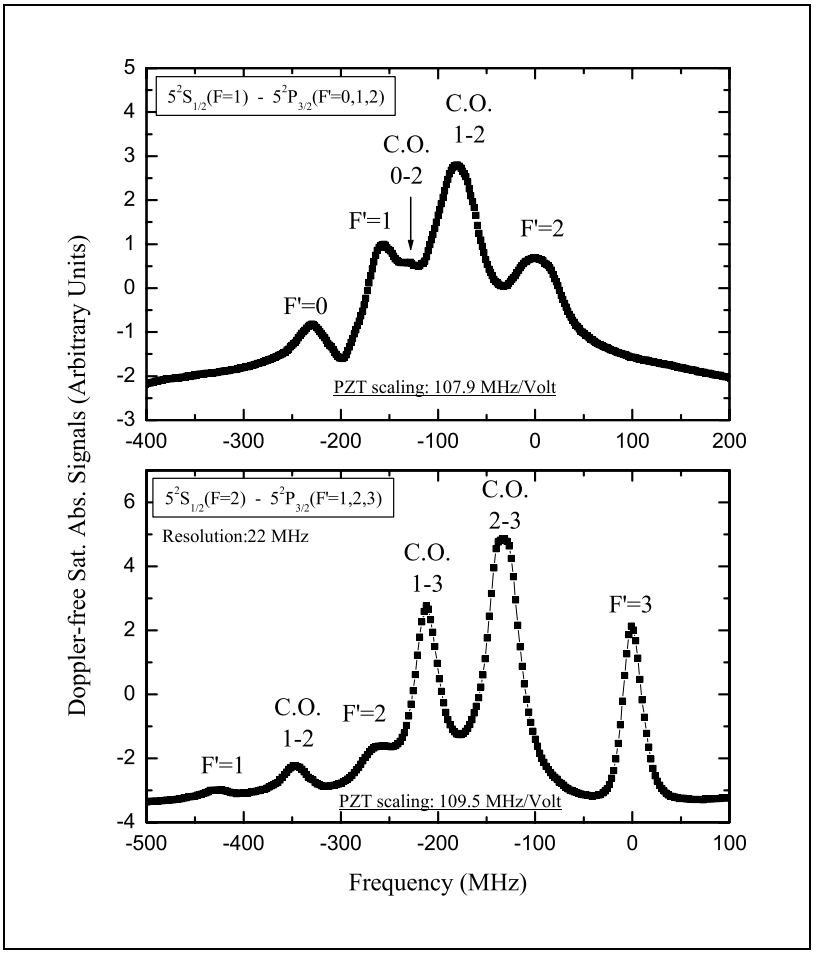

Figure D.6: *Doppler free saturated absorption.*

generate the feedback to the laser controller. The locking point then can be adjusted to the desired frequency by adding a direct voltage offset to the feedback signal using the circuit in Fig. D.9.

The advantage of DAVLL is its relatively wide range of tuning($\sim$ 500MHz). DAVLL seems to perform well due to its robustness even in the acoustically hostile environment of J. R. Macdonald Laboratory. However, absolute laser frequency is compromised since we do not know exactly where the lock set point is, as compared to peak locking where one would know exactly the lock point is. Also, the temperature dependence of the natural dichroism of the cell windows causes the lock set point

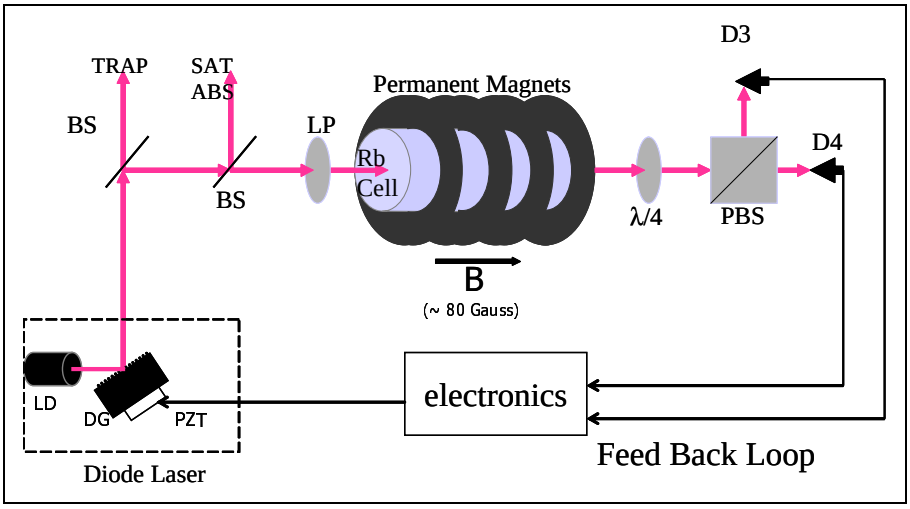

Figure D.7: *Dichroic atomic vapor laser lock setup.*

to drift as the laboratory temperature changes.

D.2 Rubidium MOT Characteristics

Using a MOT as a target for ion-atom collision experiments requires some knowledge of the MOT characteristics. Particularly, one wishes to know the approximate target temperature, the density, and the excited state fraction. In-depth theoretical understandings of the characteristics of magneto optical traps are available [96]. Experimentally, a few methods of obtaining the basic MOT characteristics were used to determine MOT characteristics in MOTRIMS setup.

D.2.1 Measuring MOT Temperature

The "temperature" can be defined as a parameter of a state of a closed system in thermal equilibrium with its surroundings. This is not the case in a MOT. We simply treat the MOT as a collection of atoms having Maxwell-Boltzman distribution of velocities.

There are several methods which give the temperature of the MOT [97]. The first

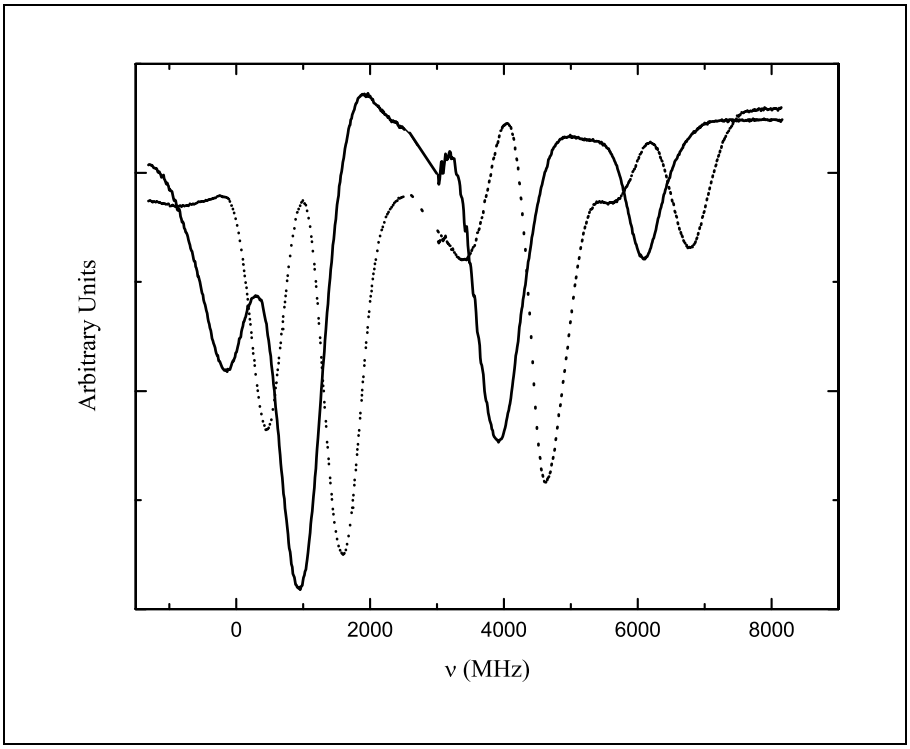

Figure D.8: *Dichroic atomic vapor laser lock signals.*

method, a time of flight technique, uses a pair of counter propagating laser beams which are derived from the trapping laser, and which form a probe region just below the MOT. When trapping lasers are turned off, the time dependence of the probe-induced fluorescence is recorded. The idea is that in the absence of the trapping lasers, the atomic cloud is free to expand at a rate equal to the atoms's v_{rms}. The probe lasers are really measuring the size of the atom cloud, at a known ΔT, and therefore its rate of expansion and hence its temperature. The second method is the so called "fountain" method, in which a probe beam is placed above the MOT. This beam causes fluorescence in atoms having sufficient velocity to rise up its level upon being released from the MOT. Thus, the initial (release) velocity, and hence the temperature is measured. However, the geometry constraints of our apparatus made it inconvenient to bring in probe laser beams above or below the MOT. We therefore

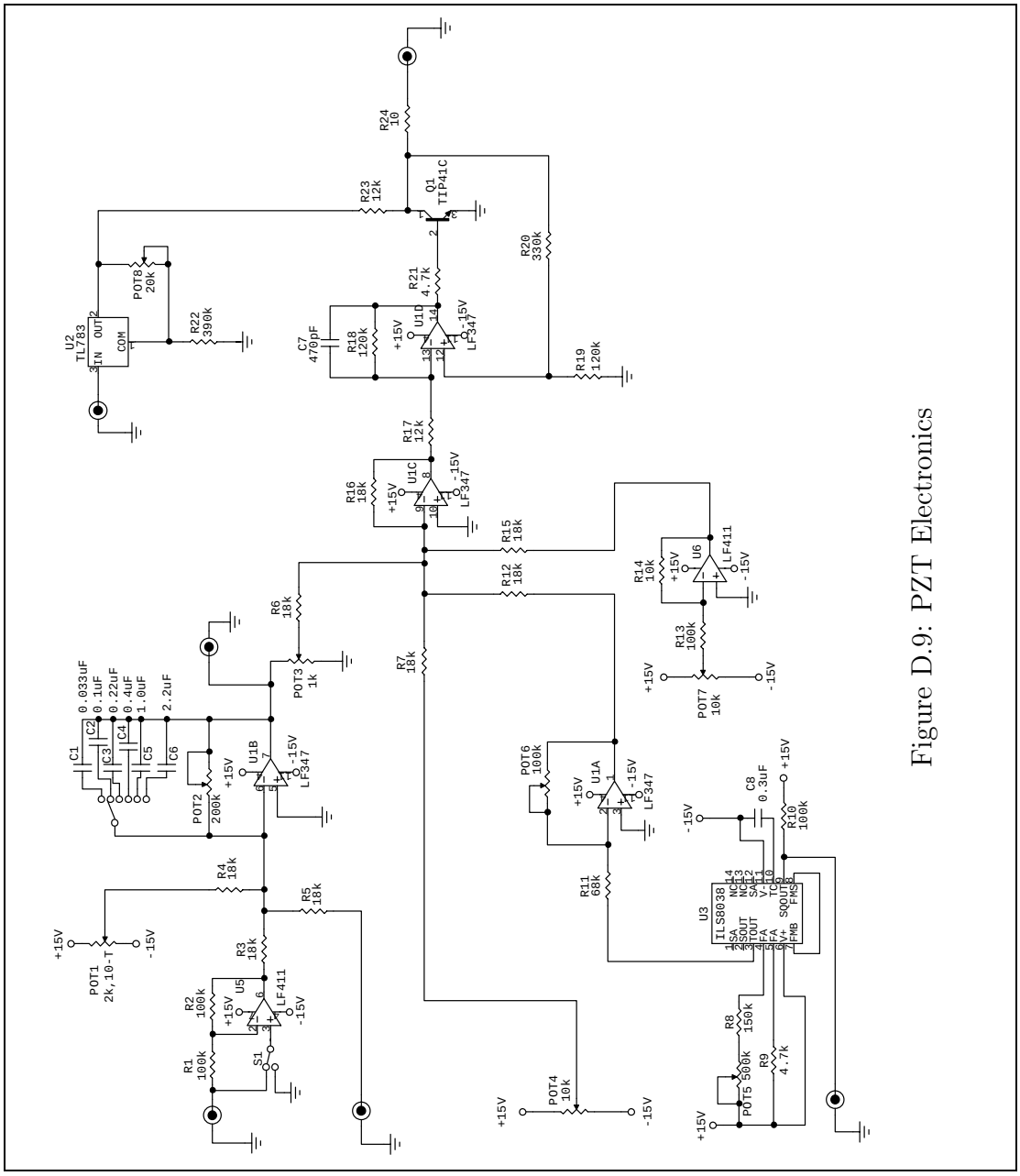

Figure D.9: PZT Electronics

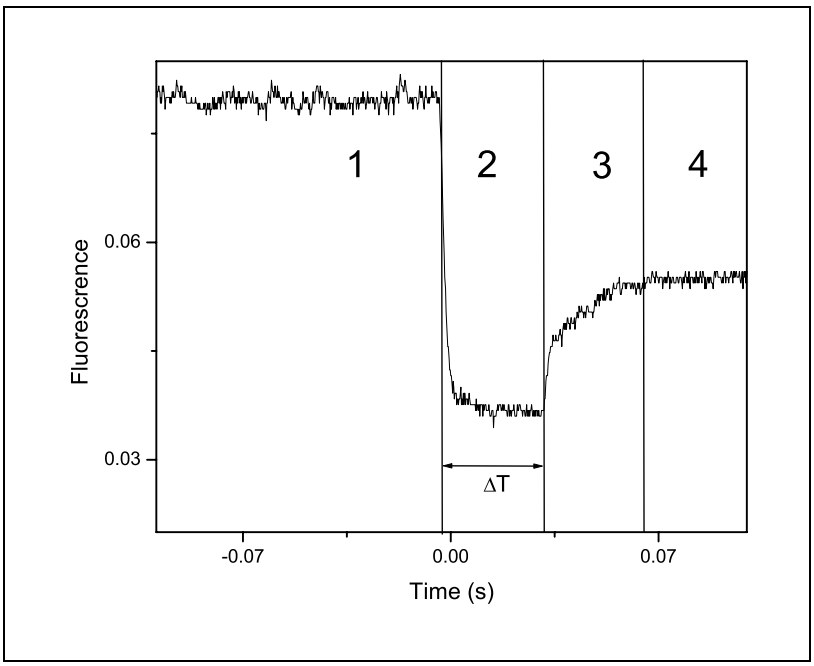

Figure D.10: *Flouresence from TOF measurement.*

chose to use the release and recapture method [98]. In this case, the repump laser is turned off, the MOT is allowed to drop *via* gravitation, while the MOT expands with a Maxwell-Boltzman velocity distribution at temperature T. After some time, the repump laser is turned on and the atoms are recaptured. Figure D.10 shows the measured fluorescence from the target region as (1) the atoms are in the MOT, (2) the repump laser is turned off, (3) the repump laser is turned on. In time interval 4, the MOT population slowly build back. Figure D.11 shows the data and the functional fit:

$$F(t) = \left(\frac{d^2}{< v^2 > t^2 + d^2}\right)^{\frac{3}{2}} Exp\left[\frac{-25000d^2(5t^2 - \tau)^2}{d^2 + < v^2 > t^2}\right] \tag{D.4}$$

where F is the recapture fraction, d = 9 millimeters is the diameter of the laser beam, $< v >$ is the average velocity of the trapped atoms, $\tau = 0.0001$ is an offset constant and t is the time. From the fit using Eq. D.4 and the thermodynamic relation:

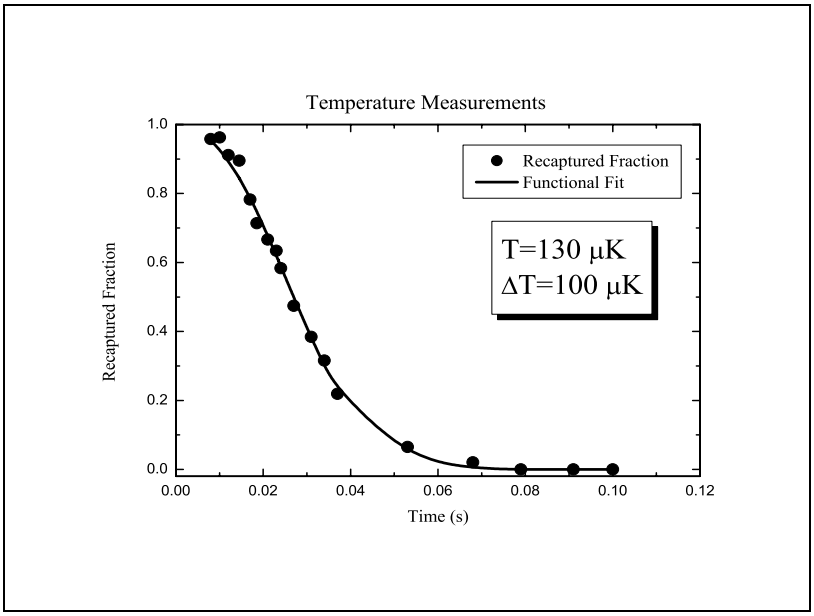

Figure D.11: *MOT temperature measurements.*

$$\frac{1}{2}m < v^2 >= \frac{3}{2}k_B T \tag{D.5}$$

the temperature of the MOT, T, is deduced. The fitted MOT temperature is found to be 130μK $\pm$ 100μK. The large uncertainty comes from the fact that the size of the MOT before and after expansion is not exactly known; nor is the position of the camera. For all intent and purposes of MOTRIMS, temperature is not a limiting factor which one should be concerned about.

D.2.2 Measuring MOT Density

To find the density of the MOT, one can observe the fluorescence of the MOT (hence total number of atoms in the MOT), and obtain the radial MOT dimension (hence the volume of the MOT). Large uncertainly would come from these type of measurements therefore MOT density measurement presented here is only accurate to an order of magnitude. There is an accurate but more involved method of measuring the total

number of atoms in the magneto optical trap [64]. This method makes use of a probe laser and hence add complications to the setup. Moreover, the geometry of our chamber does not allow optical access to do accurate measurement for the MOT number. For the application of the work presented in this dissertation, a thicker target would only mean less time necessary to take data. Therefore, operationally we optimize the MOT to have the highest count rate possible. Thus, accurate measurement of MOT density is not critical. The total number of trapped atoms in the MOT is

$$N = \frac{P_o}{R}\frac{\lambda}{hc} \tag{D.6}$$

where P_o is the optical power emitted by all the cloud into a known solid angle and measured with a photo-diode, and λ is the wavelength of the emitted photon. R is taken as

$$R = \frac{\frac{I}{I_s}\pi\Gamma}{1 + \frac{I}{I_s} + 4\left(\frac{\Delta}{\Gamma}\right)^2} \tag{D.7}$$

and $\frac{\Delta}{\Gamma} = 2.5$, $I_s = 4.1\ mW/cm^2$, and I is the total trapping laser intensity which, in this case, is 12 mW/cm^2. P_o is measured to be 10 μW. This leads to the approximate total number of atoms in the trap of about 4×10^7. Thus, the density is about 4×10^{10} atoms/cm^3. This density depends on the parameters such as rubidium source current and the current in the trapping coils. This parameter space was explored and is documented in the following section.

D.2.3 The MOT in Operation

The magnetic field gradient is proportional to the current in the anti-Helmholtz coils. Shown in Fig. D.12 is the Magneto Optical Trap fluorescence for various values of coil current. We can see that the peak value goes up with current, but the MOT width goes down. For optimum coincidence count rate with respect to the coil current, the current was set to 70 Amps.

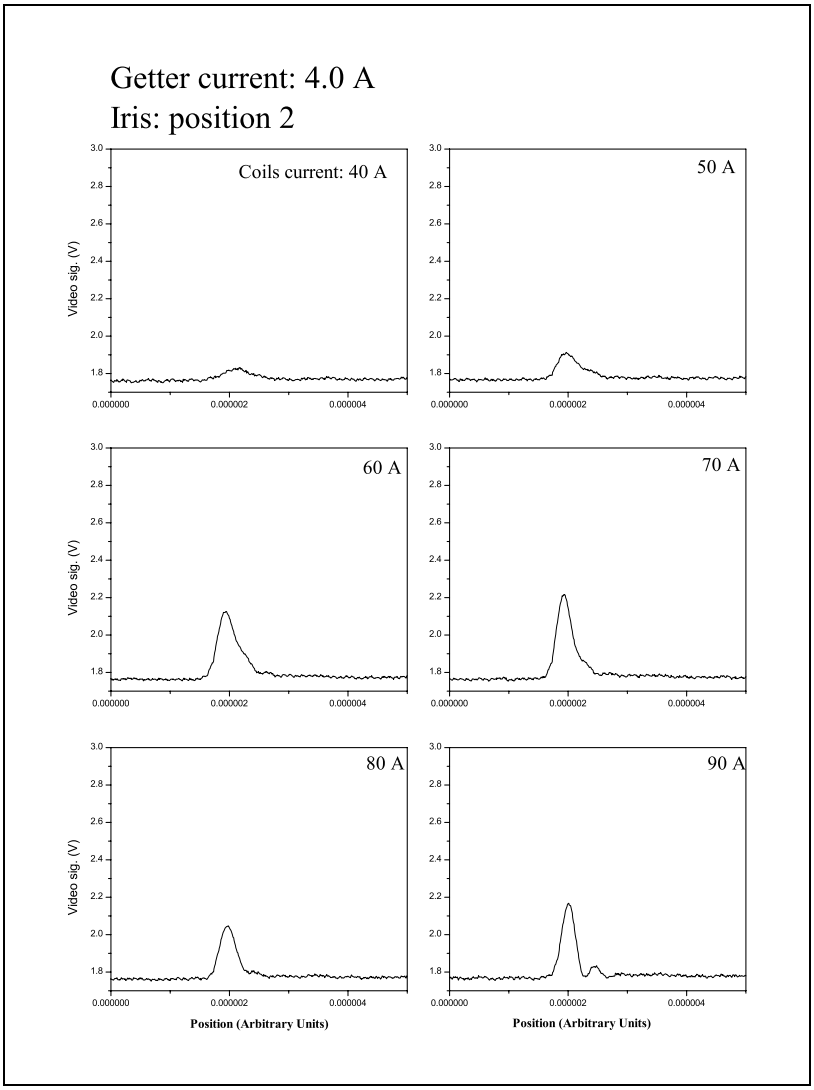

Figure D.12: *Magnetic field dependence of the MOT.*

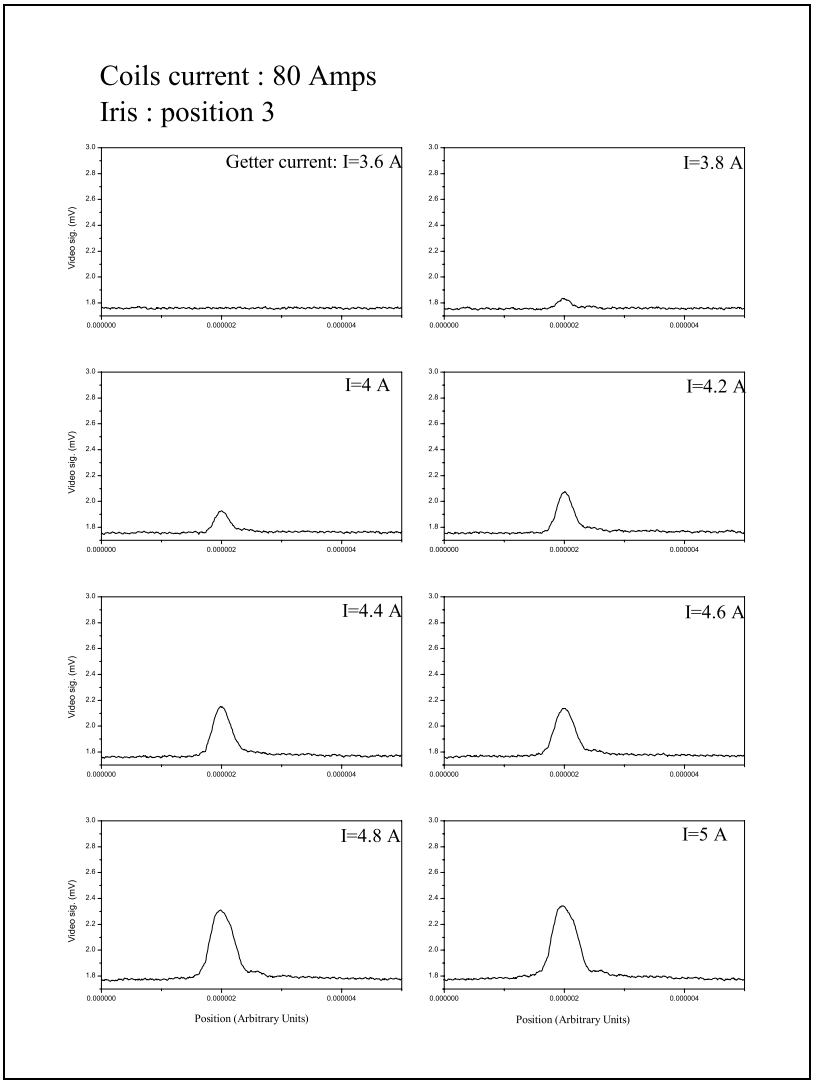

Figure D.13: *Rubidium source current dependence of the MOT.*

The MOT was also studied for different settings of the rubidium source current since it determines background density available for cooling and trapping. The load rate is dependent on the neutral atom collision rate and the background density. Shown in Fig. D.13 is the MOT fluorescence as a function of various values of source current. For optimum coincidence rate, the source current is normally set at or higher than 4.2 Amps.